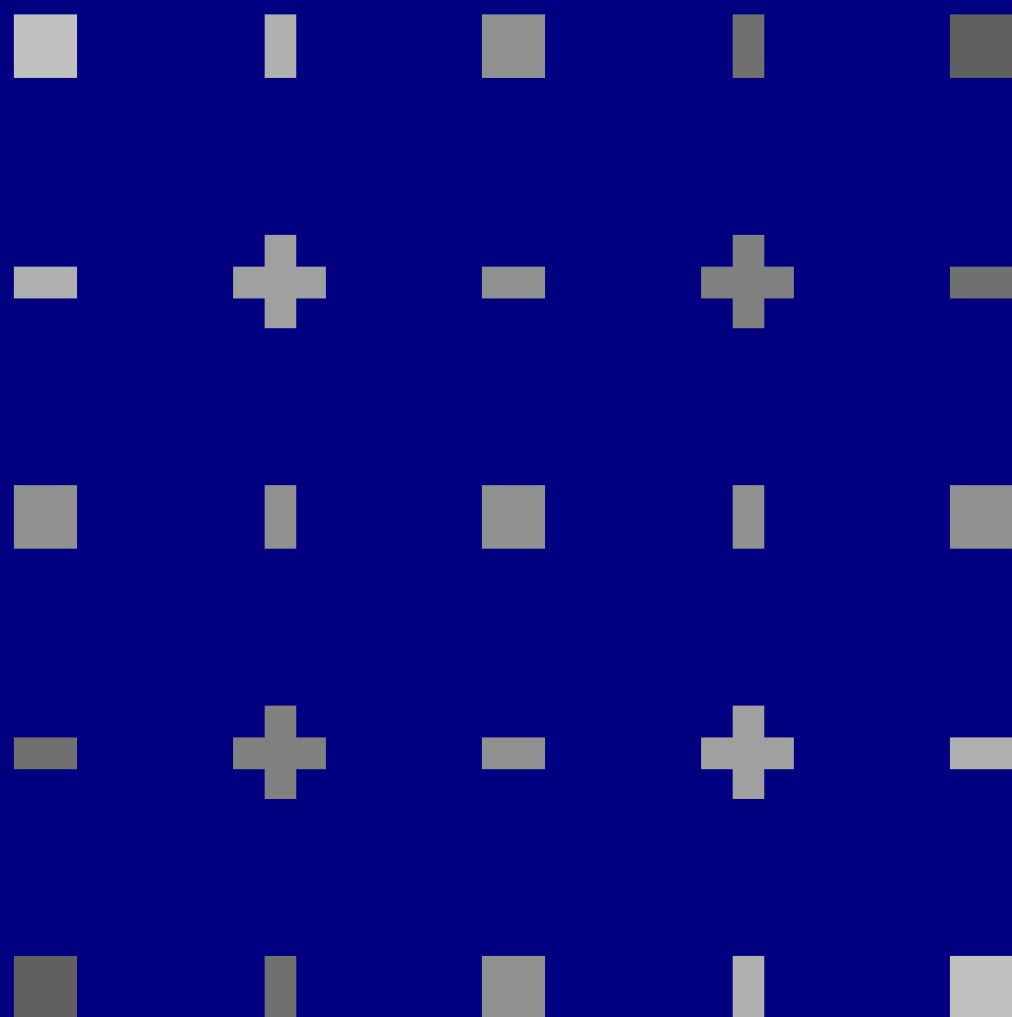# The MECS-IHT system

John van der Koijk

The multi-electrode current-source interstitial hyperthermia system

John van der Koijk

Colofon:
This text was set using the freely available LaTeX2_ε typesetting and text formatting system. The freely available typefaces used for the main text and the maths were 'Concrete Roman and Italic' and 'AMS Euler', respectively. TeX and 'Concrete Roman and Italic' were designed by D.E. Knuth, 'AMS Euler' was designed by H. Zapf for the American Mathematical Society.

The image on the cover illustrates the discretisation problems which can arise when a set of identical parallel cylinders is digitised on a square grid. This phenomenon was encountered when modelling the behaviour of a particular MECS implant geometry and is also present when discrete vessels are discretised.

(Cold-hearted orb that rules the night
Removes the colors from our sight
Red is gray, and yellow white
But we decide which is right
And which is a quantization error.
      ppmtopgm man page–Jef Poskanzer)

The multi-electrode current-source interstitial hyperthermia system

Het multi-electrode current-source interstitiële hyperthermie systeem

(met een samenvatting in het Nederlands)

Proefschrift ter verkrijging van de graad van doctor aan de Universiteit Utrecht
op gezag van de Rector Magnificus, prof. dr. J.A. van Ginkel
ingevolge het besluit van het College van Decanen
in het openbaar te verdedigen op 22 mei 1997 des middags te 12.45 uur

door
Johannes Ferdinand van der Koijk
geboren op 9 juli 1965, te Rotterdam.

promotor: prof.dr. J.J. Battermann, hoogleraar aan de Faculteit Geneeskunde van de Universiteit Utrecht.

co-promotor: dr.ir. J.J.W. Lagendijk, universitair hoofddocent aan de Faculteit Geneeskunde van de Universiteit Utrecht.

Die hohe Kraft
Der Wissenschaft,
Der ganzen Welt verborgen!
Und wer nicht denkt,
Dem wird sie geschenkt:
Er hat sie ohne Sorgen.

J.W. Goethe, *Faust*

aan mijn moeder

Contents

x

Chapter 1

General introduction

In May 1992, a project named 'The further development of the dual-electrode interstitial hyperthermia method' was started at the Radiotherapy department of the University Hospital in Utrecht, The Netherlands. The project was financially supported by the Dutch Cancer Society (grant IKMN 92-14). This thesis contains an account of parts of the work that has been done during the project.

The main parts of this thesis are

▷ a general introduction;
▷ a description of the electronics of the MECS IHT system;
▷ a description of the treatment simulation software that was developed in order to investigate physical properties of the proposed treatment and that is intended for actual patient-related treatment planning;
▷ a detailed investigation of the electrical and thermal properties of the electrodes used in the MECS system;
▷ extensive simulations of the system behaviour in anatomies with and without discrete blood vessels present.

This introduction is intended to place this thesis in the framework of global hyperthermia development.

1.1 Interstitial hyperthermia

Recent clinical phase III trials, using externally applied hyperthermia techniques producing a large heated volume (regional hypoerthermia), have clearly demonstrated the beneficial effect of thermo-radiotherapy (Overgaard, 1994; Overgaard et al., 1995; Van der Zee, 1993, 1995; Vernon et al., 1996). Still, the major problem of local hyperthermia and the main reason for the failure of several clinical studies

is the inability of the present practical heating systems of producing the temperature distributions and dose uniformity clinically desired (Oleson et al., 1993). In regional hyperthermia, relatively small temperature gradients in the target volume can be obtained because of the systemic temperature rise and the large volumes heated (Van Es et al., 1995; Wust et al., 1995). In contrast, on account of the local cooling by blood vessels (Lagendijk, 1990a; Roemer, 1990b), current interstitial hyperthermia practice shows temperature/thermal dose uniformities so bad that it is surprising to see that fair results have been obtained in some clinical studies (amongst others Cosset (1990); Salcman and Samaras (1983); Roberts et al. (1986); Silberman et al. (1985)). Sneed et al. (1992) showed, in the treatment of gliomas, that a more uniform dose (higher T_{90})[1] positively correlated with local response, emphasizing the great clinical importance of better temperature uniformity/distributions.

Recent treatment simulations and experimental research indicate that the temperature control problems can be solved: spatial control of the absorbed power (SAR) distribution at a centimetre scale can make up for local blood flow cooling and prevent hot spots related to tissue heterogeneity; thus, much improved temperature uniformity can be obtained (this thesis, Crezee and Lagendijk (1992); Lagendijk et al. (1993, 1994b)). The essential spatial SAR control can be obtained with new 3D-controlled interstitial hyperthermia (IHT) systems and scanned focused ultrasound (SFUS) systems.

The SFUS systems, which are basically non-invasive, are handicapped by the absence of massive invasive thermometry (Lagendijk et al., 1994b). Interstitial hyperthermia systems can benefit from extensive thermometry in the catheters/needles or can rely on intrinsic temperature control (hot source/thermal conduction techniques). Another attraction of interstitial hyperthermia is the possibility of combining it with brachytherapy, using the catheters/needles already present; the benefits of local hyperthermia can then be added to the treatment with minimal additional trauma to the patient. Interstitial hyperthermia can also be combined with simultaneous external-beam radiotherapy.

In this thesis it is illustrated that interstitial techniques which provide just two-dimensional control, (that is, no SAR control along the implanted track) are not capable of producing satisfactory temperature distributions in a heterogeneous anatomy containing discrete vessel structures. Interstitial hyperthermia systems

---

1.   As they are used here, T_{10} and T_{90} are characteristics of the temperature distribution in a volume. They are estimates of the time-averaged intra-tumoural temperatures which 10 respectively. 90 % of all measured temperatures were at or above.

with insufficient three-dimensional SAR-control are characterized by uncontrolled inhomogeneities in the temperature distributions obtained (Goffinet et al., 1990).

Several refinements have been proposed to improve the spatial control of the present-day IHT systems:

▷   Hot source conductive techniques:
  –   Techniques using hot water circulation through implanted tubes provide intrinsic longitudinal control if the thermal resistance of the needle wall is low as compared to the thermal resistance of the surrounding tissue (Hand et al., 1991). Unfortunately, this condition is not always met by present-day systems (Handl-Zeller, 1993).
  –   Thermal seeds: metallic seeds/needles heated by magnetisation losses in a varying magnetic field. The losses depend on the Curie-temperature of the metallic seed. The generated heat is transferred to the tissue by heat conduction. The use of thermal seeds with Curie-point power control may be a viable technique if the bare seeds are inserted in tissue. The influence of the thermal resistance of a plastic catheter destroys the intrinsic control capacities (Van Wieringen et al., 1996a). The use of brachytherapy needles containing low Curie-point metals looks promising, amongst other reasons because of the possibility of simultaneous interstitial irradiation (Van Wieringen et al., 1996b). Metal needles loaded with ferrite may also be useful.
  –   A conductive technique using small electrically heated elements is commercially available[2]. No longitudinal control of the heat source is available in this system. A similar technique is the scanning of small antennas or infrared sources through synthetic catheters (Steger, 1993).
  With regard to the conductive techniques mentioned above, the conclusion should be that sufficient spatial control may be obtained if the technological problems can be solved. However, since no heat is produced outside the applicators, the lateral spacing between catheters/needles is subject to an upper limit of about 10 mm (Schreier et al., 1990; Hand, 1993; Stea et al., 1994). This requirement results in prohibitively large(-r) numbers of catheters/needles to be implanted in the patient.
▷   Two of the advantages of interstitial microwave techniques (which exploit thin antennas which emit radiation in the microwave range, inserted into the patient) are their compatibility with plastic catheters and the good

─────────

2. The VH8500 Hyperthermia system from [William] Cook Inc, Bloomington IN, USA.

SAR penetration depth. The SAR patterns permit a lateral spacing between catheters of 15–20 mm (20 mm when using dipole antennas and constructive interference (Coughlin et al., 1992), 15 mm when using helical coils (Ryan et al., 1994)), compared to 10–15 mm with other (non microwave) techniques (Stauffer, 1990; Seegenschmiedt, 1993). For this reason, microwave antennas have been used for the heating of brain tumours (Sneed et al., 1992; Ryan et al., 1994). Unfortunately, technical problems arise when attempts are made to upgrade the present 2D (laterally) to 3D (longitudinally and laterally) controlled systems. A technique using multiple node, microwave antennas to improve longitudinal SAR uniformity has been described (Lee et al., 1986). Independent control of multiple segments seems possible; however, problems like cold antenna tips (Leybovich and Kurup, 1992) and heterogeneous absorption along the antenna will probably remain unsolved. Integration of extensive 3D thermometry with these techniques is also a hard problem, because the power transmission lines take up so much space that little room is left for thermal sensors other than thermocouples. However, thermocouples are are not easily usable because of interference with the technique.

▷   A technique employing small cylindrical segmented ultrasound transducers is being developed (Hynynen, 1992; Diederich and Hynynen, 1993). This system may provide excellent spatial steering if the problems with transducer efficiency can be solved. Self heating of the ultrasound electrodes produces a conductive thermal component which reduces the benefits of the ultrasound technology because it limits the allowed lateral spacing between electrodes and complicates thermometry. Diederich et al. (1996) states that he can produce applicators with an efficiency of about 70% which would make it possible to build a system that is roughly equivalent to an RF-LCF system with integrated thermometry. Using an integrated catheter cooling system this method would in theory be capable of producing very homogeneous temperature distributions in the target volume. A major problem in such a setup may be the absence of reliable and extensive thermometry.

▷   A segmented electrode, local current field (RF-LCF) technique has been developed at Stanford University (Prionas et al., 1992). This voltage source technique (galvanic contact between tissue and fixed-potential electrode) uses small metallic segments deposited on an electrically insulating carrier. Simultaneous operation of segments of differing potential at the same carrier causes hot spots between the segments; alternative switching techniques in which only electrodes at different carriers are energised simultaneously have

yet to be tested in the clinic. Engineering problems arise with the large number of RF-connections but these appear to be manageable.

▷   Visser et al. (1989) developed a 27 MHz current source (capacitively coupled) technique using single metal electrodes inserted in standard plastic brachytherapy catheters in the Dr. Daniel den Hoed Cancer Center. Current source techniques allow flexibility in RF-current control because of the uniform current injection along the electrode and the loose electrical coupling between the electrodes (Deurloo et al. (1991), this thesis) . Spatial SAR control can be achieved by operating several independent electrodes in a single catheter. The 64 channel MECS interstitial hyperthermia system, based on the design by Visser et al., was developed in close collaboration with the people at the Dr. Daniel den Hoed Cancer Center. The MECS IHT system includes an integrated 196 channel thermometry system and should be able to provide the 3D-SAR control needed (Lagendijk et al. (1995); Kaatee et al. (1992), this thesis).

The availability of adequate spatial control of the SAR is a *necessary* but not a *sufficient* condition for an actively controlled, good working interstitial hyperthermia system. The SAR must be adjusted to reach the desired temperature distribution in the implant; this depends on unevenly distributed and dynamically changing thermal drains in the target volume. Therefore, the availability of treatment planning and sufficient information on the actual temperature distribution in the target volume during treatment is crucial for these systems.

1.2   Planning and simulation

There are two fundamentally different ways of investigating the physical behaviour of a proposed hyperthermia treatment method.

The first is direct experimentation with the system under consideration, using it to heat up a certain volume and assessing the quality of the system by investigating the results of physical measurements conducted in the tissue.

The other approach is to build a computational model of the system and to use this model to simulate treatments. Then, the results of the computer simulations are investigated.

The strengths and weaknesses of the two alternatives are largely complementary. Using computer models one can quickly gain an understanding of the important parameters of the treatment problem, without being bothered by practical details

like thermometry. The drawback of this approach is that it is not clear *a priori* that the models offer a sound and complete representation of reality. The physical experimentation approach does not suffer much from this defect but it is practically hard to vary the parameters of the treatment (see also Roemer (1990b)).

So far, most of the literature on hyperthermia related computer simulations concentrated on homogeneous phantom situations, 2D-SAR control and thermal continuum models without discrete vessels (DeFord et al., 1991; Paulsen, 1990b,a; Gentili et al., 1995). This approach sufficed for comparing the properties of the different 2D controlled IHT techniques (Strohbehn, 1983; Strohbehn et al., 1982; Stauffer et al., 1989). Now that reliable 3D-SAR and thermal models are available, simulation of complex 3D heterogeneities becomes feasible. In the project period, we have developed a treatment planning system capable of simulating MECS implants in tissues with quite arbitrary vessel networks (De Bree et al., 1996b; Kotte et al., 1996d,b). The effectiveness of 3D-SAR steering with the MECS system was demonstrated in a case study of a brain implant containing a very heterogeneous large vessel density (Lagendijk et al., 1995). Spatial control in a heterogeneous dielectric anatomy for the MECS system, notably at fat-muscle interfaces has been investigated by Van der Koijk et al. (1995) (this thesis). A similar investigation, focusing on the effects of discrete vessels in the treatment volume, is reported on in chapter 7.

The approach chosen in this thesis is mainly the computational one. At this moment, a new project is running which encompasses clinical tests of the results presented here.

In the current context of system evaluation, the collection of hyperthermia simulation tools built in Utrecht during the last years contains four components of major importance:

▷   a power deposition model, used to calculate the heat deposited in the tissue by the MECS-IHT treatment system;

▷   a heat transport model, which is used to model heat transport in the tissue, including the heat transport by discrete blood vessels;

▷   a control algorithm capable of mimicking the behaviour of the control system in the real IHT-machine;

▷   a suite of visualisation and evaluation tools.

It is of great importance for the validity of the conclusions drawn from the simulations that the computer models and the data they operate upon are qualitatively correct. For actual treatment planning purposes an even higher standard, that of quantitative accuracy, is desirable.

1.2.1 Power calculation

SAR calculation models for use in EM-hyperthermia in the 70 to 900 MHz range have been around for a while. 3D models for regional hyperthermia have been presented by amongst others James and Sullivan (1992); Paulsen et al. (1992); Hornsleth (1996); Zwamborn et al. (1992); Jia et al. (1994). Sowinski (1992) and Chen and Gandhi (1989) have published on electrical models for low frequency RF techniques. For the MECS interstitial hyperthermia system ($f = 27$ MHz) we have developed a specialised finite difference SAR model capable of handling heterogeneous tissue properties and the steep gradients around electrodes (De Bree et al., 1996b). The SAR model is described in chapter 3. In the model, the electrodes are represented by a current source term. The calculated electrical potential is corrected using an analytical approximation of the near field of the electrode. In this way, the SAR distribution in the implant may be calculated at a resolution comparable to the diameter of the electrode cross-section and rather high compared to the size of the implant volume. This grid resolution is too coarse to be used for modelling the fine-structure of the applicator; a separate study has been undertaken to understand the thermal and electrical behaviour of the MECS-applicator (Van der Koijk et al., 1997b,a). That work is presented in chapters 4 and 5.

1.2.2 Heat transport calculation

The tissue temperature distributions existing during (interstitial) hyperthermia treatments are strongly influenced by blood flow. Both a heat sink term proportional to the blood flow rate and an enhanced thermal conductivity of the tissue have been proposed to model the collective behaviour of the blood vessels (Pennes, 1948; Chen and Holmes, 1980; Weinbaum and Jiji, 1985; Lagendijk and Mooibroek, 1986). However, for the prediction of the local thermal effects of large vessels and of possibly serious temperature inhomogeneities, discrete modelling of the vessels with diameters $\gtrsim 0.5$ mm is very important (Lagendijk, 1990a; Roemer, 1990b; Van Leeuwen et al., 1996). A numerical model which can handle discrete blood vessels is required for the calculation of temperature fields in the presence of arbitrary vessel structures. The vascular structures may be obtained for individual patients using 3D-angiographic techniques.

Lagendijk et al. (1984) developed a thermal model in which a cubic finite difference grid is locally modified to accommodate a straight vessel. Simulations involving straight vessels were also performed by, amongst others, Chen and Roemer (1992) and Rawnsley et al. (1994). A more versatile discrete vessel model which allowed

vessels to curve and to branch was designed by Mooibroek and Lagendijk (1991). In an attempt to create a less complicated, more elegant and more practical thermal model, an alternative model was devised (Kotte et al., 1996d). This new approach resulted in a model in which the vascular structures are represented as trees of parametric tracks through space, independent of the finite difference grid of the tissue. For the calculation of the interaction between tissue and vessels an analytic approach is used.

The new model has been used for all thermal simulations of the MECS system described in this thesis.

1.2.3 Thermometry and control

During interstitial hyperthermia treatment the tumour tissue temperature is increased in a controlled fashion. In systems without intrinsic control (unlike hot water tubes and thermal seeds), this requires monitoring of the three-dimensional temperature distribution to determine the optimal power setting of the individual heat sources. The spatial distribution and density of the thermometry should match the degrees of freedom available to the control of the power deposition (Hand, 1993). Normally, invasive thermometry probes are used, either integrated into the heating probes or in separate, non-heated catheters (Hand, 1993).

Temperature measurement in the electrode catheters gives a good impression of the maximum temperatures in the implant and is very suitable for power control of individual electrodes. In the MECS system the combined data from a seven- or fourteen-point thermocouple strings in each catheter yields detailed three-dimensional information on the temperature distribution without additional trauma to the patient (Lagendijk et al., 1995; Crezee et al., 1997). Disadvantages of this approach are that minimum tissue temperatures cannot be evaluated straightforwardly, and that the proximity of the heating system can affect the reliability of the thermometry readings. For these reasons, thermometry in separate non-heated catheters is often used, especially for microwave heating (Emami et al., 1990). This also has the advantage of giving a better impression of the minimum tumour temperature. A disadvantage is the extra trauma inflicted to the patient: the minimum numbers of extra catheters recommended by Emami et al. (1990) ranges between two (for 3–8 heat sources) and six (for 33 or more heat sources).

The MECS system, with its segmented electrodes, would thus need an unacceptable number of extra thermometry catheters; it would be more sensible to use

these extra catheters for heating too, further improving the spatial temperature control. In the absence of dedicated thermometry catheters the minimum temperature can be estimated using the thermometry integrated in the heating catheters by sequentially interrupting the power of each electrode for a some time, to measure the local minimum tissue temperature, while maintaining stationary heating at the other electrodes.

1.3   Tissue properties and vascular structure

Treatment planning systems exist by the grace of qualitatively good input data.

The electrical and thermal models available at this moment are verified and can solve practical problems (Kotte et al., 1996c; Van Leeuwen et al., 1996; De Bree et al., 1996a). The weak link in the whole planning process is the acquisition of patient specific information—the tissue properties and the vascular structure. A project called 'Improved hyperthermia treatment planning by using realistic patient data' (NKB-UU-96-1192) was started to address these problems.

This section describes methods that may be used for obtaining information about the distribution of the electrical, thermal and vascular properties of the target volume.

Electrical properties

The electrical contrast between low water content tissues (like fat and bone (Smith and Foster, 1985)) and high water content tissues is high (Johnson and Guy, 1972). Even relatively thin layers of low conductivity/high resistance fatty tissues can influence the RF-field distribution significantly (James and Sullivan, 1992; Turner, 1983; Wust et al., 1995). Thus, the dielectric anatomy has to be imaged with considerable detail, in three dimensions. For the volumes involved in interstitial hyperthermia (in the order of $100\,cc$) a model resolution of $1\,mm$ in all directions is practical with the computational means available at this time (De Bree et al., 1996b). The dielectric contrast between high water content tissues (for example: white versus gray brain tissue) is less pronounced but still important for treatment planning. Accurate estimation of the dielectric property distributions within these tissues is hard. Under physiological conditions a traceable relation exists between water content and the dielectric constants (Schepps and Foster, 1980). Currently utilised MR imaging techniques (SE, IR, SPIR, MTC) can be used to obtain so-called 'multiple parameter images' (ρ, T_1, T_2) which contain information on the

tissue (bound/free) water- and fat content. Thus, MRI techniques for proton density measurement can be used to estimate the tissue water content and provide a basis for estimation of the dielectric properties of a tissue volume. A moderately successful attempt at estimating the electrical anatomy pixel-by-pixel has been made this way (Van der Koijk et al., 1993).

Another approach to this problem is segmentation of the anatomy (from CT or MR imagery) into a relatively small set of tissue types and then assigning dielectric properties (from literature and/or invasively measured) to the various tissues (Jia et al., 1994; James and Sullivan, 1992).

At the RF frequency used by the MECS IHT system (27 MHz) the electrical conductivity and, less accurately, the permittivity, may be measured at treatment time using impedance probes placed inside the catheters. This involves solving a badly posed inverse problem, which is mathematically very hard to do. The sensitivity and stability of this method is questionable.

Thermal properties: lumped effects

In living tissue, heat transfer due to blood flow (convection, mass transport) dominates over heat transfer due to the intrinsic thermal conductivity of the tissue. Depending on the tissue involved, heat transfer by convection may be ten times the heat transfer by conduction (Lagendijk et al., 1988). For the soft (high water content) tissues, the variation of physical properties like thermal conductivity, specific heat and specific weight is low (ESHO/COMAC Task Group report 4 (Lagendijk et al., 1992)). The contrast between high water content tissues and low water content tissues like fat and bone is high; however, these low water content tissues can easily be found/segmented using MRI and/or CT. A similar segmentation is performed to obtain a dielectric anatomy.

The blood flow depends on physiology and temperature; tissue blood flow may increase significantly at hyperthermic temperatures, making more or less extensive *in vivo* data acquisition and feedback control during actual treatment unavoidable (Nah et al., 1996; Sekins et al., 1982, 1984; Milligan, 1987; Roemer and Cetas, 1984). Extensive *in vivo* temperature measurement techniques are being developed to determine the resulting temperature distributions, the tissue cooling coefficients and the effective thermal conductivity (Lagendijk et al., 1988; Roemer, 1990b; Crezee and Lagendijk, 1990). Ultimately, the temperature data should be correlated with the outcome of the treatment planning procedure and the 3D imaging results (Roemer, 1990b). This could supply useful data concerning the transient behaviour of blood flow.

Measurement of the 3D (small vessel) perfusion distribution in patients is currently mostly done by fast MRI techniques, although dynamic computed tomography also seems to offer potential in this area (Feldmann et al., 1992; Lyng et al., 1993). Initial clinical results with MR perfusion imaging were reported recently (Aronen et al., 1994). Interpretation of MR perfusion images relies on application of the so-called indicator dilution theory. Direct verification by phantom studies has been occasionally attempted (Duewell et al., 1990).

Thermal properties: discrete vessels

Discrete vasculature (vessel diameter $> 0.5 \, \text{mm}$) causes large inhomogeneities in the 3D cooling field, making angiographic imaging of both the arterial and venous vessels inescapable (Crezee and Lagendijk, 1992; Roemer, 1988; Chato, 1990; Lagendijk, 1990a; Rawnsley et al., 1994). Lagendijk et al. (1993, 1994a, 1995) highlighted the importance of the density of large vessels for the major temperature inhomogeneities observed during treatments. In theory, a combination of angiographic techniques and thermal modelling may supply the information required for spatial control of the SAR, provided that sufficient thermometry is available for verification and feedback (Lagendijk et al., 1995; Roemer, 1990b). Despite the rapid progress in 3D MR angiography (Potchen et al., 1993) and in discrete-vessel thermal modelling (Mooibroek and Lagendijk, 1991; Lagendijk et al., 1995; Kotte et al., 1996a), the application of thermal modelling to clinical studies is still in its infancy, which implies that the heterogeneity in local tissue cooling can only be measured directly by invasive thermometry. The spatial resolution needed for thermometry is about 1.0–$1.5 \, \text{cm}$ (Lagendijk et al. (1994b), this thesis) which implies that, for inherently *non-invasive* heating techniques, an impractically large number of probes/sensors must be implanted to make this information available. The use of extensive invasive thermometry is less impractical when interstitial heating techniques are used because of the inherently *invasive* nature of these techniques. This side effect makes IHT treatments an especially suitable test area for hyperthermia treatment planning.

In most studies the vascular cooling field is interpreted with models containing the Pennes heatsink term in the bioheat transfer equation (Pennes, 1948). The volumetric perfusion rate in this equation can be determined in several ways (Lagendijk et al., 1995; Roemer, 1990a). One of the most popular methods uses the temperature transient after a step-wise increase or decrease of the applied power. If the conduction term is assumed to be negligible with respect to the convection term, the temperature will adapt exponentially with a time constant τ yielding the perfusion rate $W_b = \rho_{\text{tis}} c_{\text{tis}} c_b \tau$ (Milligan et al., 1983; Waterman et al.,

1987). A second method to determine W_b is based on the measurement of the power density P required to maintain a stationary temperature rise ΔT, assuming $W_b = P/(c_b\,\Delta T)$. The thermal diffusion probe is a specific technique for this measurement. The probe is heated to some fixed temperature level above that of the surrounding tissue (Bowman et al., 1992) after which the amount of power required to maintain the probe at that temperature is measured.

The validity of these methods rests on the assumption that the heatsink model is a relevant model for bio heat transfer in the given situation. Many researchers prefer to use a thermal clearance coefficient, e.g *PERF* (Lagendijk et al., 1988; Lyng et al., 1991) or U_{tc} (Roemer, 1990b). To determine *PERF* or U_{tc}, the same techniques are used as for W_b, only the interpretation of the result differs.

The quantification of blood flow via measurement of the cooling coefficients may only be obtained through a discrete vessel thermal model, because of the relations between the cooling coefficients and the discrete vasculature (Crezee et al., 1994).

1.4   Evaluation of temperature distributions

From a physical point of view, the goal of a hyperthermia treatment is adequate heating of a given target volume during a prescribed time. Although this may seem to be a clear objective, there is trouble defining what exactly we mean by 'adequate heating'.

It turns out to be practical to characterise the temperature distribution in the target volume statistically, using temperature measurements at discrete points in the volume. Various criteria have been proposed to assess the quality of a given temperature/thermal dose distribution. The temperature volume histogram and its derived parameters T_{10}, T_{50} and T_{90} are popular as they suit the statistical nature of clinical temperature data (Ryan et al., 1994; Stea et al., 1994). They describe the time-averaged number of intra-tumoural temperature measurements which 10, 50 respectively 90% of all measured temperatures were at or above.

Other criteria include the minimum tumour temperature (Shimm et al., 1990) and the percentage of tumour volume above the target temperature, e.g. the HEP rating (Paulsen et al., 1984; Strohbehn, 1994).

The cumulative temperature/volume histograms used as a primary means of evaluating temperature distributions in a target volume in this thesis are constructed from the calculated temperatures of all voxels in the simulation target volume at

a single point in time. This parameter is not directly comparable to CTVH's obtained in clinical measurement; in general, the latter are constructed from thermal sensor readings at a limited number of fixed locations in the target volume during an extended treatment period (Van der Koijk et al., 1996).

Chapter 2

The multi-electrode current-source interstitial hyperthermia system

2.1   Development of the MECS IHT system

In the middle of the eighties, Marchal and Visser experimented with capacitively coupled RF-electrodes in tissue operating at a frequency of 27.12 MHz (Marchal et al., 1989; Visser et al., 1989). The power was transfered from the amplifiers to the patient using coaxial transmission lines with special impedance transformers which adapted the transmission line system to the electrode impedance[1].

One reason for trying capacitively coupled RF-electrodes was that the galvanically coupled interstitial RF-systems used earlier suffered from uncontrollable hot spots in the volume if the electrodes were implanted non-parallel or along curved paths (Deurloo et al., 1991). The capacitive coupling employed in the MECS system introduces a large impedance in the source characteristic as seen from within the tissue, so that the current density along the electrode in the catheter is relatively independent of the location of other electrodes or peculiarities of the surrounding tissue. This statement will be substantiated in chapter 4.

The first systems designed around the concept of capacitive coupling used a single large electrode per catheter. These systems were handicapped by the complicated impedance transformation techniques used at the end of the transmission line systems near the patient, by cross-coupling between electrodes and by the self-heating of the catheter wall. Due to these problems, the clinical acceptance of these systems was small (Levendag et al., 1993).

Building on the experience of it's inventors, the method was re-designed (Lagendijk, 1990b). Transmission line impedance transformation techniques were used

---

1.   The electrode impedance is the impedance which is measured between the terminal connected to the electrode just outside the patient and 'earth potential' (at 27 MHz).
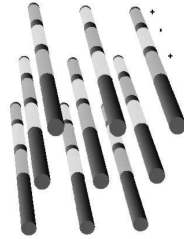
Figure 2.1: Illustration of a multi-pole implant.

and a special electronic design eliminated the cross-coupling between electrodes. The dual electrode concept was introduced: by using two somewhat shorter electrodes of opposite phase in one catheter, a dipole-like RF-field was generated with a single catheter. By connecting the two electrodes to individual power sources, unlike what is common in microwave dipole arrays, such dual electrode arrays allow SAR control along the catheter, while, because of the current source behaviour, the electrodes do not have a cold tip, allowing minimization of the insertion depth in e.g. brain implants.

Later on, our thermal modeling indicated that, in order to be able to achieve satisfactory clinical temperature distributions, it would be necessary to have real three-dimensional control over the power deposition at a scale of about one centimetre. So, to improve spatial control of the SAR, shorter electrodes were used, allowing more electrodes per catheter. Applying the principle of alternating the phase of adjacent electrodes, while using more than two electrodes per catheter, multi-pole fields can be generated allowing 3D control of the displacement current distribution in tissue (see figure 2.1).

The partitioning of the electrodes in two groups at opposite phase, makes that the main current flowing through the patient will be kept local to the implant. This limits the current flowing to a ground plane at relatively large distance from the implant; in this way the production of RF-interference is also minimized. To operate such a multi-electrode implant a completely new heating system was designed; the multi-electrode current source interstitial hyperthermia system (MECS-IHT system) (Lagendijk et al. (1995); Kaatee et al. (1992), this thesis). This system can support 64 electrodes, 32 of each phase, and thus implants of 20–30 catheters.

Figure 2.2: Photograph of the assembled IHT machine. The following subsystems are shown: to the left, the system console. In the cabinet next to the console, the power generator, switchboards and dedicated controller. During treatment, the detached connection box is located near the patient.

2.2 Overview of the treatment system

The MECS–IHT treatment system (see figure 2.2 for an impression of the assembly) is a complex machine which consists of four main components:

▷ the RF subsystem which generates the power needed to heat the patient;
▷ a thermometry system featuring 196 independent channels, used to obtain information on the temperatures in the treatment volume;
▷ a connector-system which provides a flexible connection between the RF subsystem and thermometry system and the patient;
▷ a workstation which is used to coordinate the actions of the other subsystems and to provide a comfortable interface to the human operator.

The thermometry system is the same as the one described by De Leeuw et al. (1993). Its main features are:

▷ 196 thermocouple sensors can be simultaneously connected to the system;
▷ 0.005°C resolution;
▷ long term stability better than 0.1°C;
▷ data acquisition time for all channels is 320 ms;
▷ recovery after RF-disturbance within 1 s;
▷ an optical serial data link.

The thermometry system is used to acquire temperature information from within the implant during treatment. The design allows the use of 7–14 constantan-manganin thermocouple sensors per catheter. Sensor information is used for feedback control of the electrode duty-cycles and for analysis of the treatment. The connector system provides a safe and flexible connection between the RF subsystem, the thermometry system and the implant at the patient side. The connector unit itself can be rigidly attached to the treatment bed (safety) and provides a front panel with all the connections for thermometry and RF-channels.

The controlling workstation is a Silicon Graphics Iris-Indigo with an R3000 CPU and 32 MB of core memory. The system runs under Irix-5.3, a multi-tasking Unix-like operating system. The multi-tasking ability of the workstation allows a flexible design of the control software and the real-time evaluation and visualisation of results during system operation (Kanis et al., 1994). During treatment, for safety reasons, the whole system is disconnected from the local area network of the department.

The workstation controls the power generating sub-system and gathers thermometry data. The electrode duty cycles are controlled by a process using the thermometry data from the patient, effectively implementing a feedback loop. Thermometric

and system status information is presented to the operator in a graphical way. If necessary, the operator can manually control the settings of the system, overriding the feedback control algorithms. The user interface and control programs have been developed by the collaborating group at the Daniel den Hoed Cancer Clinic in Rotterdam, headed by dr. A.G. Visser.

Both the structure of the RF-system and the matching of the electrode impedance to the MECS-system are the subject matter of the remainder of this chapter.

2.3   Structure of the RF power generation system

The RF power generating system, which, for brevity, will be called the TOP (Tower Of Power) in this chapter, has three main sub-systems:

▷   a dedicated micro-computer system, the embedded controller, which maintains communication with the workstation and is responsible for the operation of the power amplifiers and switch-boards in the TOP and for system security;

▷   a power supply containing a state machine which guarantees the correct startup-sequence for all the supply voltages originating from the power supply;

▷   a complex RF subsystem which itself contains a number of sub-systems.

The security of the system (safety of the patient and integrity of the hardware and software) is maintained at several levels:

▷   physical layer: the system is decoupled from the AC-net using decoupling transformers;

▷   manual override: the system can be shut down in a controlled fashion using an emergency/panic button;

▷   pre-set limitations on supply currents and reflected power;

▷   integrity of communications: the dialog between the embedded controller and the workstation is monitored by an error counter and a watchdog timer in the embedded controller.

In general terms, the RF subsystem, which produces and controls the power sent to the patient, works as follows: two RF pilot signals (at 27.12 MHz) with a phase difference of 180° are amplified by a number of RF-power amplifiers. The output of each amplifier is led to a switching network which produces an amplitude (on/off) modulated RF power signal with a duty cycle directly controlled by the embedded controller of the TOP. Each individual duty cycle modulated signal is then coupled
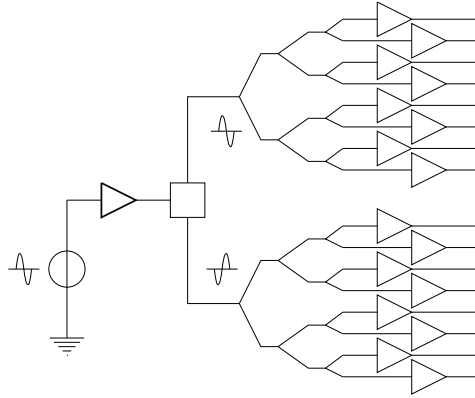
Figure 2.3: Cascade of amplifiers from pilot generator to signals offered to the switchboards.

to the electrode in the catheter, using a coaxial transmission line impedance transformation technique. The transmission line system allows the pooling of several channels, in order to increase the power available at single electrodes, if necessary.

In the following subsections, this overview will be worked out in more detail.

2.4 RF pilot generation and power amplifiers

The RF power signals are generated in the following cascade (see figure 2.3):

▷   a crystal oscillator followed by a power amplifier, which produces pilot signal at a frequency of 27.12 MHz from which the RF power signals are derived;

▷   a splitter and a phase shifting network producing two pilot signals with a phase difference of 180°;

▷   for both phases, a splitting network which produces the input signals for each of the last-stage power amplifiers;

▷   a battery of 2×8 power amplifiers, 8 for each phase.

2.5 The switchboard

The power signals from the last-stage amplifiers are fed to a battery of 16 so-called switchboards. The switchboard has two main functions:
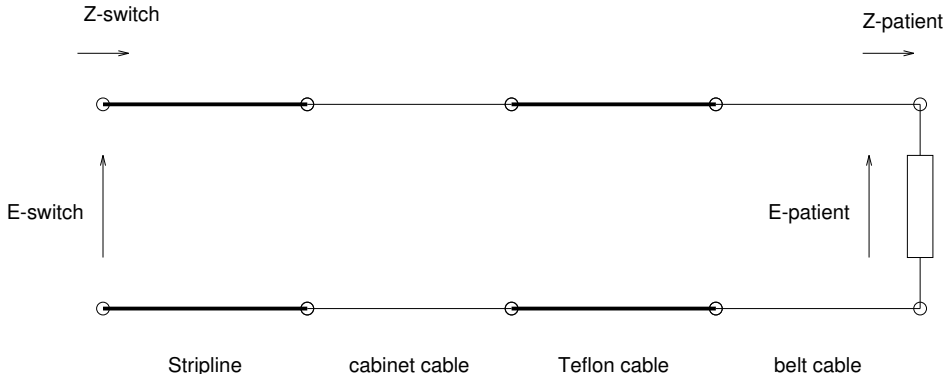
Figure 2.4: Sections of a transmission line connecting Z_{pat} to the switchboard.

▷   impedance transformation and
▷   duty-cycle control of the output signal.

Every switchboard can connect one last-stage power amplifier to one to four transmission lines. A schematic illustration of the switchboard is given in figure 2.5. The switches are controlled by the embedded controller.

For efficient energy transport through transmission lines, it is important that the impedances and lines be matched. In the TOP system, the transmission lines are terminated at the patient side (away from the switchboard) by the electrode impedance Z_{pat}, which is in the order of $(30 - \mathrm{j}600)\,\Omega$, corresponding with an electrode-tissue capacitance of about 10 pF.

The transmission line connecting the patient to the generator system consists of several sections, as is shown in figure 2.4. The electrode impedance Z_{pat} is transformed to an impedance Z_{sw} at the switch, over the transmission line connecting it to the switch. The impedance level at the switches on the switchboard is $(800 + 0\mathrm{j})\,\Omega$.

Alternatively, we can adopt the point of view that the impedance at the switch is transformed towards the patient, where it should be matched to the electrode impedance. If the electrode impedance is not compatible with the transformed switch impedance, it should be manipulated with small inductors so that a reasonable match results.

A more detailed schematic of the switches at the switchboard is given in figure 2.5. The $50\,\Omega$ termination resistance is connected to the transmission line in

Table 2.1: The properties of the transmission lines used in the MECS system.

line segment	ϵ_r	α [dB/m]	Z_0 [Ω]	length [m]
strip line switch-generator	2.2	0.1	110	0.075
cabinet cable	2.03	0.15	50	0.37
Teflon cable	1.791	0.06	50	2.505
belt cable	2.03	0.15	50	0.5–1.0
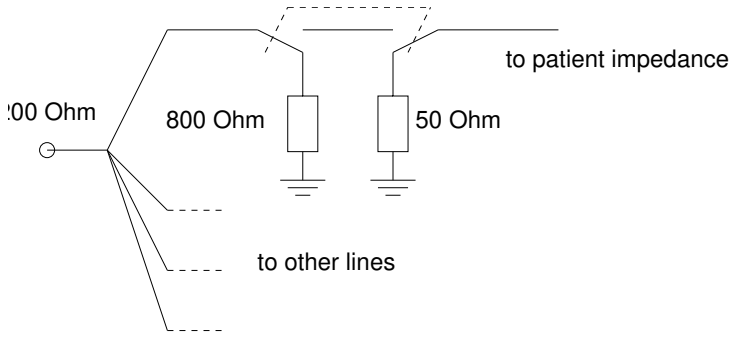
Figure 2.5: Switch connecting the power amplifier to the transmission lines.

the power-off situation. The terminator is matched to the characteristic impedance of the transmission line and transforms as a $50\,\Omega$ resistance towards the electrode, effectively preventing cross coupling between electrodes.

The actual switch used for the duty-cycle modulation at the switchboard is a biased diode.

2.6 Matching and efficiency

The power transfer from the last-stage amplifiers to the patient impedance (the applicator) the transmission line can be approached using circuit theory. A summary of the procedure is given below.

The expression for the transformation of an impedance over a given length of transmission line used here is:

$$Z_1 = Z_0 \frac{Z_2 \cosh \gamma x + Z_0 \sinh \gamma x}{Z_0 \cosh \gamma x + Z_2 \sinh \gamma x}, \tag{2.1}$$

where

Z_0 is the characteristic impedance of the line;
Z_1 is the transformed terminating impedanc;
Z_2 is the terminating impedance;
x is the length over which the impedance is transformed;
α is the attenuation constant of the line;
$\beta = 2\pi\sqrt{\epsilon_r}/\lambda_{\text{free}}$ is the phase constant;
$\gamma = \alpha + j\beta$ is the propagation constant of the line.

A potential difference can also be transformed over the line:

$$E' = E \left[\cosh\gamma x + \frac{Z_0}{Z_2} \sinh\gamma x \right] \tag{2.2}$$

where

E' is the transformed potential difference;
E is the untransformed potential difference;

The power dissipated in an impedance Z with (complex) potential difference E over its terminals is:

$$P = \text{Re}\,(EI^*) = \text{Re}\left(E\frac{E^*}{Z^*} \right) = EE^* \,\text{Re}\left(\frac{1}{Z^*} \right). \tag{2.3}$$

Using the expressions (2.1) and (2.2) a patient impedance with a unit potential at its terminals is transformed from the end of the belt cable to the start of the strip-line where the lines are connected in parallel. By comparing the power at the patient impedance i and at the start of the associated strip line, the power transfer $\eta_{p,i}$ of the line is calculated. It is assumed that the power transfer the other way around has the same value because of the linearity of the transmission lines.

If the four transmission lines are perfectly matched, their combined impedance Z_{rep} is $200\,\Omega$. We may neglect the influence of the switches and their connecting lines, which have been compensated for in the circuit design, and assume that the transformer between the $200\,\Omega$ point and the $50\,\Omega$ transmission line to the power amplifier is loss-less. Then, the power reflection at that point is

$$\zeta = \left| \frac{Z_{\text{rep}} - 200}{Z_{\text{rep}} + 200} \right|^2. \tag{2.4}$$

The total power available at the switchboard is $P_{avail} = P_{generator}(1 - \zeta)$, which is related to the potential E at the '200 Ω point' (which might also be called a 'Z_{rep} point') by equation (2.3).

The power allocated to line i is then $P_i = EE^* \operatorname{Re}(1/Z_{sw,i}^*)$. Thus, the proportion between the total power available in all parallel impedances to the power dissipated in impedance i is

$$c_i = \frac{P_i}{P_{avail}} = \left(\operatorname{Re} \frac{1}{Z_{sw,i}^*} \right) \left(\operatorname{Re} \frac{1}{Z_{rep}^*} \right)^{-1}. \tag{2.5}$$

The *absolute power* effectively available in the patient impedance i is the product of the line efficiency $\eta_{p,i}$ of line i, the total power available for all channels on this switchboard P_{avail}[2] and the fraction of the total power available (expression 2.5) for line i, c_i:

$$P_{pat,i} = P_{avail} \cdot c_i \cdot \eta_{p,i}. \tag{2.6}$$

The real system efficiency differs from the calculated values: the transmission line parameters are uncertain and it is hard to quantify the losses due to connectors and transformers. However, the behaviour of the system is qualitatively well understood and experiments confirm the general picture that emerges from the simulations.

2.7 A practical matching method

To estimate the system efficiency, a model of the power transfer along the cascade of transmission lines in the system was written in C++. The physical properties of the transmission lines used in the model are summarised in table (2.1). These properties were taken from manufacturer literature; due to aging and differing ambiance the real properties are probably somewhat different.

The transmission line transforms the electrode impedance along a spiral-like path through the impedance plane. The locus of an impedance of $(55 - 343j)\,\Omega$[3] transformed along a transmission line system with the properties given in table 2.1 is shown in figure 2.6.

----

2. The power amplifiers can deliver about $P_{generator} = 20$ W. The generator power is limited by the current level at the switching diodes on the switch boards.
3. This value was chosen to match a relatively long belt cable, to include the path for shorter cables.
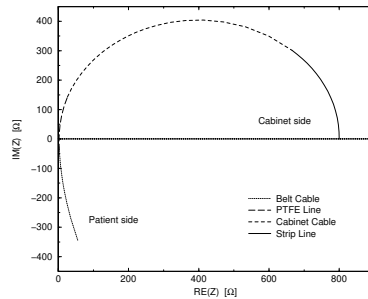
Figure 2.6: Patient impedance transformed towards the switchboard along the transmission lines. Line is ideally matched to patient impedance.
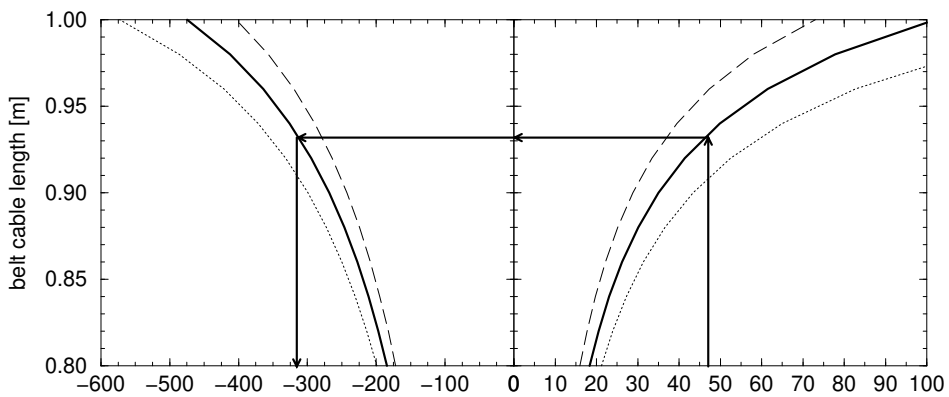
Figure 2.7: A procedure by which the belt cable length and the 'ideal' imaginary part of the patient impedance can be found, given the real part of the patient impedance. The thick curves belong to the 'mean' cable parameters which are used for the calculations. The dashed and dotted lines belong with the same cable parameters—only the relative permittivity of the PTFE cable is varied by $\pm 2\%$.
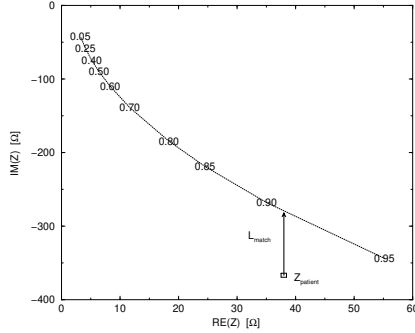
Figure 2.8: The relation between an ideally matched patient impedance, which lies on the locus of the transmission line, and a (mismatched) real patient impedance, which has a different imaginary part. The difference is made up for using a coil with self-induction L_{match}. Along the locus of the ideally matched impedance, the length of the belt cable (in m) is shown.

We now turn to a description of the matching process for a given electrode impedance Z_{pat} (see figure 2.7).

First, based upon the real part of Z_{pat}, the length of the belt cable is selected (upward arrow in figure 2.7: read off belt length).

The belt cable length found in this way, the left-hand part of figure 2.7 is used to find to the reactive part of the ideally matched Z_{pat}. The difference between the reactive part of this ideal Z_{pat} and the actual value of the reactive part of Z_{pat} must be made up for with an additional inductance at the patient side, which is calculated as follows (see also figure 2.8):

$$L = \frac{\text{Im}\left(Z_{pat}^{actual} - Z_{pat}^{perfect}\right)}{2\pi f}. \tag{2.7}$$

This simple procedure allows the selection of a belt cable and a matching inductance for the given Z_{pat}.

In practice a mismatch between the transmission line system and the patient impedance remains. One reason is that it is not so easy to precisely predict or measure the impedance of each electrode; another, very practical, reason is that
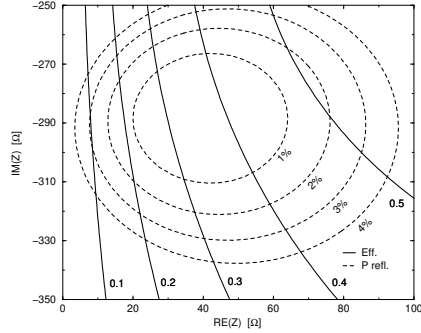
Figure 2.9: Contours of the total system efficiency (drawn contours) and power reflection (ζ, dashed contours) as as function of the actual impedance connected to all four active transmission lines of a single switch board. The belt cable length in this instance was 91.5 cm. The SWR is a steeper function of the mismatch than the power reflection, which is shown in the figure. Contours beyond 5 % power reflection are omitted for clarity.

only a limited number of connection cables, of discrete length, can be kept at hand. Therefore, the sensitivity of the system efficiency to mismatches between the patient impedance and the transmission line system was investigated.

Assuming a realistic transmission line configuration it is possible to evaluate system power transfer efficiency for a range of electrode (patient) impedances around the ideal patient impedance. Numerical experiments have shown that the efficiency of the system (assuming reasonable matching) is roughly proportional to the real part of the patient impedance. Also, near good matching, the power reflection is a function of the 'distance' of the patient impedance to the ideally matched patient impedance (the contours are more or less circular). Experiments based on calorimetry at the terminal side and forward power measurements in front of the switch boards showed total efficiencies consistently lower than found in figures like 2.9 by about 30 % (of the efficiencies).

Chapter 3

Treatment planning for the multi-electrode current-source IHT system

In order to optimally exploit the clinical potential of the MECS IHT system, a treatment planning system is necessary. Such a planning system has three main fields of application:

▷ simulation of the physical behavior of the MECS system in complicated anatomies, with discrete vasculature in the treatment volume;

▷ finding optimal values for the treatment parameters, such as catheter tracks, electrode length and insertion depth in the catheters and electrical phase of the electrodes;

▷ a-posteriori evaluation of data acquired during treatment in order to learn from treatments and improve treatment strategy.

The set of software tools that is loosely called 'the treatment planning system' contains

▷ tools for the conversion of CT and MR data to formats which can be used by the programs of the planning system, including segmentation into tissue types and the assignment of relevant tissue properties;

▷ an electrical model of the MECS system used to calculate the power density deposited in the implant volume during treatment;

▷ a thermal model that is used to estimate the transient and steady state temperature distribution in the treatment volume;

▷ a control program that emulates the action of the MECS-control system using temperature samples taken from the temperature distribution calculated by the thermal model;

▷ tools for evaluation of calculated temperature and electrical potential distributions and for visualisation of results;

▷ tools for setting up the data structures needed for the simulations.

In this chapter the different parts of the planning system will be investigated in a superficial way. The focus will be on the reasons for setting up the models and tools the way they were build.

A note concerning the software used to build the planning system is in order. The programs were built using various freely available programs. Most editing and debugging was done with the GNU Emacs editor and the GNU gdb debugger, which can be used from Emacs. Prototype software was initially built using Perl, a versatile and free tool which is good at pattern matching and operating system specific tasks. Perl made it possible to try out new functionality quickly. It was used less often after reliable and versatile class libraries became available, which provide good facilities for handling the data structures often used in the planning system. The C++ compiler used to build the final programs was GNU g++. The STL class library developed at Hewlett-Packard is used to provide basis classes for managing lists and other basic data types. Voxel data sets are stored on disk using the HDF (Hierarchical Data Format) library. The RCS and CVS revision management systems were used to ease development the software in a team without constantly tangling up different revisions of the source code. The planning system was developed on Silicon Graphics workstations running the Irix operating system.

3.1   Power deposition

For any practical hyperthermia planning system it is necessary to have a method of computing the power deposition that the system would actually produce when used in a given treatment configuration, in a given anatomy. Regarding electrical properties, a patient is not homogeneous and the description of the electrical boundary conditions and the source terms is difficult. As a further complication, the geometry of the IHT implants of the MECS system can be quite complex (for instance, electrodes can be curved). This rules out an analytical approach of this problem, except in sample problems used to verify the models. Thus, we must resort to numerical methods for the calculation of the power deposition. Two-dimensional modelling is not sufficient because of the importance of the third (longitudinal) direction in the implants. Three dimensional models for regional hyperthermia have been presented by, amongst others, Sullivan (1993); Paulsen et al. (1992); Hornsleth (1996); Zwamborn et al. (1992); Jia et al. (1994). Sowinski (1992) and Chen and Gandhi (1989) have published on quasi-static models for low frequency RF techniques.

The current diagnostic volume scan techniques (CT and MR) produce ample data from which the tissue properties may be deduced at a resolution of millimetres. This 3D data is invaluable for the accurate prediction of the power deposition in the volume. Target volumes for the MECS IHT technique fit well into a cube of $10 \times 10 \times 10$ cm; thus, the planning system should be able to handle volume sizes of some $100 \times 100 \times 100$ voxels, at a resolution of 1 mm. The practical impossibility of modelling the whole body[1] makes it necessary to adjust the boundary conditions of the calculation volume in such a way that the approximate solution of the field equations in the implant is still near the true solution in the volume of interest.

A specialised finite difference quasi-static (27 MHz) SAR model (De Bree et al., 1996b) capable of handling heterogeneous tissue properties and the steep gradients of the electric field around the electrodes was developed. During the development of the model special precautions were taken to allow for the use of curved electrodes and to make the model insensitive to variations in the resolution of the voxel grid that represents the (dielectric) anatomy.

3.1.1 The SAR model: `quasar`

The electrical model (`quasar`) described in this chapter solves a partial differential equation (PDE) arising from the Maxwell equations describing the electromagnetic field using a finite-difference method. A big advantage of using a finite-difference approach is it's compatibility with the type of volume data that is acquired by CT and MR diagnostic scans. Finite difference methods have been in use for decades and the method is well-established.

The model makes use of a `C++` class library which is shared with the thermal model.

De Bree et al. (1996b) gives a detailed explanation of `quasar`.

3.1.2 SAR calculation; basics

The goal of the electrical model is to predict the spatial distribution of the energy deposition in human tissues during treatment with the MECS Interstitial Hyperthermia system. To do this, the electrical potential field of a set of current sources,

---

1. It is sometimes argued that this could be done using finite element methods, because they allow variation in the density of grid points. However, finite element methods are handicapped by the difficulty of grid generation and of correctly specifying tissue properties with the amount of detail necessary. Finite difference methods and finite element methods are strongly related in a mathematical sense. The choice between the methods was made by comparing computational efficiencies and practical usability.

representing actual electrodes in tissue, is calculated. The use of this simplified model is justified in chapter 4. In the finite-difference model, the electrodes are modelled as contiguous groups of voxels with a non-zero current balance.

Starting from the Maxwell equation

$$\boldsymbol{\nabla} \times \mathbf{H} = \mathbf{J}_f + \frac{\partial}{\partial t} \mathbf{D} \tag{3.1}$$

we add a term for the injected current (which is produced by a source outside our problem domain) so that we may write (De Bree et al., 1996b)

$$\boldsymbol{\nabla} \times \mathbf{H} = \mathbf{J}_{inj} + \mathbf{J}_f + \frac{\partial}{\partial t} \mathbf{D} \tag{3.2}$$

and then, moving to the Fourier domain, with $\partial/\partial t \to i\omega$, $\mathbf{J}_f = \sigma\mathbf{E}$, $\mathbf{D} = \epsilon\mathbf{E}$ and, using $\boldsymbol{\nabla}\cdot(\boldsymbol{\nabla}\times\mathbf{H}) = 0$, we find the continuity equation

$$\boldsymbol{\nabla}\cdot\mathbf{J}_{gen} + \boldsymbol{\nabla}\cdot\mathbf{J}_{inj} = 0 \tag{3.3}$$

where the definition $\mathbf{J}_{gen} = (\sigma + i\omega\epsilon)\mathbf{E} = \kappa\mathbf{E}$ is used, following Sowinski and van den Berg (1990). Equation (3.3) is the basic PDE governing the electrical problem.

In a source-containing region which is small compared to the wavelength of the EM-radiation we may write (note that $\mathbf{J}_{gen} = -\kappa\boldsymbol{\nabla}V$)

$$-\boldsymbol{\nabla}\cdot\kappa\boldsymbol{\nabla}V + \boldsymbol{\nabla}\cdot\mathbf{J}_{inj} = 0 \tag{3.4}$$
$$-\boldsymbol{\nabla}\cdot\kappa\boldsymbol{\nabla}V + \dot{\rho}_{inj} = 0 \tag{3.5}$$

where κ is the admittance, σ is the conductivity, ω is the angular frequency of the EM-fields, ϵ is the permittivity and V is the (complex) potential. $\dot{\rho}_{inj}$ is the current injection term.

Given the electrical properties of the material and the potential field the dissipated power density in the material may be calculated. A convenient formulation in terms of the current density is

$$\dot{w}(x,y,z) = \frac{1}{2}\frac{\sigma(x,y,z,)}{|\kappa(x,y,z)|^2}|\mathbf{J}(x,y,z)|^2\,. \tag{3.6}$$

The relation between the power density and the *SAR* is given by

$$SAR = \frac{\dot{w}(\mathbf{r})}{\rho(\mathbf{r})}\,. \tag{3.7}$$

The electrical problem, represented as a partial differential equation, is completely defined by the material properties and the electrical boundary conditions (if we consider the sources as internal boundaries). In a phantom, or a real body, the electrodes of the MECS system are placed inside plastic tubes (catheters). The electrodes are connected to an RF source which is considered to fix their potential. The diameter of the electrodes is near 1.6 mm. The finest uniform grid spacing that can currently be handled, given the physical size of the volume we are interested in and the limits of our computers, is about 1 mm. This means that the fine structure of the electrodes, which contain layers with a thickness in the order of 0.1 mm, can not be modelled in the relatively coarse planning grid. Thus, it was decided to model the electrodes as current sources which inject current directly into grid voxels. This induces a discretisation error in the field solution[2], which is corrected by changing the uncorrected potential distribution by an amount determined using a fit of the potential outside the current injection volume against an approximate analytical solution of the field (De Bree et al., 1996b).

3.1.3 SAR calculation; transformation to diffusion problem and discretisation

The problem of calculating the $SAR(\mathbf{r})$ is solved by finding the solution to a problem slightly different from equation (3.5). Instead of finding the solution of the elliptic problem (3.5), we try to find the steady state of the PDE

$$-\nabla\cdot\kappa\nabla V + \dot{\rho}_{inj} = \frac{1}{-F(\mathbf{r})}\frac{\partial V}{\partial \tau},\tag{3.8}$$

of which the LHS (and the RHS) should go to zero for large τ. This is a relaxation problem. The function $F(\mathbf{r})$ is deliberately chosen to maximize the convergence rate of the model, in order to minimize the number of iterations to steady state (Sowinski and van den Berg, 1990). The PDE (3.8) is discretised on a finite difference grid and solved using a DuFord-Frankel scheme (De Bree et al., 1996b). The physical properties and $F(\mathbf{r})$ are constant over the volume of any voxel, but every voxel may have different material properties associated with it.

3.1.4 High resolution calculations

The program used for solving the electrical problem was also used for investigation of the detailed SAR distribution in the neighbourhood of the electrodes. In

---

2. The fact that the electrodes are modelled as current sources also introduce an error. The errors introduced by the current source assumption are investigated in chapter 4.

that case, a resolution in the order of 0.01 mm/voxel was used. No current source term was used so that the influence of the current source assumption could be investigated. An account of the methods and results of the high-resolution work is given in chapter 4.

This problem was also approached using specialised analytical models exploiting the cylindrical symmetry of the MECS applicator. The background of these specialised models is explained in chapter 4. However, they are not part of the planning system.

3.2   The thermal model: **heatran**

Temperature distributions occurring during hyperthermia treatment are strongly influenced by local blood flow. For the prediction of the local thermal effects of large vessels, giving rise to possibly serious temperature inhomogeneities, discrete modelling of these vessels is needed. Only very simple vessel geometries allow an analytic approach. These relatively simple situations are of theoretical interest, because they can be used to test numerical models of heat transport in tissue (Kotte et al., 1996d; Van Leeuwen et al., (submitted-b,s). A flexible numerical model which can handle discrete blood vessels is required for the calculation of temperature fields in the presence of convoluted vessel structures as obtained for individual patients and of complex power deposition patterns. Chapter 1 contains a short account of the historical development of the thermal models used in the group in Utrecht.

The starting point for the heatran thermal model now used for discrete vessel modelling was the versatile discrete vessel model by Mooibroek and Lagendijk (1991), which allowed vessels to curve and to branch. Initially, it was planned to use this model in the IHT planning system. In the Mooibroek model, the vessels are an inseparable part of the modelled volume: some voxels are 'vessel voxels'; their temperatures reflect local vessel temperatures. Other voxels are tissue voxels. Such a model has big problems managing vessel junctions and vessels of very different diameters and blood speeds[3]. This was the most important reason for considering other approaches.

---

3.   The Mooibroek and Lagendijk (1991) model was written in FORTRAN; the management of the heat exchange between a non-trivial vessel network and a tissue volume is an overwhelming task and FORTRAN provides little structural means for attacking the problems occurring in such situations.

When thinking about a new strategy, building on our experience with the older models, we made up a list of properties the new model should possess:

▷   the concept should allow the specification of complicated vascular geometries in such a way that there would be little or no human intervention necessary to produce a set of data structures representing the problem in a physically correct way;

▷   the vascular structures should be defined independent of the tissue voxel dimensions and grid orientation, to ease the use of anatomical data from different sources (and also to allow multi-grid techniques for solution of the heat transport equations later on);

▷   the physical interaction between the vascular structures and the tissue should be clearly defined and easily adjustable;

▷   the heat transport equation solved by the model should be quite generic[4], in order to be able to compare results of different approaches (for example heat sink versus k_{eff});

▷   the model should use voxel grids and finite difference techniques.

In short, we wanted to build a flexible, adaptable and efficient model, which could be sustained by multiple developers during extended periods of time and would be well-suited for research purposes.

In our opinion, the heatran model successfully addresses these issues. In the model, vessels are represented by tree structures [5] of parametrised tracks, independent of the tissue grid. The vessel trees, given a particular tissue grid, automatically figure out which voxels are directly involved in the tissue-vessel interactions. Thus, vessel (blood) temperatures are maintained in separate structures outside the tissue voxel grid. The interface between these structures and the tissue grid is clearly localised in the code, and easily adjustable[6].

For the calculation of the heat flow between tissue voxels and a vessel an analytic approximation of the radial temperature profile near the vessel is used. This approximation is exact for a cylinder symmetric stationary temperature distribution

---

4.   The handling of non-isotropic tissue properties is not addressed here. Some heat transport theories use such properties for the description of convective heat transport by small vessels (Crezee et al., 1993).

5.   According to Knuth (1973) (p. 310): 'Any hierarchical classification scheme leads to a tree structure.'

6.   Interestingly, it turns out that the structures devised to model heat transfer between vessel segments and the tissue grid can be easily adapted to model the thermal behaviour of so-called ferromagnetic thermal seeds, an application that was definitely not in our minds when the model was initially set up.

around the vessel and thermally developed flow. If model conditions conform to the assumptions made in the calculation of the tissue/vessel interaction (straight vessels embedded in tissue cylinders) and the tissue grid has voxel dimensions in the order of (or smaller than) the smallest vessel diameter, the computer program produces very accurate results (Kotte et al., 1996d).

Further investigations have shown that the new model also produces useful results if the vascular structures are embedded in voxel grids with low resolution compared to the vessel size and for curved vessels (Van Leeuwen et al., 1996).

The model is written in C++; the class (object) hierarchies that can be build in that language allowed the construction of elegant and versatile software[7].

3.2.1   Description of the thermal model

Only a brief explanation of some key concepts of the model will be given here; for a more comprehensive description the reader is referred to Kotte et al. (1996d).

In heatran, discrete vascular trees[8] are composed of vessel segments, which, in turn, are defined as vessel sections between branching points. In the model the vessel segments are represented using parametric curves in space with a diameter that may vary along the track of the vessel. Once again, it is emphasized that the segments are maintained as structures *separate* of the tissue grid. The vessel segments are split up into subsections called buckets, each one having it's own (mixing cup) temperature. The interaction between vessel segment and tissue grid is localised at the bucket level. The temperature profile along a segment can be thought of as the temperatures of the buckets constituting the segment, ordered along the track of the segment (the buckets of heatran are like beads on a string).

The bucket temperature represents the mixing-cup temperature in a slice of a vessel. In heatran, the radial blood temperature profile is assumed to be developed everywhere in the discrete vessel tree; as a consequence, the interaction between the tissue wall and the blood may be described using a fixed Nusselt number. An incidental advantage of this simplification is the fact that it facilitates analytical work, which serves in testing the numerical model. The question remains to

---

7.   Lippman (1991) writes: 'By creating new types to describe the problem domain, C++ allows the programmer to write applications with much less concern for the various bookkeeping aspects that make programming tedious.'

8.   The topological properties of the trees of heatran strongly resemble those of real trees. For instance, so-called shunts can not be represented at this moment. It would not be extremely difficult to implement these structures, though.

what extent this approach allows the modelling of actual vessels. Further work is going on in this field. A comparison of different, also more detailed, interaction descriptions is given by Dutton and Roemer (1994).

The heat flow rate from the tissue into a bucket is calculated using an analytic result: The stationary heat flow rate density into a vessel section embedded in tissue with cylinder symmetric boundary conditions at distance R and with uniform power distribution is given by Kotte et al. (1996d)

$$
\phi|_{r=r_{ves}} = -\frac{1}{\frac{2k_{tis}}{Nu\,k_b} + \ln\left(\frac{R}{r_{ves}}\right)} \left\{ \frac{k_{tis}}{r_{ves}} \left(T_{tis}(R) - T_{mix} \right) + \right.
$$

$$
\left. Pr_{ves}\left(\frac{1}{4}\left(\left(\frac{R}{r_{ves}}\right)^2 - 1 \right) + \frac{1}{2}\ln\left(\frac{R}{r_{ves}}\right) \right) \right\}. \tag{3.9}
$$

The total heat flow rate is the integral of this density over the vessel wall:

$$
\Phi = -\int \phi|_{r=r_{ves}} \cdot \hat{n}\ d\Omega \qquad [\text{W}]\,. \tag{3.10}
$$

The heat flow rate is estimated using the temperatures of tissue voxels near the vessel. For the implementation of the heat flow estimation and the heat exchange itself, two sets of voxels are assigned to each bucket, as illustrated in Figure 3.1. The *exchange set* comprises all voxels that have their centre inside the bucket or (for small vessels) contain the heart line of the bucket, and neighbour at least one voxel of surrounding tissue. The *estimation set* consists of the voxels in the surrounding tissue that neighbour at least one exchange set voxel.

For all voxels in the estimation set an estimate for the heat flow rate density can be calculated using equation (3.9). The estimates are averaged and multiplied with the bucket surface to yield the heat flow rate into the bucket. Using this heat flow rate the new bucket temperatures are calculated. In order to guarantee heat conservation, the heat that flows into the buckets is removed (in equal amounts) from the exchange set voxels. Evidently, the temperatures of the exchange set voxels do not represent any actual temperatures in the treatment volume[9].

The transport of blood *in the vessel segment* is modelled as follows. First, to account for the changing interaction of the moving blood with the tissue, heat flow

---

9. When temperature grids (distributions) are used for the estimation of temperature/volume histograms, the vessel wall temperatures are first drawn into the volumes at the vessel locations. For most volumes of interest, this introduces an insignificant discretisation error in the histograms.
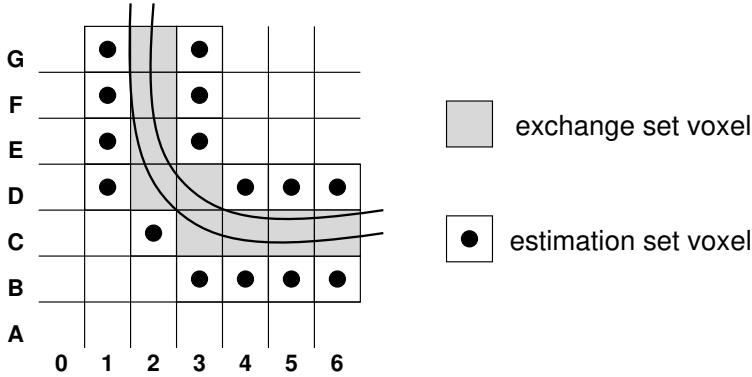
Figure 3.1: A vessels with associated sets of voxels.

rates for adjacent buckets are used to estimate the average heat flow rate during a time step. Next, the resulting temperature profile is shifted the appropriate distance in the direction of flow. During this procedure the shifted temperature profile is projected onto the new bucket positions by interpolation. This procedure allows a relaxation of the relation between the time step, the volume flux and the bucket volumes (Kotte et al., 1996d).

3.3   Simulation control software

Generally speaking, the results from the simulations should reflect the clinical choices made for a treatment. If a clinician sets a limit to the maximum temperature in a target volume, the treatment planning system should respect that limit. This restraint is relaxed when we are only interested in steady state temperature distributions—we allow intermediate states which do not honor physical limits of the patient or the treatment system.

The simulation control part of the planning system is used during the simulation of the behaviour of the MECS system during treatment. It is responsible for the control of the currents assigned to the electrodes in the implant model. As such, it simulates part of the functionality of the embedded controller and workstation components of the *real* MECS system. In figure 3.2 a schematic view of the simulation process is given.

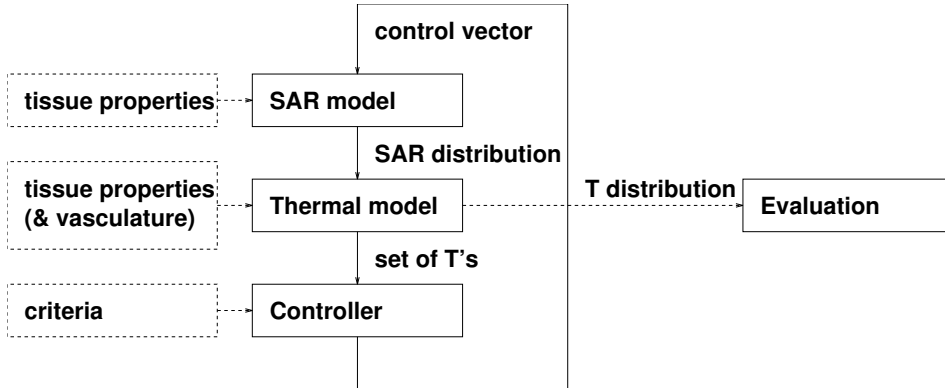Two problems have to be solved to obtain a well-working control mechanism.

```
                         ┌─────────────────────┐
                         │    control vector   │
                         └──────────┬──────────┘
                                    │
┌ ─ ─ ─ ─ ─ ─ ─ ─ ┐        ┌────────▼─────────┐
  tissue properties ┄┄┄┄┄▶ │    SAR model     │
└ ─ ─ ─ ─ ─ ─ ─ ─ ┘        └────────┬─────────┘
                            SAR distribution │
┌ ─ ─ ─ ─ ─ ─ ─ ─ ┐        ┌────────▼─────────┐     T distribution   ┌──────────────┐
  tissue properties ┄┄┄┄┄▶ │  Thermal model   │┄┄┄┄┄┄┄┄┄┄┄┄┄┄┄┄┄┄┄▶ │  Evaluation  │
  (& vasculature)  │        └────────┬─────────┘                      └──────────────┘
└ ─ ─ ─ ─ ─ ─ ─ ─ ┘            set of T's │
┌ ─ ─ ─ ─ ─ ─ ─ ─ ┐        ┌────────▼─────────┐
  criteria         ┄┄┄┄┄▶ │    Controller    │
└ ─ ─ ─ ─ ─ ─ ─ ─ ┘        └──────────────────┘
```

Figure 3.2: Schematic overview of the control process leading to a stationary temperature distribution.

The first problem is the selection of a strategy for adjusting the electrode currents of the MECS electrodes. A control algorithm should take into account the history of the temperature near the electrodes, the history of the electrode currents and the relation between that temperature and the electrode excitation. Control theory offers a wide variety of feedback control algorithms, ranging from on-off controllers to PID controllers and (multiple input, multiple output) adaptive controllers. However, because we were not primarily interested in the selection of optimal control mechanisms we have implemented a number of simple control strategies which allow us to find steady state solutions and which are not complicated by strict adherence to physical limits of the treatment system [10].

The current control program uses the currents in the electrodes from the previous control loop iteration and the new and old simulated temperatures at certain control points in the temperature volume. At this time, two useful algorithms for current control have been implemented:

▷   based on the (reasonable) assumption that there is a proportional relation between the *square* of the output current I of, and the temperature T near an electrode, the new current I_{new} is calculated from from the old

─────────

10. For instance, the control systems act as if they have unconstrained (but positive) power available. Real hyperthermia systems do not possess this property. This implies that transient temperature distributions found using these algorithms may not represent actual transient behaviour of the system. For clinical purposes, the steady state system settings should be checked for compliance with the physical system limits.

temperature T_{old}, the old current I_{old} and the set point temperature T_{set} as follows:

$$I_{new} = I_{old} \sqrt{\frac{T_{set}}{T_{old}}}.$$

This simple approach turned out to be surprisingly stable and robust, if the time steps between iterations of the control program are kept small enough.

▷   Simple on-off control (full scale) of the electrode current. This allows fixing the maximum current, but leads to much slower convergence to steady state and less stable results.

The second problem   is choosing *which* temperature data should be used to control the electrodes. Two alternatives are considered here:

▷   associating a measurement position fixed in space with every electrode; this is what is physically realizable with a small number of temperature measurement points inside the catheter;

▷   at every iteration, selecting the highest temperature in a special set of voxels; this allows the user to fix the maximum temperature in a simulation (for all practical purposes).

Using the theory from chapter 5, a temperature measurement subject to the thermal effects of the properties of the thermocouple material and the applicator could be simulated. This step has not been made yet.

3.4   Qualification of temperature distributions

In this section, a description will be given of the way temperature distributions are evaluated in the current treatment planning system. To illustrate the contrast between the way the temperature distribution is qualified in the planning system and in practice, a short digression on one of the problems of temperature measurement follows.

Since reliable non-invasive temperature mapping systems with good spatial resolution do not exist, little information is available on the details of the temperature distribution in treatment volumes. In case of (invasive) temperature measurement devices present in the treatment volume, one has to be very careful when drawing conclusions on the distribution of temperature in the volume, based on the readings of these devices. In fact, a spatial sampling of the temperature distribution

is performed. If the set of sample is too sparse or if it's point spreading is insufficiently random, problems may arise. For instance, if a disproportionate fraction of the set of measurement devices is located near sources of heat, an overestimation of the average temperature in the volume is easily made. In this way, an optimistic picture of treatments could arise—however, the effect of such treatments is less than expected. It is hard to obtain a good estimate of the real temperature distribution in a perfused volume. Because of the small numbers of measurements, it is important to make very efficient use of the data available.

The RTOG has issued a quality guideline for IHT, which rules out temperature measurement inside treatment catheters for evaluation purposes (Emami et al., 1990). In our opinion, that guideline is somewhat conservative. Temperature data from treatment catheters *can* be used for some evaluation purposes, like maximum temperature estimation and, if sufficient precaution is taken, also for estimation of other characteristics of the tissue temperature. This issue is touched upon in chapter 5. The temperatures measured in the catheters can, and must, be used for feedback purposes during treatment.

We now turn to a description of the way in which the temperature distribution is evaluated in the treatment planning system.

3.4.1   Statistical description of temperature distributions

One of the most attractive ways of describing temperature distributions is through estimation of statistical moments of the temperature data. Basically, we view the temperature in a volume as a stochastic variable of the position. From this view, we can define a probability density for the temperature. One of the popular views of an ideal hyperthermia treatment, a uniform temperature in the treatment volume, can than be translated as: the probability distribution of the temperature is a Kronecker delta function at the desired treatment temperature. Such a mathematical approach eases discussions on the quality of temperature distributions. In practice the temperature is never completely uniform in the treatment volume. In such cases, the probability density becomes wider spread and we can talk about certain points in the (integrated) probability density, or about average temperatures[11].

---

11. There is an important problem here: temperature distributions which differ significantly from a clinical point of view can have identical temperature/volume histograms. However, clinical trials show significant correlation between clinically measured parameters of the probability density of the temperature and the outcome of the treatment. This is one of the reasons why temperature/volume histograms are in use.

The discrete CTVH is defined as

$$CTVH(T) = \sum_{i=0}^{k} P(T_i, \Delta T),$$
(3.11)

where k is the index of the temperature interval for which $T \in \{T_k \pm 0.5\Delta T\}$ and $P(T_i, \Delta T)$ is the probability that the temperature T at a randomly chosen point in the volume of interest lies in the interval $\{T_i \pm 0.5\Delta T\}$.

Using equation (3.11) we define the clinically used index temperatures T_{10}, T_{50} and T_{90}. A convenient definition of T_η is:

$$CTVH(T_\eta) = \frac{\eta}{100\%}.$$
(3.12)

The value of 100% in the denominator stems from the conversion between volume fraction and percentage of volume and is not interesting.

3.4.2   Estimation of the temperature probability distribution

From the mathematics it follows that the essential quantity for a statistical description of the temperature distribution is the temperature probability distribution in a certain region of interest.

If an analytical solution of a temperature distribution is at hand, that can be used to construct the real temperature probability distribution.

In clinical practice, the temperatures measured during treatment are used to make an estimation of this probability density. Most measurement schemes used to date to obtain an estimate of the probability density are problematic, leaving apart the problem that generally, the data points used are gathered over an extended period of time, so that a changing temperature distribution is used to construct a temperature probability density of what is regarded as a single temperature distribution.

Given a clinical set of temperature measurements, the different measurement points are weighted in an attempt to estimate the temperature probability distribution. Using weights only related to geometrical properties of the set of measurement points (for instance using the measurement positions to generate a Voronoi tessellation (Okabe et al., 1992) and using the volume of the cells as the weights of their data values) does not guarantee success because the temperature at the

measurement point in such a cell is not guaranteed to be a good estimate of the average temperature in the cell.

Simulated temperature distributions allow a brute force approach to the estimation of the temperature probability density. Here, the TVH is directly constructed from the temperature values in the voxels of the temperature distribution. The number of voxels in a given interval divided by the number of voxels in the volume of interest gives a good approximation of the probability density at the middle of the interval, if we have a reasonable number of voxels in the VOI.

3.4.3   Volumes of interest

The term volume of interest (VOI) has surfaced some times already. This concept allows us to discriminate between, for instance, the target volume and its surroundings, or the vessels and their direct surroundings and the rest of the target volume.

A precise definition of a volume of interest divides space in two disjunct regions. In principle, the two regions themselves do not *have* to be contiguous—for instance, a volume of interest might be the inter space between the surfaces of two concentric balls with differing radius, or the (possibly unconnected) parts of a target volume where the temperature is above a certain level.

A specialised tool for the definition of *convex* regions[12] of interest is *the convex hull*. Convex hulls are used to define the boundary of the smallest convex volume which fits around a given set of points in space. Many algorithms exist for the calculation of the convex hull of a set of points. In the planning system, we have chosen to use a method which results in a set of oriented planes. This makes it possible to expand or contract a convex hull simply by displacing all of it's planes in the direction of their normal. A practical drawback is that it is not trivial to visualise a convex hull defined using this representation. A definition in terms of bounding triangles is more convenient for that purpose, but makes expanding or shrinking the convex hull more difficult.

When doing statistics on data sets, the volume of interest is effectively represented by a mask file. A geometric description of the volume of interest is used to fill in a mask file, which has the same grid properties as the data file subject to statistical analysis. The use of mask files allows set-theoretic operations on the volumes

---

12. A region in space is called convex if any two points in the region may be connected by a single straight line which does not cross the border of the region. A ball is a convex region. A hollow ball is not.

of interest, so that mask volumes can be 'added' or 'subtracted'. This makes it practical to construct complex volumes of interest.

3.4.4   Visualisation

In the planning system, a serious attempt was made to describe all relevant structures in terms of a geometric, parametrised, mathematical representation, as opposed to keeping a menagerie of sets of voxels. Besides the merits of this approach with respect to grid independence and ease of manipulation, this also eases visualisation of the ingredients of the model.

We have used the proprietary Application Visualisation System (AVS) for complex 2D renderings of 3D volumes containing regions of interest, electrode implants and anatomical structures and images (Lagendijk et al., 1995). AVS allows the construction of interfaces between external data structures and AVS's internal structures.

Vessel trees are visualised by building tubes of appropriate diameter along the tracks of the vessel segments of the tree. The tube can be color washed. For instance, a color code indicating the vessel wall temperature can be selected during visualisation.

Iso-temperature (and iso-SAR) surfaces are constructed in AVS using standard modules, some of which can read HDF[13] files and relatively simple custom networks designed for the convenient manipulation of iso-surfaces, slices through the data volume and iso-value contours. The results of these visualisation techniques can be seen in the next chapters of this thesis.

---

13. Voxel volumes are represented in so-called HDF files. HDF is a standard file format that is machine-architecture independent. HDF should not be confused with the Hyperthermia Data Format (also called HDF) which is designed to document regional hyperthermia treatments.

Chapter 4

Numerical analysis of capacitively coupled electrodes for interstitial hyperthermia

4.1 Introduction

Multi-electrode current-source interstitial hyperthermia (MECS-IHT) is a relatively new technique for the application of spatially controlled interstitial hyperthermia (Lagendijk et al., 1995). It employs individually controlled, 27 MHz radiofrequency electrodes inserted into plastic brachytherapy catheters. The principle of current source electrodes has been described by Marchal et al. (1989), Visser et al. (1989) and Deurloo et al. (1991).

In the SAR model used in our interstitial hyperthermia treatment planning system (Lagendijk et al., 1995; De Bree et al., 1995; Kotte et al., 1996b) the electrodes are described as ideal, loss-less, current sources. This chapter focusses both on the realistic physical properties of the MECS applicators and the ideal current source electrode implementation in our SAR model. Specifically, both the influence of the loss angle of the catheter wall material and the influence of the current source assumption is investigated.

4.2 Theory

4.2.1 Architecture of the applicator

The MECS-IHT system employs applicators inserted in plastic catheters implanted in the treatment volume. Each applicator carries multiple independent electrodes and is a complex assembly of metallic and plastic structures. The system operates at 27 MHz. The catheter, into which the applicator is inserted, serves as a dielectric (wall) between the metallic electrodes and the tissue volume. Typical capacitance

is about 5–10 pF/cm. If the dielectric material of the wall is low-loss instead of loss-less, heat will be dissipated in this wall. In figure 4.1 a schematic drawing of the construction of the applicator is shown.
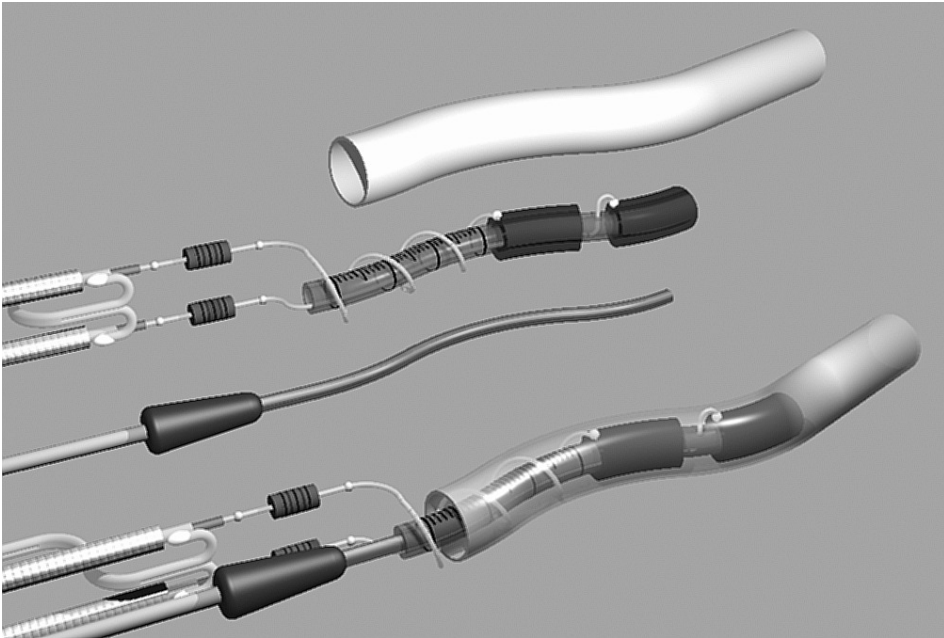

Figure 4.1: Principle of the MECS-IHT applicator. The top part of the illustration shows an exploded view containing (1) the patient catheter, (2) the electrode carrier connected to the transmission lines by matching components (coils) and (3) the thermocouple assembly. The bottom element of the drawing shows the assembled applicator inside the patient catheter. By courtesy of K. Meijer.

The core of the applicator consists of a string of thermocouples in a thin plastic catheter (outer diameter 0.5 mm) inserted into the plastic tube that serves as the carrier of the electrodes. The thermocouples measure temperatures which are used for treatment control. The electrodes are made by applying silver-paint (Acheson, type Electrodag 1415) to the plastic carrier. They are connected to a circuit matching the applicator to the transmission lines of the MECS system by a thin copper wire carrying isolating paint. The power deposition is controlled by varying the duty-cycle of the RF-signal applied to the electrodes. Care is taken to ensure that the wires do not touch; the connecting wires are led both through

Table 4.1: Material properties used in the calculations

material	electrical conductivity $[\mathrm{S\,m^{-1}}]$	relative permittivity	$\tan\delta$
air	10^{-18}	1	n.a.
Nylon (PA11)	$0.18 \cdot 10^{-3}$	4	$3 \cdot 10^{-2}$
polyethylene	$1.20 \cdot 10^{-6}$	2	$4 \cdot 10^{-4}$
Teflon	$1.50 \cdot 10^{-6}$	2	$5 \cdot 10^{-4}$
muscle	0.6	100	4.0
fat	0.2	20	6.6

the lumen and along the surface of the electrode carrying catheter. The electrode carrier is covered by an extremely thin heat-shrinked plastic sleeve (Advanced Polymers) which greatly improves its physical endurance. The outer diameter of the patient catheter is 2.0 mm; the inner diameter is 1.6 mm. The outer diameter of the electrodes is 1.4 mm.

4.2.2   Numerical electrical models

The potential distribution $V(\mathbf{r})$ in the modelled applicator is governed by the Poisson equation (Sowinski and van den Berg, 1990)

$$-\boldsymbol{\nabla}\cdot\kappa\boldsymbol{\nabla}V = 0 \tag{4.1}$$

where $\kappa = (\sigma + i\omega\epsilon)$ is the admittance, σ is the conductivity, ω is the angular frequency of the power signal, ϵ is the permittivity and V is the (complex) potential. Equation (4.1) follows from a quasi-static approximation of the Maxwell equations, which is applicable in this case because the dimensions of the computational volume are small compared to the wavelength in tissue of the 27.12 MHz signal (about 1 m in muscle). Given the potential distribution and the properties of the material, the dissipated power density $\dot{w}$ in the material is calculated as follows:

$$\dot{w} = \frac{1}{2}\,\sigma\,|\boldsymbol{\nabla}V|^2\,. \tag{4.2}$$

This relates to the SAR by

$$SAR = \frac{\dot{w}}{\rho}. \tag{4.3}$$

Equation (4.1) is converted to

$$\frac{1}{-\mathsf{F}(\mathbf{r})}\frac{\partial V}{\partial \tau} = -\boldsymbol{\nabla}\cdot\kappa\boldsymbol{\nabla}V \qquad\qquad (4.4)$$

with the introduction of a pseudo-time τ and a spatially dependent relaxation function F (Sowinski and van den Berg, 1990; De Bree et al., 1996b). Equation (4.4) is solved with an iterative method by marching on in pseudo-time. The relaxation function is introduced to increase the convergence rate when there are large differences in the admittance κ. A suitable choice is $\mathsf{F}(\mathbf{r}) = \sqrt{\kappa(\mathbf{r})}$ (Sowinski and van den Berg, 1990).

In our model we discretised equation (4.4) in space on a rectangular grid with uniform grid spacing (De Bree et al., 1996b). This grid partitions the modelled volume in a large number of rectangular nodes. Each node is assigned a uniform admittance κ. Discretisation in space and pseudo-time leads to a finite difference scheme that calculates the potential in the centre of each node at the next iteration from potentials at the current iteration. When iterating, the potentials in each node converge to a potential distribution which is the solution of equation (4.1).

To investigate the electrical behaviour of the applicator in detail the actual material properties and boundary conditions present in the applicator a block containing the applicator is modelled at a high resolution. The material properties of the applicator and the surrounding tissue in this block are discretised on a rectangular grid. The material properties that were chosen approximate the values present in practical applications of the MECS-IHT system (table 4.1, ESHO task group report 4 (1992)). The nodes that belong to an electrode are fixed at the applied electrode potential. In this chapter, this setup is referred to as the high resolution model.

The maximum practical model resolution is determined by the available computer memory and the size of the volume of interest; the electrical model uses 17 bytes for every node. A workstation main memory of 100 MB will then accommodate about $5 \cdot 10^6$ nodes in the electrical model. To describe the catheter wall the distance between two node centres must be less than or equal to 0.3 mm, making the maximum allowed volume $5 \times 5 \times 5$ cm^3, which will mostly be too small to describe a full implant. More important, this high resolution would also lead to impractical convergence speeds of the model because of the Fourier-limit on the pseudo-time step in the model (De Bree et al., 1996b).

Normally, the goal of a SAR calculation is finding the SAR Distribution Produced by the MECS system in a treatment volume with linear dimensions in the order of

0.1 m at a resolution greater than or equal to 1 mm. For reasons mentioned above, it not feasible to implement the actual boundary conditions on the potential as posed by the electrodes. The high series impedance present in the catheter wall (the origin of the term 'capacitive coupling') produces current source like behaviour of the electrodes (Visser et al., 1989). This behaviour is exploited in our *SAR* model by considering the metal electrode and the plastic catheter together as a current source electrode, with a diameter equal to the outer diameter of the catheter (De Bree et al., 1996b). These current source electrodes are incorporated in the electrical model by adding a current injection term to the right hand side of equation (4.1). Consequently, the copper wires and the generator providing the electrical current are not incorporated in the models. This model approach is referred to as the current source model.

In the current source model the electrode is discretised on the grid: each node whose centre is within the physical boundaries of the electrode is marked as an 'electrode node'. The total current of an electrode is then equally distributed over the electrode nodes and injected in the centre of these nodes. This discrete current injection has no respect for the actual diameter of the electrode; therefore the potential in the electrode nodes generally differs from the actual electrode potential. To estimate the actual electrode potential an analytical solution in the direct neighbourhood of the electrode was proposed (De Bree et al., 1996b). The behaviour of the current source model can be verified by comparing its results with the results of the high resolution model and the analytical model described in the next section.

4.2.3   Analytical model

It is possible to derive important physical properties of the applicator system from a simple analytical model.

A construction of nested coaxial layers forming an infinite long applicator can be described in terms of lumped properties (resistance and capacitance), which is justified because of the small size of the structures with respect to the wavelength.

The replacement impedance of N coaxial capacitors is the sum of the impedances of the individual capacitors. If concentric regions with a homogeneous medium are regarded as individual capacitors, we can write

$$Z = \sum_{i=1}^{N} \frac{1}{2\pi l \kappa_i} \ln \frac{r_{o,i}}{r_{i,i}} \qquad (4.5)$$

where l is the length of the capacitors, κ_i is the admittance of the dielectric in the i-th capacitor and $r_{o,i}$ is the outer radius and $r_{i,i}$ is the inner radius of the i-th capacitor. Combining equations (4.5), (4.2) and (4.3) leads to

$$SAR(r) = \frac{1}{\rho(r)} \frac{1}{2} \frac{\sigma(r)}{|\kappa(r)|^2} \left| \frac{V}{\sum_{i=1}^{N} \frac{1}{\kappa_i} \ln \frac{r_{i,2}}{r_{i,1}}} \right|^2 \frac{1}{r^2} \tag{4.6}$$

where i counts off the different consecutive layers of electrode, air gap, plastic and tissue and V is the electrode potential. Thus, the SAR is proportional to the square of the potential difference in the capacitor and inversely proportional to the radius squared.

4.3   Methods

Using the high resolution model and the simple analytical model of the applicator, the influence of the catheter material properties on the electrode impedance and on the power absorption in the catheter were investigated. Also, the assumption that an electrode behaves like a current source was investigated. The reliable results of these investigations were compared with the results from the current source model, which uses ideal current sources. The catheter properties that were used are listed in table 4.1.

4.3.1   Impedance

The electrode impedance is defined as the impedance between the metallic electrode and zero potential. In the current source model it is assumed that the catheter wall acts as a perfect dielectric and does not contribute to the real component of the electrode impedance, which also means that all heat generation takes place in the tissue. In practice all catheter materials are lossy to some degree. The loss angle of a material is defined by

$$\tan \delta = \sigma/\omega\epsilon. \tag{4.7}$$

This loss angle varies between about 0.03 for Nylon and $0.5 \cdot 10^{-3}$ for Teflon. By varying the value of $\tan \delta$ between the given limits and calculating the wall impedance we can investigate the sensitivity of the electrode impedance for variations of the wall properties. For this purpose, we have assumed that the relative permittivity of the wall was constant and equal to 3 and that $\tan \delta \in [0.0, 0.1]$ so

that the conductivity $\sigma = \omega\epsilon \tan\delta \in [0.0, 0.45 \cdot 10^{-3}]\,\mathrm{S\,m^{-1}}$. The tissue boundary was chosen to simulate a fixed zero potential boundary condition at 1 cm from the catheter centre, which is a reasonable distance between the catheter and a virtual ground plane in common implant geometries.

Theoretically we expect the real part of the wall impedance to be proportional with $\tan\delta$, because

$$Z \propto \frac{1}{\kappa} = \frac{1}{\sigma + i\omega\epsilon} = \frac{1}{\omega\epsilon \tan\delta + i\omega\epsilon} \propto \frac{\tan\delta - i}{\tan^2\delta + 1} \qquad (4.8)$$

and, in the domain of interest, $\tan^2\delta \ll 1$.

The MECS applicator is designed to deposit all its power directly in the tissue; the power density (SAR) in the catheter wall should be as low as possible. Undesired power dissipation in the catheter wall adds a conductive component to the temperature gradient in the tissue, lowering the effective penetration depth of the produced heat and thus lowering the catheter spacings clinically allowed (Emami et al., 1990). Unfortunately, practical catheters have lossy wall materials (table 4.1). The ratio between the real part of the wall impedance and the real part of the tissue impedance was investigated. It should be equal to the ratio of the integrated power depositions in the catheter wall and in the tissue, for $P = I^2 R = I^2(R_{\mathrm{wall}} + R_{\mathrm{tissue}})$.

By definition, in an ideal current source situation the electrode current is insensitive to variations in tissue conductivity. To test the current source approximation the electrode current was calculated as a function of tissue conductivity for an applicator in a homogeneous medium. The capacitive component of the tissue cylinder is very small compared to the capacitive component of the catheter wall. Thus, the relative permittivity of the tissue was kept fixed at 80.

4.3.2 Absorbed power distribution

The high resolution model enables us to compute the complete SAR distribution in the volume, including the dissipation in the catheter wall.

Two model geometries were investigated: a two dimensional high resolution plane perpendicular to the long axis of the applicator, with a resolution of 0.15 mm (infinitely long applicator), and a three dimensional volume with a resolution of 0.3 mm. The tissue boundary was again chosen to simulate a fixed zero potential boundary condition at 1 cm from the catheter centre. The two dimensional

geometry is used to compare the distribution with the analytical results and with the current source model. The three dimensional geometry with homogeneous muscle tissue, gives the SAR distribution along the electrode.

We have also used the high resolution electrical model on a volume which models a tissue volume with a step in conductivity along an infinitely long catheter. In this way the influence of tissue conductivity on the current density and the SAR distribution and the behaviour of the current density at the boundary between the contrasting tissue media was investigated in three dimensions. An interface between muscle and fatty tissue, with properties as given in table 4.1, was modelled at a resolution of 0.3 mm. The tissue boundary was again chosen to simulate a fixed zero potential boundary condition at 1 cm from the catheter centre. The top and bottom boundaries were isolating. We also modelled this situation with the current source model at the same 0.3 mm resolution.

4.4   Results and discussion

4.4.1   Impedance

A theoretical estimate of the fraction of the total delivered power dissipated in the catheter wall as a function of the loss angle of the catheter material is shown in figure 4.2. This result was calculated from the ratio of the real parts of the catheter wall impedance and the electrode impedance respectively. The electrode impedance is the sum of the catheter wall impedance and the tissue impedance. The variation of the real part of the electrode impedance with the loss angle of the catheter wall is depicted in figure 4.3.

The electrode current as a function of tissue conductivity for an electrode in a polyethylene catheter in a homogeneous medium is shown in figure 4.4. The relative permittivity of the tissue is 80 and the conductivity varies between 0.1 and $1.0\,\mathrm{S\,m^{-1}}$. This figure shows that the influence of the tissue conductivity on the electrode current is small for this range of conductivities.

The capacitance of the catheter wall is much smaller than the tissue capacitance. Thus, the capacitive part of the electrode impedance is dominated by the capacitance of the catheter. The resistive part of the electrode impedance is dominated by the resistance of the tissue cylinder because the resistance of the catheter wall is much smaller than the tissue resistance. Finally, the imaginary part of the electrode impedance is much larger than the real part, so the magnitude of this impedance
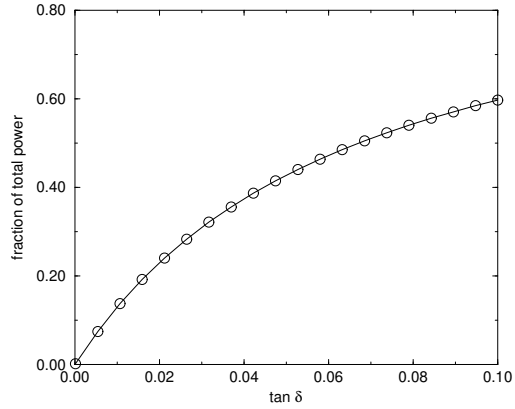
Figure 4.2: Predicted fraction of total delivered electrode power dissipated in catheter wall as a function of the loss angle of the catheter material.
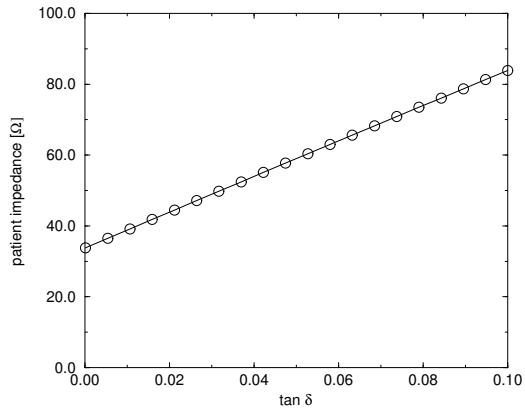

Figure 4.3: Predicted real part of the electrode impedance as a function of the loss angle of the catheter wall material. The offset in this graph is caused by the real part of the tissue impedance.
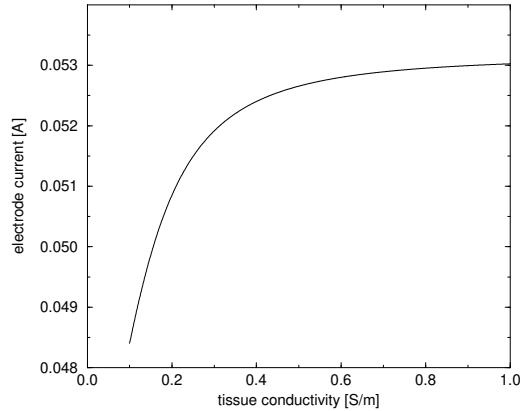
Figure 4.4: Electrode current as a function of tissue conductivity for an electrode in a homogeneous medium. The electrode is inserted in a polyethylene catheter and is held at a potential of 100 V.

is not much influenced by the tissue conductivity, validating the current source approximation. This is summarised in table 4.2.

4.4.2 Absorbed power distribution

Figure 4.5 gives the absorbed power distribution for a polyethylene and a Nylon catheter calculated with the high resolution model and with the current source model. The absorbed power density is sampled along a line passing through and perpendicular to the long axis of the applicator. For all three simulations the injected power is $1\,\mathrm{W\ cm^{-1}}$. The electrode in the polyethylene catheter is therefore fixed at 323 V and the electrode in the nylon catheter is fixed at 142 V. The current injection in the current source simulation is 0.187 A. As can be seen from figure 4.5 and figure 4.2, Nylon has a much higher power absorption in the catheter wall than polyethylene, caused by the higher loss angle of nylon. The SAR profiles for polyethylene and from the current source model should coincide because the wall impedance of a polyethylene catheter can be neglected compared to the tissue impedance and because the current source model assumes that the material of the catheter wall is loss-less. Figure 4.5 shows that this is indeed the case. The two small negative spikes in the profile calculated by the current source model are

Table 4.2: Calculated impedances of several cylindrical regions in the applicator model. Listed are the resistance (the real part of the impedance), the capacitance and the imaginary part of the impedance.

	R $[\Omega\,\mathrm{cm}^{-1}]$	C $[\mathrm{pF}\,\mathrm{cm}^{-1}]$	Im(Z) $[\Omega\,\mathrm{cm}^{-1}]$
polyethylene catheter	0.75	3.12	−1881
fat tissue	178	218	−27
muscle tissue	57	408	−14
polyethylene catheter and fat tissue	179	3.08	−1908
polyethylene catheter and muscle tissue	58	3.10	−1896

caused by the SAR correction as described in De Bree et al. (1996b). The calculated ratio between absorbed power in the catheter wall and the total absorbed power is 34 % for Nylon and 1.2 % for polyethylene. This matches with the analytical results given in figure 4.2.

As a check of the correctness of the results of the high resolution model and the current source model the electrode impedances calculated from the numerical models and equation (4.5) are compared. The results are summarised in table 4.3. The electrode impedance found in the current source case is the impedance as seen by the lumped applicator and consists only of the tissue component. The impedances found by the numerical models are in good agreement with the analytically calculated impedances.

Table 4.3: Comparison of the electrode impedances found by the high resolution (upper two) and the current source model calculations and using the analytical approach.

	numerical		analytical	
	R	C	R	C
setup	$[\Omega]$	[pF]	$[\Omega]$	[pF]
polyethylene	58.8	3.35	57.9	3.10
Nylon	80.9	6.66	85.4	6.15
current source	57.2	406	57.2	408

Figure 4.6 shows the SAR distribution around a 2 cm long electrode in a polyethylene catheter; because of symmetry only one half of the electrode is shown. The
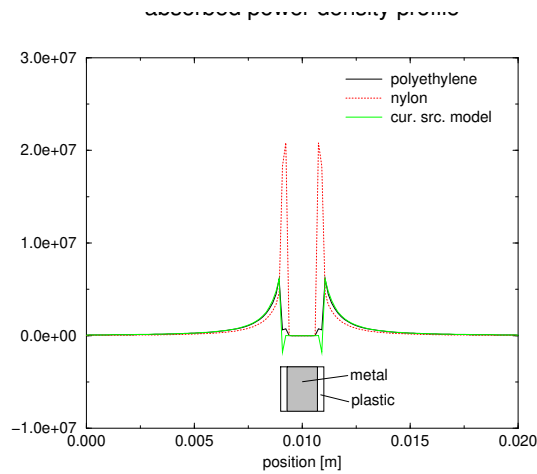
Figure 4.5: SAR distribution calculated with the high resolution model in catheter and tissue for both a nylon and a polyethylene catheter. Also the *SAR* distribution calculated with the current source model has been given.

SAR is highly localised around the catheter as shown by Hand et al. (1991) and in figure 4.5. The tip of the electrode does not produce a singularity because of the reduced capacitive coupling due to the extension of the catheter.

Figure 4.7 shows the iso-contours of the current density and the *SAR* distribution in a cross-section through a MECS applicator in the inhomogeneous fat-muscle medium. In this high resolution computation the electrode is kept at 198 V, which results in an average injected power of $1\,\mathrm{W\,cm^{-1}}$. The current that flows outward through the catheter wall is in the fatty tissue slightly less (1.2 %) than in the muscle tissue. This is in accordance with the currents calculated by equation (4.5) which shows a difference of 1.1 %. Figure 4.8 represents the result calculated with the current source model. The current injection is $135\,\mathrm{mA\,cm^{-1}}$, which results in an injected power of $1\,\mathrm{W\,cm^{-1}}$. The current density and the *SAR* calculated with both models are in accordance with each other.
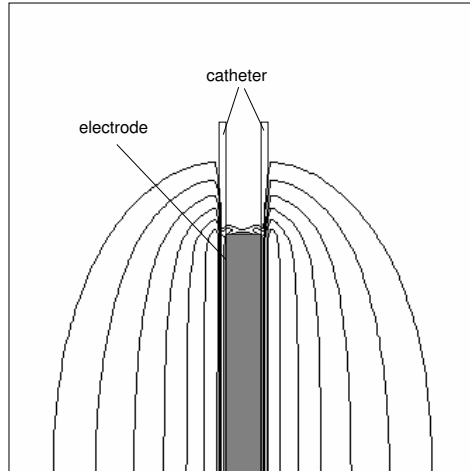
Figure 4.6: Slice through the centre of the electrode showing the iso-SAR contours. The electrode is inserted in a polyethylene catheter. With each contour the SAR level decreases by a factor two when going away from the electrode.
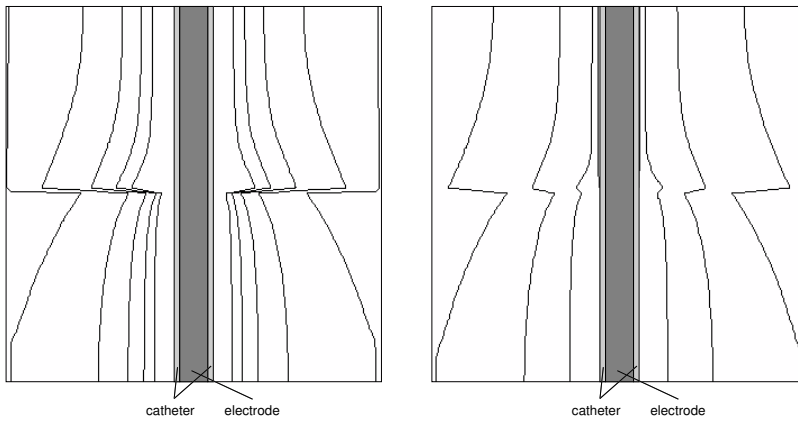

Figure 4.7: Slice through the centre of the electrode showing the iso-contours of the magnitude of the (complex) current density in the first figure (contours at $200, 400, 600, 800$ and $1000\,\mathrm{A\,m^{-2}}$) and of the absorbed power density in the second figure (contours at $10^5, 4 \cdot 10^5$ and $16 \cdot 10^5\ \mathrm{W/m^3}$). The electrode is inserted in a polyethylene catheter. The upper half of the tissue is muscle and the lower half is fat. The calculation is done with the high resolution model.
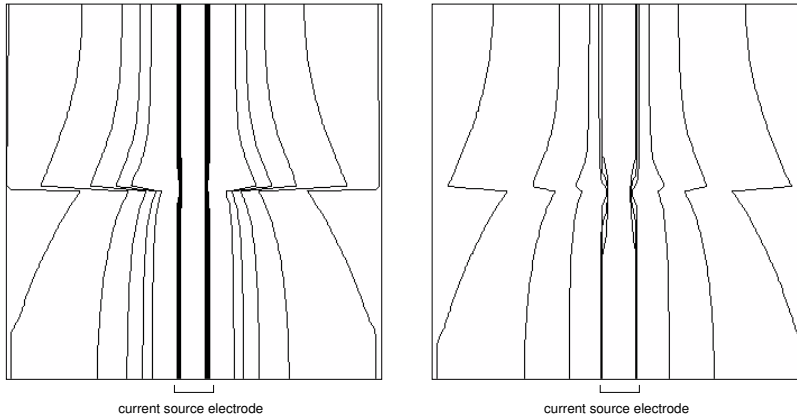
current source electrode   current source electrode

Figure 4.8: Slice through the centre of the catheter showing the iso-contours of the magnitude of the (complex) current density in the first figure (contours at $200, 400, 600, 800$ and $1000\,\mathrm{A\,m^{-2}}$) and of the absorbed power density in the second figure (contours at 10^5, $4\cdot 10^5$ and $16\cdot 10^5\,\mathrm{W\,m^{-3}}$). The upper half of the tissue is muscle and the lower half is fat. The calculation is done with the current source model.

4.5   Conclusions

The high resolution computations and the analytical results confirm the validity of the ideal current source approximation for interstitial hyperthermia treatment planning. The errors introduced by this approximation are small because the electrode impedance is dominated by the small capacity of the catheter wall. This makes the current injection insensitive to anatomy and geometry, allowing eg. non-parallel complex implants (Deurloo et al., 1991). In the current source model used in our interstitial hyperthermia treatment planning system the applicator is considered an ideal loss-less current source. This is acceptable for low-loss catheter material and has great advantages from a modelling point of view: the model is flexible and fast (De Bree et al., 1995).

Lossy catheter materials cause significant additional heat production in the catheter wall. Polyethylene and Teflon can be considered low-loss and are ideal materials for MECS IHT. The use of Nylon should be discouraged; Nylon shows a high power absorption inside the catheter wall. This adds a conductive heating component to the temperature gradient in the tissue which induces a more heterogeneous temperature distribution (Kaatee et al., 1995) for a given catheter spacing.

The heat production in the catheter wall should be incorporated in the current source model, which is used to produce a SAR distribution for use in the thermal model. This can be implemented by adding a SAR to the electrode voxels, which will depend on the exact properties of the catheter wall material and on the injected current.

As was shown by Hand et al. (1991), the SAR is highly localised near the catheter. In contrast with conductive coupling IHT, the tip of the electrode does not go with a steep increase of the SAR because of the reduced capacitive coupling due to the extension of the catheter beyond the electrode.

The calculations concerning a fat-muscle interface show that, as expected with current source behaviour, the SAR around an electrode is higher in fatty tissue than in muscle tissue. Chapter 6 illustrates that it is essential to segment the electrodes to introduce 3D SAR control in such a case.

Chapter 5

Thermal properties of capacitively coupled electrodes in interstitial hyperthermia

5.1 Introduction

The multi-electrode current-source interstitial hyperthermia (MECS-IHT) technique was designed for the application of spatially controlled hyperthermia (Lagendijk et al., 1995; Kaatee et al., 1997b,a). It employs individually controlled electrodes operating at 27 MHz radio frequency, inserted into plastic brachytherapy catheters. The principle of current source electrodes has been described by Marchal et al. (1989), Visser et al. (1989) and Deurloo et al. (1991). Chapter 4 gives an account of the electrical properties of current source electrodes.

Utilization of the 3D control provided by the multi-electrode system requires extensive 3D thermometry. To this end seven sensor thermocouple probes are integrated into the applicator. Temperature control is straightforward for ideal electrodes inserted in ideal, loss-less catheters (Crezee et al., 1997). This chapter focuses on the realistic physical properties of applicator and catheter. First the influence of the loss angle of the catheter material on the temperature measured in the core of the applicator is investigated. The results allow the selection of suitable catheter properties and the determination of the magnitude of possible temperature differences between the central thermocouple and the tissue just outside the applicator, opening up the possibility of almost real-time feedback control during treatment. Second, the decay of this offset to the measured temperatures during power-off is investigated. The final investigation concerns the measurement of gradients in the tissue temperature along the catheter, using thermocouples in the central core of the applicator.

Table 5.1: Sizes of important structures in the MECS applicator.
OD=outer diameter, ID=inner diameter.

structure	size	unit	structure	size	unit
OD patient catheter	2.0	mm	OD electrode carrier	1.3	mm
ID patient catheter	1.6	mm	ID electrode carrier	0.7	mm
gap	0.1	mm	gap	0.1	mm
OD electrodes	1.4	mm	OD thermocouple plastic	0.5	mm
thickness electrode lining	12	μm	OD thermocouple string	0.15	mm
thickness electrodes	20	μm	thickness thermocouple wires	50	μm
thickness copper wire	50	μm			

5.1.1 Construction of the applicator

The MECS-IHT system employs applicators inserted in plastic catheters implanted in the treatment volume. Each applicator carries multiple independent electrodes. The catheter, into which the applicator is inserted, serves as a dielectric layer between the metallic electrodes and the tissue volume. The capacitance of the catheter wall is about 5–10 pF/cm. At page 44, in figure 4.1, a schematic drawing of the applicator is shown.

The core of the applicator consists of a string of constantan-manganin thermocouples in a thin plastic tube, used to acquire temperature information for treatment control (Ella CS). The next layer is the plastic tube which serves as carrier of the electrodes. The electrodes are made of silver-paint and are connected to the circuit matching the applicator to the transmission lines by a thin copper wire. The power deposition is controlled by varying the duty-cycle of the RF-signal applied to the electrodes. The electrode carrier is covered by an extremely thin heat-shrunk plastic sleeve which greatly improves its physical integrity. Space in between some structures is filled with air. The radial dimensions of the inner parts of the applicator are summarised in table 5.1.

During treatment, temperatures measured within the applicators are used to adjust the duty cycle for each individual electrode. To this end the power is briefly interrupted to eliminate electronic disturbance of the thermocouple signal. The thermometry system yields reliable data within one second after power off (De Leeuw et al., 1993). It is important to know details of the temperature distribution within the applicator, to be able to correctly control the electrodes. For instance, if the dielectric material of the wall is low-loss instead of loss-less, heat will be generated in this wall. This self-heating affects the temperature distribution in

Table 5.2: The material properties used in the calculations in this chapter.

material	density	thermal conductivity	heat capacity	electrical conductivity	ϵ_r	$\tan \delta$
	$\mathrm{kg\,m^{-3}}$	$\mathrm{W\,m^{-1}\,K^{-1}}$	$\mathrm{J\,kg^{-1}\,K^{-1}}$	$\mathrm{S\,m^{-1}}$		
air	1.16	$26 \cdot 10^{-3}$	1000	$1 \cdot 10^{-18}$	1	n.a.
tissue	1000	0.6	4000	0.6	80	n.a.
constantan	8900	40	386	204	1	n.a.
copper	8900	400	386	5880	1	n.a.
manganin	8400	20	386	204	1	n.a.
Nylon (PA11)	1000	0.247	2100	$1.8 \cdot 10^{-4}$	4	$3 \cdot 10^{-2}$
polyethylene	920	0.335	2300	$1.2 \cdot 10^{-6}$	2	$4 \cdot 10^{-4}$
Teflon	1400	0.252	1000	$1.5 \cdot 10^{-6}$	2	$5 \cdot 10^{-4}$

the applicator, but one may adjust the control temperatures so that the temperatures in the surrounding tissue remain close to their clinical goal temperature. We are also interested in the thermal decay after power off, and especially in the relation between the temporal behaviour inside and outside, and whether the internal thermal decay data provide sufficient information to characterise the self heating component. Furthermore, the dynamics of the temperature distribution also give information on the thermal properties of the applicator and its surroundings. The temperature decay measured by the thermocouple is expected to have two main components; a fast one due to cooling of the 'self-heated' catheter wall and a slower one related to the cooling of the tissue. Thus, when the power-off interval is short, the measured temperature includes a self-heating component, and to obtain the true tissue temperature one must either extend the power off interval, or estimate the self heating component and subtract it from the measured temperature (De Leeuw et al., 1993). Any control method exploiting a relation between loss angle, internal and external temperature must be well-tested as errors may lead to hot or cold spots in the tissue. Methods for using the decay data to characterise tissue and blood flow properties (Waterman et al., 1987; Lagendijk et al., 1988; Roemer, 1990b) are not the subject of this study.

5.2   Methods

The transient and stationary temperature distribution inside and outside the applicator are influenced by the choice of a catheter wall material and the composition

of the applicator. Our investigation focuses on the influence of the SAR deposition in the catheter wall and of layers of air in the applicator structure on the temperature measurements. Both analytical models for simple 1D and 2D situations and a high resolution numerical 2D model for calculation of the transient distributions were used. Rotational symmetry is assumed. The simulated tissue is muscle without perfusion. The results of the model calculations are compared with experimental data obtained with our hyperthermia system in phantom material. The applicator used contains two 20 mm long electrodes operating at opposite phase. The catheter dimensions and properties are listed in table 5.1 and 5.2.

5.2.1 SAR in co-axial structures

In chapter 4, both a numerical and a simple analytical model are used for modelling the electrical properties of the applicator. In this chapter, only the analytical approach is used to find the radial SAR distribution. Briefly, the potential distribution $V(\mathbf{r})$ in the modelled applicator is governed by the Poisson equation (Sowinski and van den Berg, 1990; De Bree et al., 1996b)

$$-\boldsymbol{\nabla}\cdot\kappa\boldsymbol{\nabla}V = 0 \tag{5.1}$$

where $\kappa = (\sigma + i\omega\epsilon)$ is the admittance, σ is the conductivity in $\mathrm{S\,m^{-1}}$, ω is the angular frequency of the power signal, ϵ is the permittivity and V is the (complex) potential in V. Equation (5.1) follows from a quasi-static approximation of the Maxwell equations which is applicable in this case because the dimensions of the computational volume are small compared to the wavelength in tissue of the 27.12 MHz signal, about 1 m in muscle (Sowinski and van den Berg, 1990; De Bree et al., 1996b). Given the potential distribution and the properties of the material, the dissipated power density P in the material is calculated as follows:

$$P = \frac{1}{2}\,\sigma\,|\boldsymbol{\nabla}V|^2\,. \tag{5.2}$$

This relates to the SAR by $SAR = P/\rho$, with ρ the mass density of the medium.

The analytical approach as given in chapter 4 involves describing the system of nested coaxial layers considered as an infinitely long applicator in terms of lumped properties (resistance and capacity), which is justified because of the small radial size of the structures with respect to the wavelength.

Ideally the catheter wall acts as a perfect capacitor and does not contribute to the real component of Z; all heat generation is localised in the tissue. In practice all

catheter materials are lossy to some degree. The loss angle of a material is defined by $\tan\delta = \sigma/\omega\epsilon$ and varies between almost nil, $0.4\cdot10^{-3}$ for polyethylene (PE) and Teflon (PTFE), and 0.03 for Nylon (polyamide, PA) (table 5.2). The sensitivity of the electrode impedance for variations of the wall properties was investigated by varying the value of $\tan\delta$ between the given limits and calculating the wall impedance. The real part of the wall impedance was found to be proportional to $\tan\delta$.

In the following sections stationary and transient temperature distributions are computed for two different catheter materials, PE and PA, using the radial SAR distributions computed in Van der Koijk et al. (1997b) (see chapter 4).

5.2.2   The temperature distribution in coaxial structures

The stationary and transient temperature distribution near an electrode depends on the physical properties of the catheter wall and the surrounding tissue. In the following sections we concentrate on the effect of catheter properties and the contact between the various nested structures inside the applicator on the stationary radial temperature distribution, the thermal decay after power off, and the stationary gradient in the axial direction.

The radial steady state temperature distribution

Consider the radial temperature distribution during steady state heating. The temperature at a thermocouple inside the MECS-applicator is influenced by the thermal and electrical properties and the geometry of the catheter wall. The result may be a temperature difference between applicator core and tissue. Using the SAR distributions calculated in Van der Koijk et al. (1997b), the steady state temperature distribution in the applicator wall can be computed as follows (Carslaw and Jaeger, 1959): Assuming an infinitely long hollow cylinder which has a given thermal conductivity k and a given (uniform) heat production P, the temperature in this cylinder is governed by

$$\frac{1}{r}\frac{d}{dr}\left(r\frac{dT(r)}{dr}\right) + \frac{P}{k} = 0. \tag{5.3}$$

The general solution of this equation is

$$T(r) = A + B\ln r - \frac{Pr^2}{4k}. \tag{5.4}$$

In case of a solid cylinder, the $\ln r$ term is inadmissible and A is the temperature at the axis of the cylinder. The heat flow rate density ϕ in the cylinder is given by

$$\phi = k\frac{dT(r)}{dr} = k\left(\frac{B}{r} - \frac{Pr}{2k}\right).$$ (5.5)

Now, the equations (5.3), (5.4) and (5.5) can be used to find the steady state temperature distribution in a geometry consisting of a number of concentric cylinders, by first finding the B terms for all cylinders using continuity of heat flow at the interfaces between the cylinders and then, using the continuity of temperature, finding the A terms.

We calculated the stationary temperature distribution in and around the MECS-applicator using the 1D technique described above, using the thermal properties listed in table 5.2. The applicator is located in the lumen of a catheter (dimensions given in table 5.1) inserted in muscle tissue with a cylindrical boundary at 10 mm, similar to the geometry used in Van der Koijk et al. (1997b). We assume a rotationally symmetric temperature distribution and negligible temperature gradients along the catheter. The catheter was modelled with a radial resolution of less than 50 μm. The term P was considered constant in each 50 μm thick annulus and is given by the analytical model of the radial electrical field in the catheter described in Van der Koijk et al. (1997b). The effect of variation of the loss angle of the catheter material was investigated; the range $0 < \tan\delta < 0.1$ includes PE and PA. For comparison we also analysed the temperature distribution associated with purely conductive heating, by making the electrical tissue conductivity very large and thus setting the tissue SAR to zero. Self heating effects in-between the electrode and the thermocouple are considered absent because both the thermocouple and electrode carrier are made of loss-less Teflon and the SAR in-between the electrode and the thermocouple is negligible.

The temperature decay after switching off the electrode

Normally, no extensive extra invasive thermometry is present during treatment; the detailed 3D tissue temperature distribution can only be determined using the integrated thermometry. This is achieved by regularly interrupting the power for a few seconds and analysing the resulting temperature decay. Different time dependent behaviour may be expected for PE and Nylon catheters.

We simulated this method with a numerical model and compared the result with experiments in a muscle equivalent phantom. The high-resolution numerical thermal model used (Kotte et al., 1996b) is based on a finite difference algorithm, and

is used in this case to solve the heat transfer equation

$$\rho c \, \frac{\partial T}{\partial t} = \boldsymbol{\nabla} \cdot (k \boldsymbol{\nabla} T) + P, \tag{5.6}$$

where ρ is the density in $\mathrm{kg\,m^{-3}}$, c the tissue specific heat in $\mathrm{J\,kg^{-1}\,K^{-1}}$, k the thermal conductivity in $\mathrm{W\,m^{-1}\,K^{-1}}$ and P the power absorption rate in $\mathrm{W\,m^{-3}}$. Equation (5.6) is used to simulate the temperature decay after switching off the electrode power at $t = 0$ in the geometry described in section 5.1.1. Again we assume negligible temperature gradients along the catheter. For $t < 0$ the temperature distribution is the steady state profile computed in section 5.2.2. This profile is interpolated on a flat, square grid of 200×200 voxels which has world dimensions of 10×10 mm; this leads to a nearest neighbor voxel centre distance of $50\,\mu\mathrm{m}$. For $t > 0$ we apply equation (5.6) with $P = 0$. Discretisation effects were acceptable; calculations at double resolution yielded results identical within a few percent, at the cost of an unacceptably low computational speed. Due to symmetry the computation can be limited to only one quadrant, with the centre of the applicator positioned in the top-left corner of the grid. The outer tissue boundary at 10 mm is at room temperature. The fourier time of the setup was $27\,\mu\mathrm{s}$ and a three time level scheme with a time step of $3.3\,\mathrm{ms}$ was used.

Experimental data were acquired in a setup consisting of either PE or PA catheters placed in a container ($10 \times 10 \times 10$ cm) filled with a muscle equivalent gel containing 0.3 %NaCl and 2 % hydroxy propyl methyl cellulose. The applicator contains two 20 mm long electrodes operated at opposite phase, containing a seven sensor thermocouple probe for power control. The tip of an additional seven sensor thermocouple probe is placed in the gel against the catheter at the location of one of the electrodes. Constant power is given to the electrodes. When stationary temperatures are reached the power is switched off and the thermal decay inside and outside the applicator is monitored.

The steady state temperature gradient along the catheter

The steady state temperature measured by the embedded thermocouple $T(x)$ can be viewed as a weighted average of the temperature $T_{\mathrm{wall}}(x)$ just outside the catheter wall. The thermal conduction in the axial direction x of the thermocouple string is much better than over the plastic catheter wall. This causes distortion of the axial temperature profile. If we assume that

▷   the longitudinal heat conductivity of the applicator wall is negligible in comparison with the longitudinal heat conductivity of the thermocouple;

▷   there is no radial temperature gradient in the thermocouple core;
▷   the thermocouple can be considered to be homogeneous;
▷   there is no self-heating of the thermocouple;
▷   the longitudinal conductivity of the whole applicator is very low compared
    to that of its surroundings,

then this situation is equivalent to the problem of heat conduction along a thin rod
connected to its surrounding by a finite thermal conductance. The temperature
of the thermocouple $T(x)$ as a function of the tissue temperature just outside the
catheter $T_{wall}(x)$ is governed by the differential equation

$$\frac{d^2 T(x)}{dx^2} - \frac{2Hr_{out}}{k_{tc}r_{tc}{}^2}\left(T(x) - T_{wall}(x)\right) = 0.$$

We apply this equation in a simple test situation; a temperature step at $x = x_0$
with $T_{wall} = T_{low}$ for $x < x_0$ and $T_{wall} = T_{high}$ for $x \geq x_0$. The solution is

$$T(x) = \begin{cases} T_{high} - \frac{1}{2}(T_{high} - T_{low})\exp^{-(x-x_0)\cdot\alpha} & \text{if } x \geq x_0 \\ T_{low} + \frac{1}{2}(T_{high} - T_{low})\exp^{+(x-x_0)\cdot\alpha} & \text{if } x < x_0 \end{cases} \tag{5.7}$$

The axial distortion is inversely proportional to $\alpha = \sqrt{2Hr_{out}/k_{tc}r_{tc}{}^2}$ (Carslaw
and Jaeger (1959), page 133); with the constant H the surface conductance of a
uniform rod: $H = G/2\pi r_{out}$, with G the radial conductance per unit length of the
concentric structures in the catheter between the thermocouple and the catheter
wall given by (Carslaw and Jaeger (1959), page 190, equation 12)

$$G = 2\pi \left(\sum_{l=1}^{n} \frac{\ln(r_{l+1}/r_l)}{k_l}\right)^{-1}. \tag{5.8}$$

In this equation, k_l is the heat conductivity, r_l the inner and r_{l+1} the outer
radius of cylinder l. Note that the use of copper instead of manganin reduces α
by a factor $\sqrt{20}$. Dickinson (1985) compared copper and manganin thermocouple
probes with step function experiments; manganin indeed proved far more reliable.

This model is tested by measuring the steady state axial temperature distribution
inside an electrode placed in a PE catheter mounted in a water bath (measuring
$20 \times 20 \times 40$ cm). The temperature profile along the catheter is a step function:
the bath is divided in two sections, the water temperature in one section is room
temperature, the temperature in the other half is kept six or seven degrees higher.
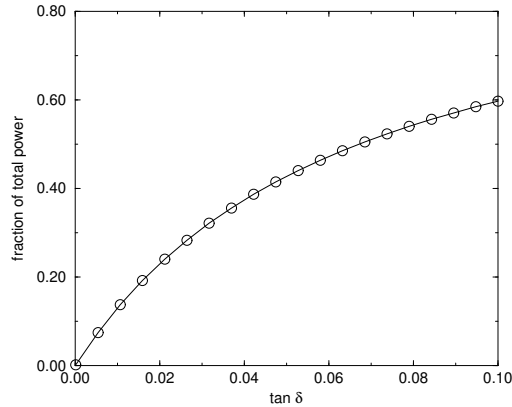The dividing wall at $x = x_0$ is about 0.1 mm thick and the water at both sides is

Figure 5.1: Fraction of total delivered electrode power dissipated in catheter wall as a function of the loss angle of the catheter material. The geometry is described in section 5.1.1.

well stirred. The step response was measured by moving the applicator through the catheter in 0.5 mm steps over a distance of 6 cm. Each thermocouple sensor will cross the division, enabling us to study smear as a function of the number of thermocouple wires. The effective diameter of the sensor varies between 0.035 mm (for two wires) and 0.071 mm (for eight wires).

5.3   Results

5.3.1   Electrode impedance and partition of power between catheter wall and tissue as a function of the loss angle

The real part of the electrode impedance and the fraction of power dissipated in the catheter wall as a function of the loss angle of the catheter material (figure 5.1) were computed in Van der Koijk et al. (1997b). Note that in lossy materials a significant part of the power deposition takes place in the catheter wall, e.g. 34 % for 'low loss' Nylon.
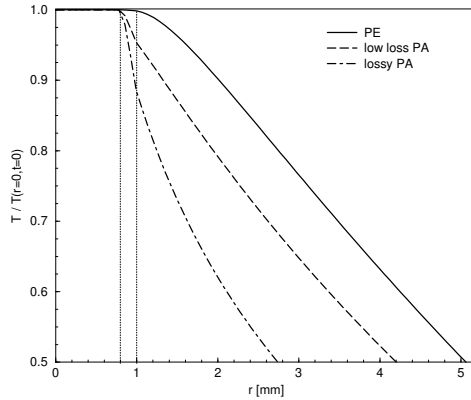
Figure 5.2: Normalised radial temperature profiles for three different catheter types for steady state with power on. The geometry is described in section 5.1.1. The outer tissue boundary is at $r = 10$ mm, the catheter wall boundaries are indicated by the two vertical lines at $r = 0.8$ mm and $r = 1.0$ mm.

5.3.2 The temperature distribution in coaxial structures

Temperature difference between applicator core and tissue just outside the catheter.

The radial temperature distribution was computed for three catheter materials (figure 5.2). There is no temperature gradient for $r < 0.8$ mm as there is no power deposition inside the inner catheter wall. Self heating causes a gradient in the wall ($0.8 < r < 1.0$ mm) and a sharp reduction of the radial penetration depth of the probe. In PE the 50 % isotherm is found at $r = 4.1$ mm from the catheter wall, versus $r = 3.2$ mm for low-loss Nylon, and $r = 1.7$ mm if all power is dissipated in the catheter wall. Regarding the reliability of the thermometry: For low-loss Nylon the wall temperature is 6 % lower than the measured applicator core temperature, versus an 11 % difference for conductive heating. This can also be observed in figure 5.3, where the temperature inside and outside the catheter is plotted versus $\tan \delta$; only in a loss-less material the temperature inside and outside are equal. The temperature at 1 mm from the catheter decreases more significantly for increasing $\tan \delta$, due to the reduction in penetration depth of the SAR deposition illustrated in figure 5.2.
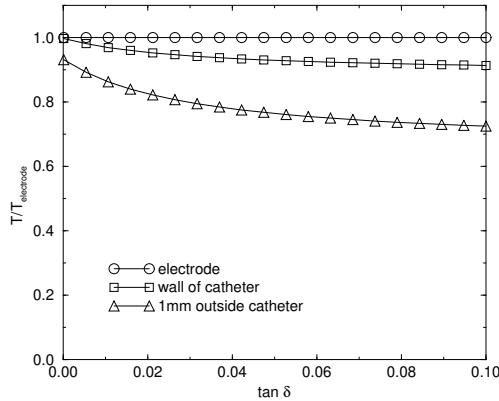
Figure 5.3: Relative temperature difference between the thermocouple in a MECS applicator, at the outer catheter wall and at a distance of 1 mm outside the catheter wall as a function of the loss angle of the catheter material in steady state.

The temperature drop after switching off the electrode power

Figure 5.4 shows the evolution of the radial temperature gradient after power off for three different catheter types. Within a few seconds steep gradients occur at $r = 0.3$ mm and at $r = 0.75$ mm, coinciding with the regions filled with air. Their high thermal resistance delays cooling of the interior. After about 30 seconds this effect has disappeared. For three radii, $r = 0$ mm (thermocouple core), $r = 1$ mm (wall-tissue interface) and $r = 2$ mm (1 mm outside the applicator), the temperature is plotted versus the time in figure 5.5, to compare the decay at the thermocouple and in the tissue outside the catheter. When loss-less catheter materials are used the thermocouple temperature is equal to the temperature of the surrounding tissue at $t = 0$ and remains stable for another two seconds. Thus, two seconds after power-off, measurement of the thermocouple temperature still yields a reliable indication of the tissue temperature at $t = 0$. This is due to the absence of a temperature gradient within the applicator during stationary heating, after power off some time is needed before the thermal decay reaches the centre of the probe. The air layers delay decay even further. For comparison the transient temperature distribution was also computed for an electrode in a gap-less situation in a loss-less catheter,
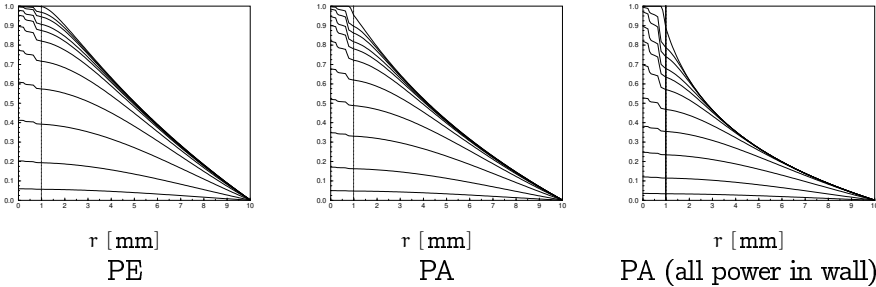
Figure 5.4: Normalised radial temperature profiles for three different catheter types $0, 1, 2, 4, 6, 10, 20, 40, 80, 160, 300$ seconds after the power is switched off (From top to bottom). The vertical line at $r = 1$ mm indicates the outer catheter wall.

with air substituted by PE. The tissue temperature curves are almost identical, but in the case of a solid applicator wall the decay of the thermocouple signal is 2–3 seconds faster, much of the plateau phase disappears (figure 5.6). The extra thermal resistance of the air layers also enhances the magnitude of the transient differences between the thermocouple temperature and the wall temperature.

During the next 60 seconds the difference between the temperature decay inside and outside is at most 5 to 10 % of the maximum temperature rise when using loss-less catheter materials like PE and PTFE (figure 5.5). For high-loss materials there is initially a significant difference between the temperature inside and outside, only after about 20 seconds the internal thermometry becomes reliable. Apparently the power dissipation in the catheter wall gives rise to an extra component in the thermal decay, faster than the components associated with the tissue heating. However, this fast component is also noticeable in the tissue temperature at $r = 1$ mm. This represents very local tissue heating as this component is absent at $r = 2$ mm, and is also not seen in the experimental results.

The results from the phantom measurements are shown in figure 5.7. The results agree qualitatively with the simulated behaviour between $r = 1$ mm and $r = 2$ mm (figure 5.5). As $\tan \delta$ rises the initial difference between the thermocouple and tissue temperature becomes larger. Normalised initial tissue temperatures of 0.86 and 0.63 were obtained for PE and PA, respectively, which is lower than calculated, but showing the same downward trend. No plateau phase is present in
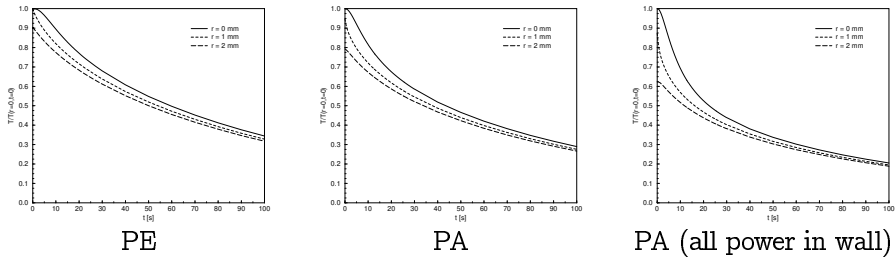
Figure 5.5: Computed temperature drops after switching off the power to an electrode. Catheter material is PE, PA or high loss PA. In each figure, the temperature drops are shown as a function of time for three radial positions. From top to bottom: $r = 0$ mm, the applicator core; $r = 1$ mm, the catheter wall; and $r = 2$ mm, in the tissue, 1 mm from the catheter wall.
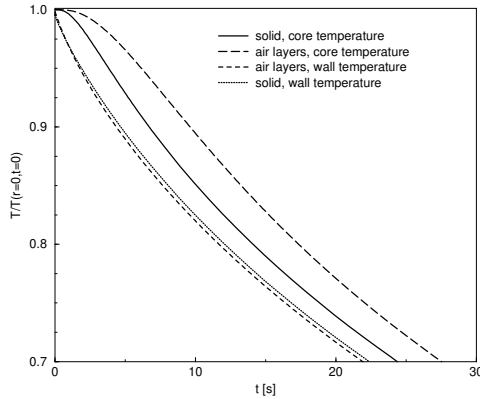

Figure 5.6: Computed temperature drops after switching off power for a solid PE applicator and for an applicator containing air layers, at $r = 0$ mm and $r = 1$ mm.
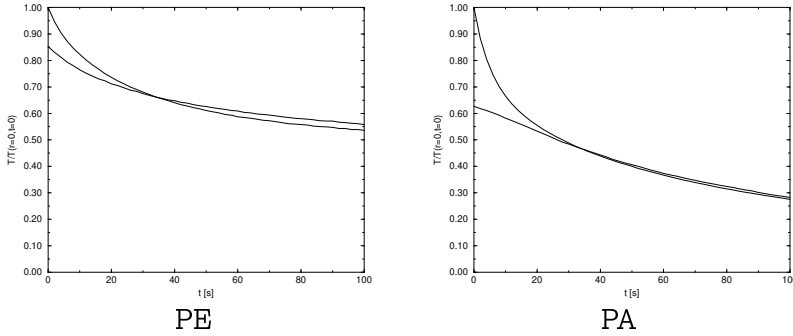
Figure 5.7: Measured temperature drop after switching off the power. Catheter material is PE or PA. Temperatures are shown for two positions: in the central thermocouple and in a thermocouple located less than 1 mm outside the catheter wall.

the thermocouple signal curve measured in PE. Apparently, in practice the air layers dominate the thermal wall resistance less than computed. A likely explanation is the presence of contact points bridging the air layers. Interestingly, in the measurements the central thermocouple temperature drops below the tissue temperature after about 30 s. This may be explained by the limited axial extension of the heated volume; after power off the thermocouple cools rapidly in the axial direction where the thermal conductivity is far better than in the radial direction (section 5.2.2).

The steady state temperature gradient along the catheter.

Temperature data measured by five out of seven sensors of a thermocouple probe crossing the division are shown in figure 5.8. Curves of the form predicted by equation (5.7) are fitted through the data. For example, the relaxation coefficient for 'tc 4' is $\alpha = 585.5$ m^{-1} (equivalent to smear extending 1.7 mm), compared to a predicted $\alpha = 463$ m^{-1} for $r_{tc} = 0.043$ mm (equivalent to three 50 μm wires), using equation (5.8). The α predicted without air gaps is 1843 m^{-1}, equivalent to four times less axial distortion. In figure 5.9 the log of the experimental values for α and the values computed with and without air gaps are shown versus the log of the number of thermocouple wires, yielding a linear relation in the graph.
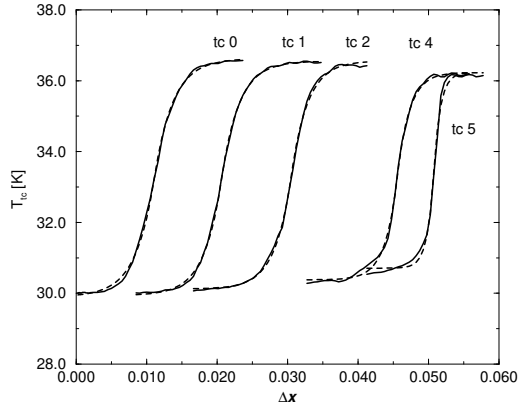
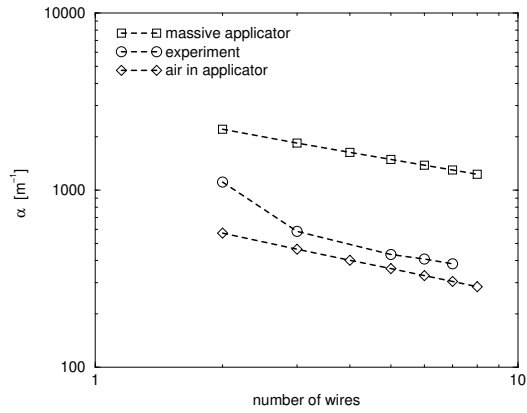*Figure 5.8:* Step response: Measured temperature data and fitted results.

Figure 5.9: Axial smearing coefficient α: experimental data versus model prediction.

Axial distortion increases with the number of wires, but air gaps have a far more significant effect. The experimental curve yields slightly less 'smear' than the simulation of a layered probe. In practice, there will be contact points bridging the air layers, improving radial conductivity. The theoretical model fails for the topmost thermocouple where the leads extend in just one direction, resulting in far less smear than computed.

5.4 Discussion and Conclusions

The MECS applicator is designed to deposit its power only in tissue; not in the catheter wall. However, in practice all catheter materials are lossy to some degree (table 5.2). This affects both the SAR distribution and the reliability of the thermometry.

Regarding the SAR distribution: the steady state tissue temperature distribution of a system with power deposition in both the catheter wall and the tissue can be regarded as a sum of two temperature distributions, one associated with the SAR deposition in the tissue and one with the SAR in the catheter. The latter is similar to conductive heating and has a significantly smaller penetration depth than the former Mechling and Strohbehn (1986); Stauffer et al. (1995); Wonnell et al. (1992). The ratio between the components determines the effective penetration depth. In our geometry the 50 % isotherm ranges between 1.7 mm and 4.1 mm, depending on this ratio. Thus, a consequence of self heating is a reduction of the allowed spacing between the catheters as the system is modified in the direction of conductive heating. Diederich et al. (1996) showed a similar dependency on the degree of selfheating for interstitial ultrasound applicators. These ultrasound applicators have an efficiency of 60–65 %, similar to a MECS applicator in a low-loss Nylon catheter.

PE and PTFE are ideal catheter wall materials: their selfheating is negligible. Low-loss Nylon may also be acceptable; the wall receives 34 % of the total power delivered, yet the radial temperature distribution is only slightly worse than for PE, with the 50 % isotherm at r = 3.2 mm. A higher proportion of power dissipation in the catheter wall is undesirable; the temperature distribution becomes similar to conductive heating.

Regarding thermometry: At steady state the temperature drop over the catheter wall is absent for PE, 6 % for low-loss Nylon, and 11 % for conductive heating. The difference for low-loss Nylon is so small that the thermocouple signal still represents

the temperature of the surrounding tissue reasonably accurately, it is not really relevant to estimate the self heating component. The self heating component is only relevant when high-loss nylon is used, but that material should be avoided because of the poor penetration depth resulting from its use. More interesting is *when* you should measure the temperature. Absence of self heating has the advantage that the thermocouple provides a reliable indication of the temperature of the surrounding tissue up to two seconds after power-off. This allows us time to await disappearance of the electronic disturbance after power off, which takes less than one second.

Axial distortion is present but was found to affect temperatures a few millimetres away at most, which is acceptable in clinical applications where we use 10–20 mm long electrodes (Hand, 1993). Elimination of the air gaps which dominate this effect would further reduce smear, as our results show and as is advised by Samulski et al. (1985). Unfortunately the presence in the catheter of oil or other media improving thermal contact is unacceptable in combination with brachytherapy afterloading techniques. In fact it can be considered favourable that the recorded temperature represents the mean over a few millimetres of tissue. A super local temperature is not representative of the average local tissue temperature, and therefore not suitable for power steering.

Our objective was to study applicator and catheter related causes of temperature measurement errors. We did not present a parametric study of the influence of blood flow on the temperature distribution near the applicators, although it would not have been difficult to include blood flow effects into the heat transfer model by introducing a non-zero heatsink and/or an enhanced thermal conductivity term (Pennes, 1948; Crezee et al., 1994; ESHO task group report 4, 1992). However, we felt this would complicate analysis unnecessarily. Some general comments: the anticipated effect of blood flow is effectively a lower tissue heat resistance; regardless of what model is used (heatsink, k_{eff}), the thermal resistance of the catheter wall would become relatively larger, resulting in a larger temperature drop over the catheter wall than without blood flow. This would support the need to avoid selfheating in the catheter.

Chapter 6

Temperature control in MECS interstitial hyperthermia: impact of longitudinal control in model anatomies.

6.1   Introduction

Local hyperthermia systems currently in practical use are limited in providing control of the temperature distribution reached during treatment. This fact is reflected in the poor temperature distributions obtained in the clinic: the heating systems are unable to cope with the complex cooling field and tissue heterogeneity present in the treatment volume (Oleson et al., 1993; Chato, 1990; Lagendijk, 1990a; Paulsen, 1990b; Roemer, 1990b; Lagendijk et al., 1994b). Our simulations and model experiments suggest that the problem of controlling the blood flow related spatial variation of the temperature in local hyperthermia can be solved: if the power deposition (SAR) can be controlled at a centimetre scale, the vascular cooling can be accounted for and excellent temperature distributions can be expected (Crezee and Lagendijk, 1992; Lagendijk et al., 1993, 1994b). In electromagnetic hyperthermia techniques the spatial variation of the electrical conductivity further complicates the control of the temperature in the target volume (Paulsen, 1990b; Sowinski and van den Berg, 1990). Large contrasts in the electrical conductivity occur in clinical situations (Johnson and Guy, 1972; Hand et al., 1982; Chen and Gandhi, 1989; Stuchly et al., 1982).

Along with the great electrical contrast, the (effective) thermal conductivity, the specific heat and the micro-vascular perfusion may also vary considerably (Chen and Holmes, 1980; Lagendijk et al., 1988; Lyng et al., 1991; Bowman et al., 1992).

In this chapter the influence of the (bulk) tissue inhomogeneity will be considered. The MECS technique is designed to deposit RF-energy in tissue through electrodes inserted in plastic catheters (Visser et al., 1989). Several independent electrodes can be operated in a single catheter. This provides control of the power deposition

along the catheters so that the power can be adapted to possible inhomogeneities. A thermocouple string inside the catheter is used to measure the temperature along the probes, allowing direct feedback power control.

The simulations are performed using temperature data obtained with our finite difference SAR and thermal models (Lagendijk et al., 1995; Kotte et al., 1996b; De Bree et al., 1995). The programs allow the modelling of fully inhomogeneous tissue properties. The anatomies used in this chapter are uncomplicated and allow focusing on some important tissue related criteria for the design of treatment plans for IHT. Discrete vasculature is not considered here. Although the incorporation of discrete vasculature in the models is essential for obtaining information on the details of the temperature distribution, in this study we focus on the effects of tissue heterogeneity (Chato, 1990; Lagendijk, 1990a; Roemer, 1990b). We have evaluated cases with a pure k_{eff} approach and, alternatively, using the mixed k_{eff}/bioheat transfer equation (Crezee et al., 1994).

6.2   Methods

6.2.1   Computer simulation

The SAR model and the thermal model used to investigate the MECS system are part of the interstitial hyperthermia treatment planning system which is being developed in Utrecht (Lagendijk et al., 1995; De Bree et al., 1995; Kotte et al., 1996b). The models are used to simulate treatments using the MECS IHT system in pre-defined anatomies. Model resolution and volume are limited by the data acquisition resolution and by computer memory; in general, we can work with voxel space of $100 \times 100 \times 100$ voxels and a spatial resolution of 1 mm. The models used in the simulations described here had a size of $25 \times 25 \times 40$ voxels, the voxels had a size of 2 mm in each direction. The reason for the rather coarse grid size was the gain in speed of the simulations (about two instead of 60 hours of processor time to reach steady state for a single simulation setup). The results of the coarse grid simulations were consistent with sample runs performed at a grid spacing of 1 mm.

During treatment simulation, the SAR model and the thermal model are executed in turn. Electrode currents for the SAR model are determined from the output of the thermal model and the electrode currents used in the previous cycle of the simulation. Employing the assumption that there is a proportional relation between the square of the output current I and the temperature at the control

point T we compute the new current I_{new} from the old temperature $T_{control}$ (which is the highest temperature occurring in the set of voxels constituting the electrode considered), the old current I_{old} and the setpoint temperature T_{set} as follows:

$$I_{new} = I_{old} \sqrt{\frac{T_{set}}{T_{control}}}.$$

This procedure converges if a suitable value for the time interval of a single run of the thermal model is chosen. After a sufficient number of iterations of the control loop, the simulation reaches a steady state where all electrode temperatures are at their set point and the temperature in the whole of the volume becomes stable. At this point, the maximum temperature in the volume is close to the setpoint temperature; the SAR is highly peaked near the catheters and there are no other SAR maxima in the volume; the temperature maxima occur near the electrodes, where the temperature is limited to the setpoint temperature by the control algorithm. The resulting steady state temperature distribution is used to evaluate the treatment setup considered.

The power deposition model

The estimated power density distribution ($[\mathrm{W\,m^{-3}}]$) in the modelled implant is computed using a finite difference algorithm solving the Poisson equation (Sowinski and van den Berg, 1990)

$$-\boldsymbol{\nabla}{\cdot}\kappa\boldsymbol{\nabla}V + \boldsymbol{\nabla}{\cdot}J_{source} = 0. \tag{6.1}$$

This PDE follows from a quasi-static approximation of the Maxwell equations. The electrodes are described in a grid independent fashion using an analytical approximation of the potential distribution near the electrodes (De Bree et al., 1996b).

The power deposition is derived from the calculated potential distribution, combined with the electrical media properties.

The thermal model

The thermal model is based on a finite difference algorithm, solving the mixed heatsink/k_{eff} bioheat transfer equation (Kotte et al., 1996b; Pennes, 1948; Crezee et al., 1994; ESHO task group report 4, 1992):

$$\rho c_{tis}\,\frac{\partial T}{\partial t} = \boldsymbol{\nabla}{\cdot}\left(k_{eff}\boldsymbol{\nabla}T\right) + P + fW_b c_b\left(T - T_{art}\right), \tag{6.2}$$

where ρ is the density in $\left[\text{kg}\,\text{m}^{-3}\right]$, c_{tis} the tissue specific heat in $\left[\text{J}\,\text{kg}^{-1}\,\text{K}^{-1}\right]$, k_{eff} is the thermal conductivity in $\left[\text{W}\,\text{m}^{-1}\,\text{K}^{-1}\right]$, P is the power absorption rate in $\left[\text{W}\,\text{m}^{-3}\right]$. The modification factor f, dependent on counter-currency and vascular network properties, was chosen equal to 1.0, W_{b} is the volumetric perfusion rate in $\left[\text{kg}\,\text{m}^{-3}\,\text{s}^{-1}\right]$ and c_{b} the specific heat of blood in $\left[\text{J}\,\text{kg}^{-1}\,\text{K}^{-1}\right]$. Without loss of generality, the arterial inflow temperature T_{art} is taken equal to zero. The discrete vessel facilities of the thermal model were not used for the simulations described in this chapter.

6.2.2   Model anatomies

To investigate the influence of longitudinal control in the MECS system we have performed computer simulations in several anatomical models. The implant is a hexagonal prism with a length of 50 mm. The catheters are placed along the vertices and long axis of the prism with a spacing of 15 mm. The two main variables in the simulations were the anatomical structures in which the simulations were performed and the number of individually controllable segments per implanted probe. Allowing for some margin around the implant the grid size was chosen at (50 mm × 50 mm × 80 mm).

The following four anatomies were defined:

1.   homogeneous tissue [homogeneous];
2.   two half-spaces, interface plane perpendicular to long axis of implant [horizontal plane];
3.   two half-spaces, oblique to interface plane [oblique plane];
4.   two half-spaces, interface plane parallel to main axis of implant [vertical plane].

In the text, we refer to these media configurations using the designations between square brackets.

The given anatomies facilitate investigation of a number of basic situations arising in clinical practice. Figure 6.1 illustrates the principle planes of the interfaces between the half-spaces present in the modelled implants.

Tissue properties

The thermal and electrical tissue properties used in the simulations represent plausible contrasts and are summarised in table 6.1.
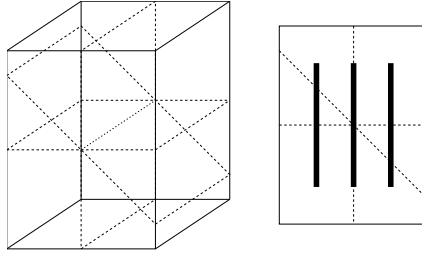
Figure 6.1: Illustration of the orientation of the principal planes of the interface between contrasting tissues used in the simulations.

Table 6.1: Thermal and electrical tissue properties used in the simulations.

simulation	tissue	perfusion $[\mathrm{kg\,m^{-3}\,s^{-1}}]$	eff. conductivity $[\mathrm{W\,m^{-1}\,K^{-1}}]$	σ $[\mathrm{S\cdot m^{-1}}]$	ϵ $[1]$
homogeneous	high cond	0	0.6	0.70	80
heterogeneous					
'muscle'	high cond	0/6.5	2.0	0.76	112
'fat'	low cond	0/1.5	0.5	0.23	22

In the table, *Homogeneous* corresponds to the homogeneous anatomy, *Heterogeneous* to the situations with half-spaces. g The fat and muscle tissue properties were taken from the averaged values in the ESHO/COMAC task group report on treatment planning and modelling in hyperthermia (ESHO task group report 4, 1992). When moderately high perfusion levels of $6 \ kg \ m^{-3} \ s^{-1}$ for 'muscle' and $1.5 \ kg \ m^{-3} \ s^{-1}$ for 'fat' are assumed, a k_{eff}/k ratio of about 3 can be expected, which yields the values tabulated (Crezee et al., 1991).

Two levels of blood flow were investigated using the heat sink (W_b) term present in the thermal model: zero blood flow and the higher blood flows just mentioned.

This variation was applied to investigate the qualitative influence of the heatsink on the results.

Boundary conditions

The boundary conditions on the computational volume influence the shape of the electrical potential and temperature distributions at and inside the convex hull of the implant.

At the border of the computational grid the electrical conductivity is set to 1/10 of the lowest tissue conductivity to simulate a shell of 10 mm extra tissue between the interior of the computational volume and its (fixed potential) boundary, which is then effectively at some 20 mm from the implant. In this way, the number of voxels in the model can be kept limited, while the potentials are not influenced too much by a near-by boundary.

The fixed temperature boundary conditions mimic the presence of large thermally unequilibrated vessels at 37°C at some distance from the implant by choosing the thermal conductivity at the boundary of the computational volume equal to 1/10 of the lowest tissue conductivity in the model volume. This effectively moves away the fixed temperature border of the computational grid to about 20 mm from the implant.

Implant definition

The basic configuration is an implant with the 'needles' or 'probes' placed on a hexagonal grid with a nearest neighbour distance of 15 mm. In each probe, between 1 and 4 electrodes are placed along an 'active section' which has a length of 50 mm (see figure 6.1). The ratio of the length of the electrodes to the length
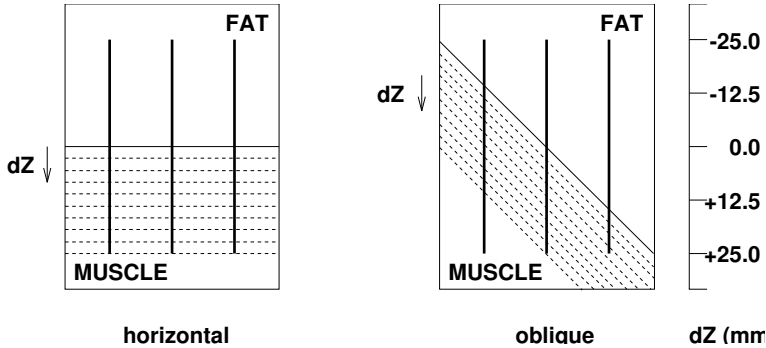
Figure 6.2: Variation of media interfaces with respect to implant. The implant remains at the same position in the volume, the interface shifts with respect to the implant. dZ denotes the vertical component of the shift which varies between 0 mm and 25 mm.

of the gaps between the electrodes was $2:1$, Thus, the electrode segments had lengths of $50, 20, 12$ and 9 mm.

The modelled electrodes have a diameter of 2.1 mm. The computational grid has a resolution of 2 mm. The potential distribution calculated by the SAR model was corrected for the discretisation errors occurring near the electrodes using the method described by De Bree et al. (1996b).

The position of the interface between the media was varied by shifting it from the centre of the implant outwards. Thus, the ability of an implant to cope with unknown details of the tissue properties in the target volume was investigated. This is essentially a situation in which no planning is done before treatment.

In figure 6.2 the variation of the position of the media interface in the computational volume is illustrated.

6.2.3   Target volume

The target volume or region of interest is the set of voxels used to evaluate temperature distributions. It is desirable to select a volume which is 'clinically relevant'; there are many seemingly equivalent alternatives at hand (Dutreix, 1988). The target volume chosen here is the convex hull of the active sections of the implant, limiting evaluation of temperature distribution to the bulk of the implant.
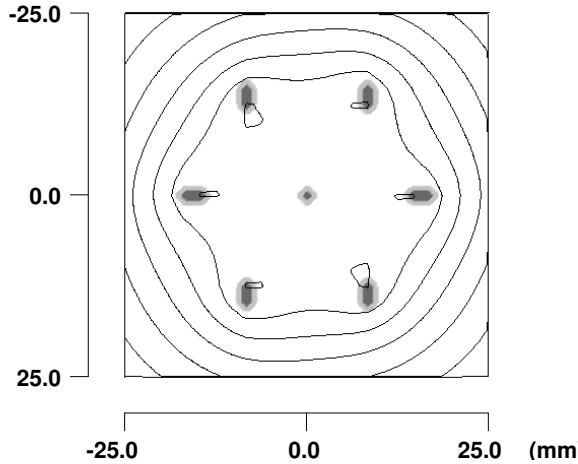
Figure 6.3: Homogeneous anatomy, cross-section perpendicular to the modelled needles. The needles are shown in grey. Iso temperature contours in the central plane superimposed on the anatomy. The highest contour is at $44°$C. Contours are $1°$C apart.

6.2.4   Comparison of distributions

The Cumulative Temperature Volume Histogram (CTVH) is used to judge the quality of the temperature distribution in the target volume. To facilitate a comparison of many different simulations a simple measure of the quality of the resulting temperature distribution is desired. In this case, $T_{10} - T_{90}$ has been used, which has the drawback that information about absolute temperature levels is lost. In these simulations that is not a problem because T_{10} is close to the set-point temperature due to the control method used.

In this thesis, the convention is used that n percent of the volume of interest has a temperature *higher than* T_n. For instance, if $T_{10} = 5.0$ K, the volume fraction with a temperature higher than 5.0 K is 10 %.
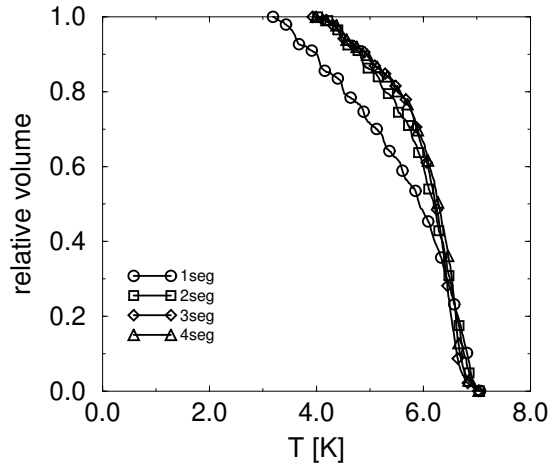
Figure 6.4: Homogeneous anatomy, cumulative temperature volume histogram for four different segmentations of the electrodes along the active sections. The interface plane is through the centre of the implant ($dZ = 0$)

6.3 Results

6.3.1 Homogeneous volume

A cross section through a plane containing electrodes in the anatomy used for the calculations in the homogeneous volume is shown in figure 6.3. The tissue properties used in the homogeneous volume can be found under 'homogeneous' in table 6.1.

The bio heat transfer factor W_b was not varied and equal to zero.

The results from the simulations are summarised in figure 6.4. Clearly, the CTVH is very similar for different longitudinal segmentations. The single electrode result is slightly more inhomogeneous than the other simulated temperature distributions.

6.3.2 Dual media

The dual media simulations shown here were set up with the tissue properties shown under 'muscle' and 'fat' in table 6.1. Three orientations of the interface plane with respect to the long axis of the implant were investigated (see figure 6.1).
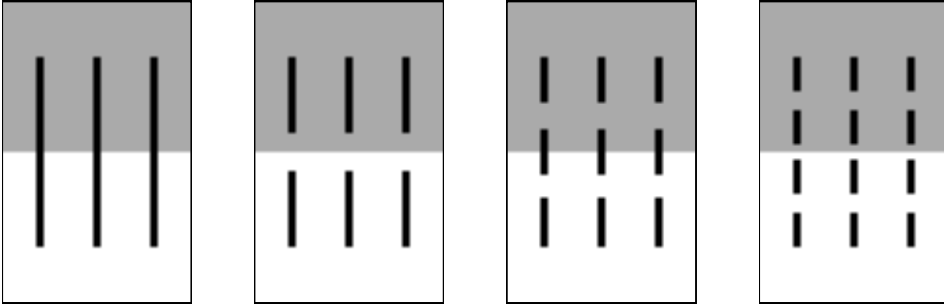
Figure 6.5: Horizontal inhomogeneity: cross-section of anatomy with the four different implants. $dZ = 0$. Gray is fat, white is muscle.

Horizontal division

The simulations with the interface plane between the contrasting media parallel to the long axis of the implant were performed using the anatomy depicted in figure 6.5. This figure illustrates the four different electrode segmentations used throughout this chapter.

All simulations involving the horizontal plane were performed in duplo, with and without a heatsink (W_b) term in the calculations. In the range of W_b's employed no significant effect on the $T_{10} - T_{90}$ was observed. However, as can be seen by comparing figures 6.7 and 6.6 there is a longer tail on the CTVH's in the $W_b > 0$ case. This means that both T_{10} and T_{90} have shifted to lower temperatures. In the $W_b > 0$ case the power output of the modelled electrodes was consistent with the expected larger heat removal from the volume due to the presence of a non-zero heatsink term.

The results of a number of steady state simulations with the interface plane displaced in the direction of the long axis of the implant (the normal on the interface plane) can be found in figures 6.8 and 6.9. $T_{10} - T_{90}$ is in the order of $2\,K$ in the most favourable cases. This is the residual inhomogeneity, which is also present in the homogeneous case (see figure 6.4, page 83). In contrast with the homogeneous case, the single electrodes perform badly, with $T_{10} - T_{90}$ equal to about 5 K in all cases.

Note that $T_{10} - T_{90}$ increases significantly when the planes of electrodes located closest to the border of the implant are reached by the interface. This is caused by the fact that the temperature gradients in the interior of the implants are relatively
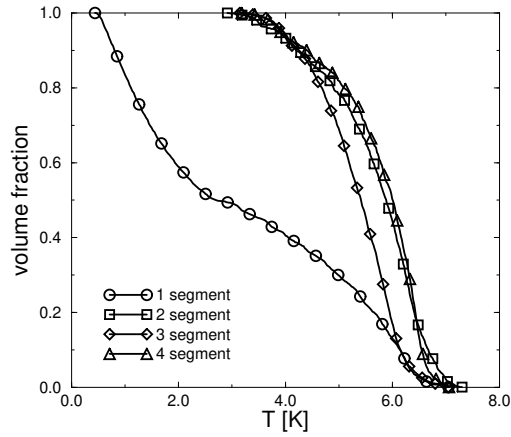
Figure 6.6: Horizontal inhomogeneity: Cumulative temperature/volume histogram for the convex hull of the implant for the case $dZ = 0$. $W_b = 0$.
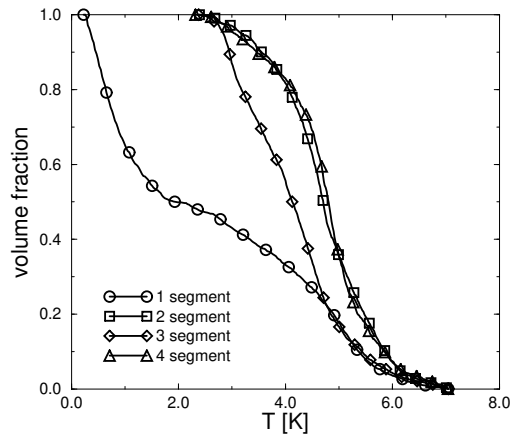

Figure 6.7: Horizontal inhomogeneity: Cumulative temperature/volume histogram for the convex hull of the implant for the case $dZ = 0$. $W_b > 0$.
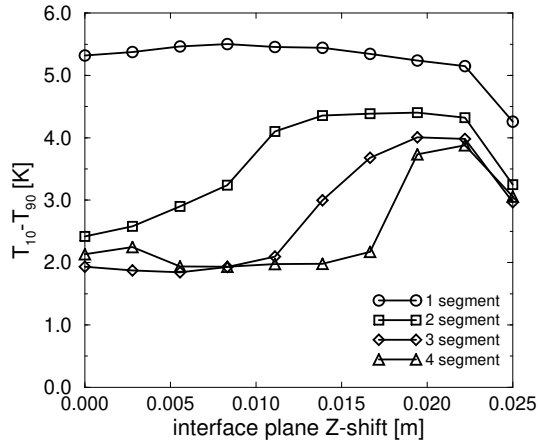
Figure 6.8: Horizontal inhomogeneity: variation of $T_{10} - T_{90}$ versus offset dZ of interface plane. $W_b = 0$.
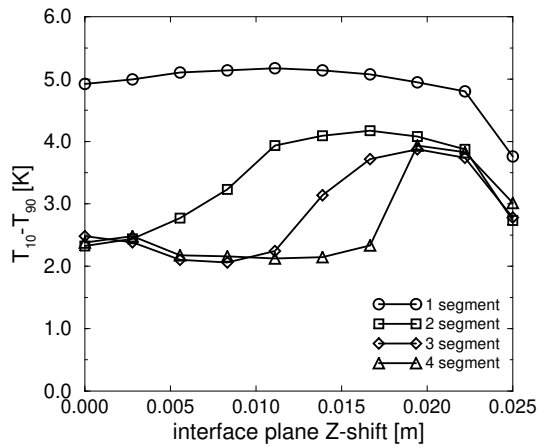

Figure 6.9: Horizontal inhomogeneity: variation of $T_{10} - T_{90}$ versus offset dZ of interface plane. $W_b > 0$.
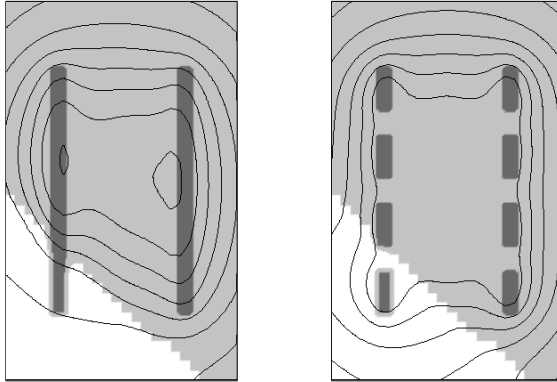
Figure 6.10: Oblique inhomogeneity, temperature contour in a plane parallel to the long axis of the implant and perpendicular to the tissue interface plane, through two catheters. White is muscle, grey is fat. $dZ = 25$ mm. To the left, mono electrodes are shown. To the right, the active section contains four electrodes. Notice the dramatic improvement in the temperature distribution. The highest temperature contour is at 6 K temperature raise, the contours are 1 K apart.

small, as long as the temperature at the boundaries of the implant is near the setpoint. When the outer layer of sources becomes affected, the temperatures at the border can no longer be maintained and the temperature control in the target volume is compromised.

Oblique division

The results for the oblique interface plane are similar to the results for the horizontal plane but the variation of $T_{10} - T_{90}$ is smaller. This is because a smaller number of boundary sources are jointly influenced, they are further apart and neighbouring sources can, to some degree, make up for the loss of power deposition of the affected electrodes.

Notice the failure of the mono-electrodes in the temperature/volume histogram in figure 6.11.
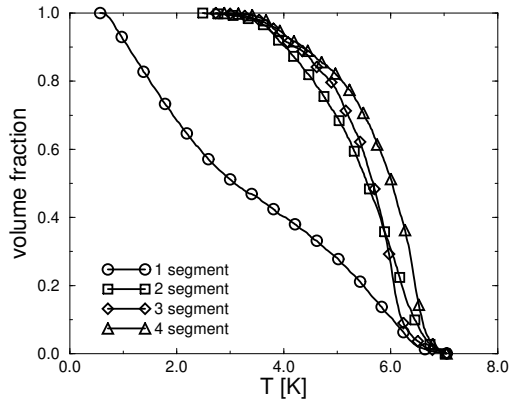
Figure 6.11: Oblique inhomogeneity: cumulative temperature/volume histogram for the convex hull of the implant. $dZ = 0$
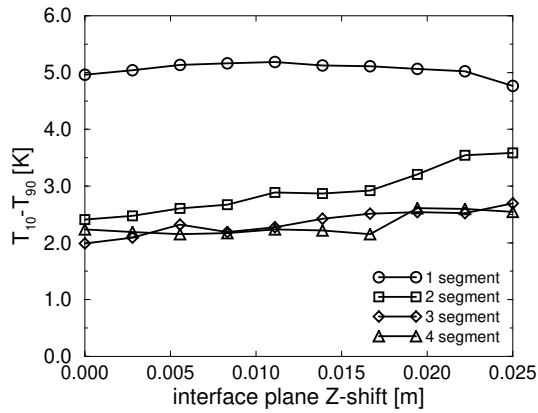

Figure 6.12: oblique inhomogeneity: variation of $T_{10} - T_{90}$ versus offset dZ of interface plane.
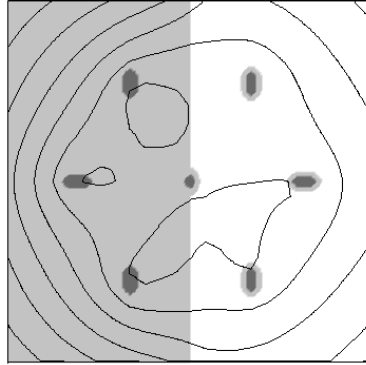
Figure 6.13: Vertical inhomogeneity, anatomy. Grey is fat, white is muscle. The electrode configuration was $+\overset{-+}{-}+$. The highest contour is at $44°$C; no temperature in the shown central plane is above $44.2°$C. Contours are $1°$C apart.
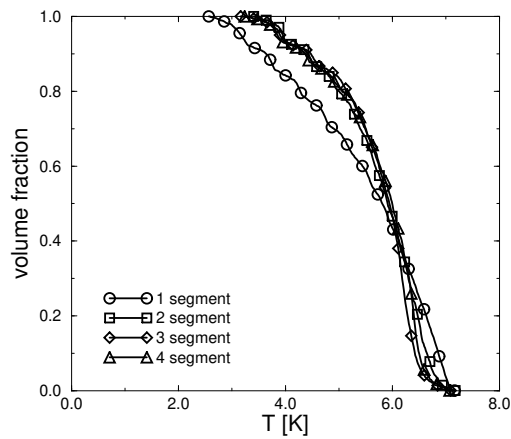

Figure 6.14: vertical inhomogeneity, CTVH. The plane position was through the centre of the implant ($dX = 0$).
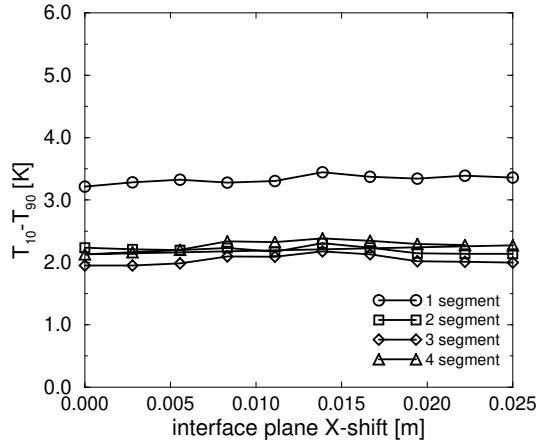
Figure 6.15: Vertical inhomogeneity: variation of $T_{10} - T_{90}$ versus offset of interface plane.

Vertical division

The simulations for the case where the interface between the contrasting media was oriented parallel to the long axis of the implant were performed using the anatomy depicted in figure 6.13. The iso-temperature plot shows a nice distribution, although the temperature distribution contains regions with temperatures slightly above the setpoint (excess < 0.2 K). This is partly due to the electrode phase configuration.

The CTVH of the target volume for the simulation with the interface plane through the centre of the implants is shown in figure 6.14; the cumulative histograms are very similar to those of the homogeneous simulation, depicted in figure 6.4 (page 83). The CTVH's of simulations performed in the same implants with the interface plane displaced in the X-direction are shown in figure 6.15. It is clear that the inhomogeneity has virtually no effect on $T_{10} - T_{90}$. This is due to the fact that none of the electrodes passes perpendicular through the interface between the media.

6.4 Discussion and conclusions

6.4.1 Anatomies and tissue properties

Idealised anatomies are used in this chapter. The binary media anatomies, containing media interfaces oriented parallel, perpendicular or oblique with respect to the long axis of the implant represent simple anatomies which can be encountered in clinical implants. A homogeneous anatomy is used as a control.

The tissue properties used in these simulations represent a relatively large inhomogeneity of the thermal and electrical properties. The inhomogeneities encountered in clinical practice may be smaller.

6.4.2 Comparison of results with clinical data

The cumulative temperature/volume histograms used here as a primary means of evaluating temperature distributions in a target volume were constructed from the calculated temperatures of all voxels in the simulation target volume at a single point in time. They are not directly comparable to CTVH's obtained in clinical measurement; in general, the latter are constructed from thermal sensor readings at a limited number of locations in the target volume during an extended period during which the temperature distributions are subject to change. Because of this sample collection procedure the clinically measured CTVH's contain systematic errors.

Kapp *et al.* achieved a $T_{10} - T_{90}$ of 3 K and a $T_{90} \simeq 40.7°$C in anal carcinoma treated with hot water tubes, a system with reasonable longitudinal control (Kapp et al., 1993). Results from interstitial systems without longitudinal control, similar to our single electrodes, yield higher values of $T_{10} - T_{90}$. For example, using microwave antennas in brain, Seegenschmiedt found a $T_{10} - T_{90} = 3.4$ K at $T_{90} = 39.8°$C. Prionas obtained $T_{10} - T_{90} \simeq 4.5$ K with $T_{90} = 39.6°$C in the prostate, using an RF system,

The clinical data quoted above were obtained using thermometry in dedicated catheters so that the $T_{10} - T_{90}$'s are probably too low due to an underestimation of T_{10}. Ryan *et al.* also included temperature data from within the applicators and obtained a $T_{10} - T_{90} \simeq 8$ K at $T_{90} = 40.8°$C using microwave antennas in the brain (Ryan et al., 1994).

A more correct, practical way of comparing clinical results with the model calculations could be to reconstruct CTVH's from the simulations containing similar systematic errors by sampling the computed temperature distribution in a comparable way, choosing measurement points along representative catheter tracks.

6.4.3   Influence of W_b on the temperature distributions

The temperature distributions simulated in this chapter are dominated by conductive transport of heat from the implant. Comparison of heat removal due to the heatsink term in (6.2) with the conductive heat transport through the convex hull of the implant reveals that these two terms become equal only for very high W_b, much higher than the values used in this chapter. This reflects the fact that the implants are small (the volume in the convex hull of the active sections was 43 cc) and have a relatively large surface/volume ratio, which is true for most interstitial implants.

When the perfusion term W_b is varied within moderate limits, effects observed on $T_{10} - T_{90}$ are small (see figures 6.8 and 6.9, page 86). However, the absolute values of T_{10} and T_{90} decrease when W_b increases, indicating a steeper temperature gradient near the electrodes than in the non-perfused case (see figures 6.6 and 6.7). This is in accordance with the results published in literature (Strohbehn, 1983; Strohbehn et al., 1982; Mechling and Strohbehn, 1986; DeFord et al., 1991; Crezee et al., 1991). At the chosen values of W_b we observed that the calculated temperature profiles were effectively independent of the thermal conductivity chosen at the boundary of the computational grid. This means that in this case the heat sink determines the boundary condition but still most of the heat is removed from the implant by thermal conduction through its convex hull.

6.4.4   Treatment planning and spatial control

This study shows that even with high contrasts in electrical and thermal conductivity in the implant it remains possible to obtain satisfactory temperature distributions with the MECS system. Due to its 3D spatial control the temperature homogeneity in the implant can be made quite satisfactory, with $T_{10} - T_{90}$ in the order of 2–3 K. Treatment planning must ensure that the placement of the current source electrodes is compatible with the media configuration.

Treatment planning can be traded to spatial control. A good temperature distribution can be achieved if there is enough control over the physical SAR distribution to cope with the cooling field. Scanned focussed ultrasound systems provide this and have the advantage of not being invasive; however, insufficient information on the temperature distribution is available for on-line adjustment of the power deposition. The solution of this problem is the insertion of temperature sensors in the treatment volume—losing the advantage of non-invasiveness. The MECS interstitial hyperthermia system provides both 3D spatial SAR control and the thermometry required for feedback control.

The minimum sensible length of the individual controllable electrodes is in the order of the catheter spacing. Using shorter electrodes does not notably improve the temperature distributions in well-positioned implants. Temperature control improves dramatically when going from a single to two segments; further segmentation has less effect (see paragraph 6.3.2). To further improve the temperature distributions the spacing between the catheters, 15 mm in the simulations, may be decreased, which would improve the lateral SAR control.

Inhomogeneities present in the implant volume lead to inferior temperature distributions if no longitudinal SAR control is available in the interstitial system used: It is then impossible to devise an electrode configuration compatible with the anatomy (Prionas et al., 1994). If there is a limited amount of spatial control and the inhomogeneities are of comparable or larger scale, careful planning of the geometrical electrode configuration is essential. The performance of electrodes extending through the interface between media can be compromised, as shown in figure 6.10. The hot spot that develops in the less conductive medium limits the power output of the affected electrode, leading to a cold spot in the other medium. Although effects seen in the CTVH may not be spectacular, there can be significant local deviations from the prescribed temperature, which may have consequences for tumour control (Oleson et al., 1993).

The results in sections 6.3.2 and 6.3.2 suggest that inhomogeneities in the tissue properties within the implant have less impact than those at the boundaries of the implant (see figures 6.12 and 6.8), where the temperature gradients are larger. However, the inhomogeneities modelled here are of quite simple nature; in tumours irregular spatial variations of the tissue properties can be expected. In particular, when thermally significant discrete vasculature is present in the tumour volume, large gradients of the temperature within the implant can result (Lagendijk et al., 1994b). The behaviour of the MECS system in more realistic anatomies, containing discrete vessels, is investigated in the next chapter.

Chapter 7

The influence of vasculature on temperature distributions in MECS interstitial hyperthermia: importance of longitudinal control

7.1 Introduction

Recent clinical phase III trials using external hyperthermia techniques have clearly demonstrated the beneficial effect of thermoradiotherapy (Overgaard et al., 1995; Van der Zee, 1993; Vernon et al., 1996). The major problem in local hyperthermia and the major reason for the failure of several clinical studies is that the present heating systems still have a limited capability of providing the thermal dose and temperature control clinically wanted (Perez et al., 1989; Oleson et al., 1993). In regional hyperthermia, because of the limited cooling by the vasculature following from the systemic temperature rise and the large volumes heated, relatively uniform temperature distributions can be obtained (Lagendijk, 1990b; Van Es et al., 1995; Wust et al., 1995). In interstitial hyperthermia the absence of vascular preheating, tissue heterogeneity and the limited control capabilities result in inadequate temperature/thermal dose uniformities (Lagendijk, 1990b; Roemer, 1990b; Goffinet et al., 1990; Van der Koijk et al., 1996; Corry et al., 1988). Despite the unfavourable thermal dose distributions reasonable results have been obtained in some clinical studies using interstitial heating techniques (Cosset, 1990; Salcman and Samaras, 1983; Roberts et al., 1986; Silberman et al., 1985). However, the recent phase III RTOG trial showed no additional beneficial effects of interstitial thermoradiotherapy over interstitial radiotherapy alone (Emami et al., 1996). In this trial only one patient out of 86 received an adequate hyperthermia dose; it was stated that substantial technical improvements are needed before (new) properly randomized clinical trials can be initiated (Emami et al., 1996).

Simulations and experimental research show that the temperature uniformity can

be improved; by spatial control of the absorbed power (SAR) distribution at a centimetre scale excellent temperature uniformity can be achieved; local blood flow cooling can be compensated for and hot spots related to tissue heterogeneity can be prevented (Crezee and Lagendijk, 1992; Lagendijk et al., 1993, 1994b; Van der Koijk et al., 1996). Spatial SAR control at this scale can in principle be obtained with recently developed 3D controlled interstitial hyperthermia (IHT) systems and scanned focused ultrasound (SFUS) systems. Where the latter, for achieving this goal, are handicapped by the absence of massive invasive thermometry, IHT systems can in principle use extensive thermometry from within the catheters/needles already present or rely on intrinsic temperature control (hot source/thermal conduction techniques) (Lele, 1983; Fessenden et al., 1984; Lagendijk et al., 1994a; Hand et al., 1991; Cetas et al., 1994; Van Wieringen et al., 1996b).

Visser et al. (1989) and Marchal et al. (1989) developed 27 MHz current source interstitial hyperthermia techniques using metal electrodes inserted in standard plastic brachytherapy catheters. Current source techniques allow flexible RF-current control because of the absence of coupling between electrodes and the uniform current injection along the electrodes (Deurloo et al., 1991). We developed the multi-electrode current source (MECS) technique, which is based on the current source technology, in a collaboration with the Dr. Daniel den Hoed Cancer Center (Rotterdam, the Netherlands). To exploit the full potential of 3D spatial SAR control a 64 channel interstitial hyperthermia system based on this technology was designed (Lagendijk et al., 1995). The system contains an integrated 196 channel thermometry unit. This IHT system should be capable of providing 3D SAR control at a centimetre scale.

Computer simulations offer a powerful and versatile test method for the comparison of the capabilities of different interstitial heating systems. So far, most of the relevant literature concentrated on homogeneous phantoms, 2D SAR control and thermal models without discrete vessels (DeFord et al., 1991). This sufficed for performing comparative tests of the properties of the different 2D controlled IHT techniques (Strohbehn, 1983; Strohbehn et al., 1982; Stauffer et al., 1989). Now that reliable 3D SAR and thermal models are becoming available, simulations incorporating complex 3D heterogeneities become feasible. We have developed a treatment planning system capable of simulating MECS-implants in tissues with arbitrary vessel networks (De Bree et al., 1996b; Kotte et al., 1996e). In a case study of a brain implant, Lagendijk et al. (1995) demonstrated the effectiveness of 3D SAR steering with the MECS IHT system in a volume with a very heterogeneous large vessel density. Spatial control in a heterogeneous dielectric anatomy using the MECS system, notably at fat-muscle interfaces, has been investigated

by Van der Koijk et al. (1996).

In this chapter the capabilities of the MECS IHT technique in anatomies containing three-dimensional vessel structures are investigated. A target volume is heated with simulated interstitial implants with and without longitudinal steering along the catheter, modelling systems with 2D- and 3D-SAR control. By varying the large vessel network properties the influence of heterogeneity in tissue cooling on the steady state temperature distributions achieved could be investigated.

7.2   Methods

7.2.1   Computer simulation

The SAR model and the thermal model used for the investigation of the MECS system are part of the interstitial hyperthermia treatment planning system which is being developed in Utrecht (Lagendijk et al., 1995; De Bree et al., 1996b; Kotte et al., 1996b). During treatment simulation, the SAR model and the thermal model are executed in turn. Electrode currents for the SAR model are determined by comparing electrode temperatures from the output of the thermal model with the set point temperatures, using the electrode currents from the previous cycle of the simulation. After a sufficient number of iterations of the control loop, the simulation reaches a steady state: all electrode temperatures are at their set point and the temperatures in the whole of the volume, including the vascular structures, are constant. At this point, the maximum temperature in the volume is close to the setpoint temperature; the SAR is highly peaked near the catheters and the temperature maxima occur near the electrodes, where the temperature is limited to the setpoint temperature by the control algorithm. The resulting steady state temperature distribution is used to evaluate the treatment setup considered.

The power deposition model

The estimated power density distribution in the modelled implant is computed using a finite difference algorithm solving the Poisson equation (Sowinski and van den Berg, 1990; De Bree et al., 1996b)

$$-\boldsymbol{\nabla}\cdot\kappa\boldsymbol{\nabla}V + \boldsymbol{\nabla}\cdot J_{\text{source}} = 0. \tag{7.1}$$

V is the electric potential, κ the complex admittance and J_{source} is the current density at the sources. The capacitive coupling between the metal electrode and

the tissue, through the catheter in which it is inserted, allows the electrode to be modelled as a current-source (Deurloo et al., 1991). In our model, the current-source electrodes are described as cylinders with a uniform current density normal to their surface (De Bree et al., 1996b). The geometrical form of the electrode is defined in a global coordinate system. This makes the electrode description independent of the grid resolution. The location of the tissue volume is also defined in the global coordinate system, so that the location of the electrodes relative to the volume is known.

If an electrode with an outer diameter in the order of the grid spacing is discretised, the cross-section of the electrode contains a small number of nodes. The discretisation does not do justice to the actual diameter of the electrode. The calculated potential in the electrode nodes is not equal to the actual local electrode potential. On the other hand the potentials in the tissue nodes away from the electrodes represent the actual potential distribution in the tissue. To estimate the actual electrode potential we developed an analytical approximation of the potential in the direct neighbourhood of the electrode (De Bree et al., 1996b).

The power deposition distribution is derived from the calculated potential distribution, combined with the electrical media properties.

The thermal model

Our thermal model has provisions for dealing with the convective heat transport by direct modelling of discrete vessels. Direct simulation of vessel structures in the finite difference grid is not flexible (Mooibroek and Lagendijk, 1991). One of the most important limitations of that approach is the strong dependency on resolution and the difficulty of specifying the geometrical properties of the vascular structures. In our new finite difference model, vascular structures are represented as trees of parametrically described vessel segments which are linked together according to the tree topology (Kotte et al., 1996e). The vessel segments are thus defined independent of the grids used in the actual computations. The heat flow between the vessels and the surrounding tissue is calculated from the mixing-cup temperatures in the vessels and the temperature of tissue voxels neighbouring the vessels, using an analytical approximation of the temperature profile near a vessel. In order to maintain heat balance, the heat flow is taken into account in both the vessel tree and the finite difference grid. Several vessel trees together represent the arterial and venous vessel structures in a volume of tissue. At points where vessel segments are joined, blood flux conserving boundary conditions are applied. The

behaviour of the discrete vessel model has been investigated in detail for single vessels and for counter current pairs (Van Leeuwen et al., (submitted-b,s).

The time evolution of the tissue temperature is calculated with the use of a finite difference scheme based on equation (7.2) (Mooibroek and Lagendijk, 1991; Kotte et al., 1996e; Crezee et al., 1994; ESHO task group report 4, 1992). To allow comparison with previous studies we have used the bioheat transfer sink term (Pennes, 1948).

$$\rho c_{tis} \frac{\partial T}{\partial t} = \boldsymbol{\nabla} \cdot (k_{eff} \boldsymbol{\nabla} T) + P + f W_b c_b (T - T_{art}), \qquad (7.2)$$

where ρ is the density in $kg\,m^{-3}$, c_{tis} the tissue specific heat in $J\,kg^{-1}\,K^{-1}$, k_{eff} the effective thermal conductivity in $W\,m^{-1}\,K^{-1}$, P the power absorption rate in $W\,m^{-3}$. The collective influence of vasculature may be taken into account by a combination of a heatsink (third right hand term) and adjusting the effective tissue conductivity k_{eff}. W_b is the volumetric perfusion rate in $kg\,m^{-3}\,s^{-1}$ and c_b the specific heat of blood in $J\,kg^{-1}\,K^{-1}$. The modification factor f, which depends on counter-currency and vascular network properties, was chosen equal to 1.0. Without loss of generality the simulation baseline temperature and arterial inflow temperature T_{art} was set to zero K above baseline. The baseline temperature corresponds to the body core temperature.

7.2.2 Model anatomies

To investigate the interplay of the spatial SAR control enabled by the MECS IHT system and the complex cooling field originating from the vascular structures in the implant volume we have performed computer simulations in several (more or less representative) anatomical models. The convex hull of the MECS-implant is a hexagonal prism with a length of 50 mm. The 'catheters', or implant tracks, are placed along the vertices and the central axis of the prism with a spacing of 15 mm. The geometry of the implant is illustrated in figures 7.2 and 7.4. The two main variables in the presented simulations are the topology and location of the vascular network structures in the simulation volume *and* the number of individually controllable segments per implanted catheter (the longitudinal control). In each interstitial catheter with a diameter of 2.1 mm between 1 and 4 electrodes were placed along an 'active section' with a length of 50 mm. The electrode segments had lengths of 50, 20, 12 and 9 mm. Allowing for some margin around the implant the dimensions of the modeled volume were chosen to be (50 mm × 50 mm × 80 mm). At the border of the computational grid the thermal conductivity is set to 1/10 of that of muscle to simulate a shell of 10 mm extra tissue between the interior

of the computational volume and its (fixed temperature) boundary, which is then effectively at some 20 mm from the convex hull of the implant (Van der Koijk et al., 1996). The setpoint temperature (highest temperature at the electrodes) was chosen at 7 K above the baseline. Vascular inflow temperature was at the baseline temperature. Several vascular network structures were investigated:

▷ a single non-equilibrated vessel passing through the implant volume with various orientations and positions, showing the effects of a local heat drain on electrode performance;

▷ a simple branching vessel in the implant volume, emphasizing the local effect of a larger vessel density on the temperature distribution;

▷ two complex counter-current vascular trees in the implant region, illustrating realistic results that may be obtained with the MECS IHT system.

The finite difference grids used in the simulations of the single vessel and simple vascular network situation had a size of $25 \times 25 \times 40$ voxels, the voxels have a size of 2 mm in each direction. Tests run at higher spatial resolutions showed equal results. The complex vascular tree simulations had a 1 mm resolution, leading to a grid of $50 \times 50 \times 80$ voxels.

No vasculature

For comparison, a homogeneous anatomy containing no vascular structures and a $1, 2, 3$ or 4 electrodes per active section implant was modelled, in the non-perfused, muscle equivalent $k = 0.6 \mathrm{Wm}^{-1}\mathrm{K}^{-1}$ situation, the $k = 1.2 \mathrm{Wm}^{-1}\mathrm{K}^{-1}$ effective thermal conductivity situation and with a number of different non-zero heat-sink terms corresponding to perfusions of $10, 20$ and $40 \mathrm{ml}(100\mathrm{g})^{-1}\mathrm{min}^{-1}$ in combination with $k = 0.6 \mathrm{Wm}^{-1}\mathrm{K}^{-1}$.

Single vessel anatomies

In order to investigate the effect of a single passing vessel on the performance of the MECS IHT system we have used the previously described 7-segment implant geometry and added a straight vessel with an inner diameter of 2 mm with a mean blood velocity of $10 \mathrm{~cm\,s}^{-1}$ ($0.3 \mathrm{ml\,s}^{-1}$) (figure 7.2). The Nusselt number used was 3.66 and the specific heat was $4000 \mathrm{~J\,kg}^{-1}\mathrm{~K}^{-1}$, giving a theoretical thermal equilibration length of 1 m, which is large compared to the heated volume (Crezee and Lagendijk, 1992). These material property values were also used in the other simulations containing vasculature.

The properties of the bulk of the volume were first chosen to mimic non-perfused muscle tissue with the thermal conductivity at $k = 0.6\,\mathrm{Wm^{-1}K^{-1}}$. The vessel structure was shifted through the volume from $Z = 0$ mm to $Z = 25$ mm, in order to assess the effect of different vessel orientations and positions with respect to the implant. The position $Z = 0$ is located at the centre of the implant.

As a check on the non-perfused $k = 0.6\,\mathrm{Wm^{-1}K^{-1}}$ calculations, we have performed simulations at $k = 1.2\,\mathrm{Wm^{-1}K^{-1}}$ and with a number of different non-zero heat-sink terms corresponding to perfusions of $10, 20$ and $40\,\mathrm{ml(100g)^{-1}min^{-1}}$. In these simulations, only a single vessel position within the implant was investigated.

Simple branching vessel anatomy

A bifurcation was introduced in the vessels inside the treatment volume as a typical clinical example. In this way, a vessel tree resembling a fork was created. The tree is positioned somewhat off-centre perpendicular to the long axis of the implant (see figure 7.7). The entry vessel has a diameter of 2.5 mm (mean blood velocity of $10\ \mathrm{cm\,s^{-1}}$) and the two vessels after the bifurcation have a diameter of 2 mm. The thermal conductivity of the bulk of the volume was chosen at $k = 0.6\,\mathrm{Wm^{-1}K^{-1}}$.

Complex counter current vascular tree

The previously mentioned vascular structures all pass through the implant volume without coming in thermal equilibrium with the heated tissue. They pass the volume and can not be considered as perfusing the volume. The perfusion of the implant volume was first assumed to be zero taken into account by $k = 0.6\,\mathrm{Wm^{-1}K^{-1}}$. Simulations at $k = 1.2\,\mathrm{Wm^{-1}K^{-1}}$ and with a number of different non-zero heat-sink terms corresponding to perfusions of $10, 20$ and $40\,\mathrm{ml(100g)^{-1}min^{-1}}$ have been performed to investigate the influence of small vessel vasculature. To model a real vascular tree which perfuses the volume considered two complex counter-current trees were constructed, one with a quite homogeneous vascular structure and one with a more inhomogeneous vascular tree. These examples illustrate the feasibility of modelling several generations of vessels in a treatment simulation setting. Van Leeuwen et al. (1996) describe the construction and validation of this type of tree geometry.

In these cases, in order to be able to accurately model smaller vessels, the finite difference model's resolution was increased by a factor of two in the three space dimensions, making the voxel dimensions 1 mm $\times$ 1 mm $\times$ 1 mm. Only a small

number of these simulations were run. With the present thermal model, not optimized for computational speed, it takes about four days on a SGI-R4400 machine to reach a stationary situation.

The vascular trees used for the complex tree simulations were based upon the fork-like tree structure used in the simple-vessel simulations. With the simple fork-like tree as starting point an extensive tree was generated with over 350 vessel branches of the highest generation (Van Leeuwen et al., (in preparation). The termination points of these vessels were uniformly distributed over the volume, yielding a homogeneous tissue perfusion. Of this extensive tree the vessel branches belonging to the last generation were removed for computational reasons. The remaining tree spanned 5 vessel generations, the number of terminating vessel branches being just over one hundred (see figure 7.9). A venous tree, roughly counter current to the arterial tree, was constructed using the same procedure of building an extensive tree and removing the vessel branches in the last generation.

All the segments in the venous tree were classified according to vessel generation using a centripetal ordering scheme (cd. Popel (1987)). This tree is qualitatively the same as the arterial tree while being completely contained within the modelled volume, which facilitated the classification. Analysis of the classified network learned that for consecutive generations the ratio between the numbers of vessel branches as well as the ratio's between the average branch lengths and average branch diameters were approximately constant throughout the network. On average the number of vessel branches of a generation decreased by a factor 3.2 for every new generation of larger vessels. For consecutive generations the ratio between the average branch lengths was 1.2, whereas the branch diameter increased by a factor 1.4 going up in the tree. This last value is partly a result of the implementation of Murray's principle, which states that the flow is proportional to the cube of the vessel diameter, and is strongly correlated with the ratio between the numbers of branches in consecutive generations (3.2) (Murray, 1926).

The blood inflow in the arterial tree was chosen so as to have a volumetric perfusion in the tissue volume of $5\,\mathrm{ml}(100\mathrm{g})^{-1}\mathrm{min}^{-1}$. The diameter of the venous and arterial root segments was 2.1 mm, the mean velocity just over $1\,\mathrm{cm\,s}^{-1}$. The diameter of the incoming arterial vessel was 2.7 mm, that of the vein (with half the volume flow) 2.1 mm. The flow velocities were $5.8\,\mathrm{cm\,s}^{-1}$ and $4.7\,\mathrm{cm\,s}^{-1}$ respectively. The average diameter of the terminal branches in both trees was 0.4 mm. The density of the terminal branches was about $0.45\,\mathrm{cm}^{-2}$.

Figure 7.10 shows a similar set up now simulating a heterogeneous perfusion (upper half of the implant $5\,\mathrm{ml}(100\mathrm{g})^{-1}\mathrm{min}^{-1}$, lower half $1.25\,\mathrm{ml}(100\mathrm{g})^{-1}\mathrm{min}^{-1}$). The

heterogeneous perfusion was obtained by constructing the vascular tree using different numbers of termination points in the upper and lower half of the volume; in the lower half of the volume just a quarter of the termination points in the upper half was used.

7.2.3   Evaluation of results

The temperature distributions resulting from all simulations were visualised using the AVS data visualisation system. Using specialised software the cumulative temperature-volume histogram (CTVH) was constructed for a volume of interest (VOI) identical to the convex hull of the active sections of the implant (Van der Koijk et al., 1996). To study the effect of a shift of the vessel geometry, the $T_{10} - T_{90}$ was plotted against the vessel shift in the cases where that was the only difference between simulations, giving an impression of the influence of the vessel position on the homogeneity of the temperature distribution.

7.3   Results

No vessels

The cumulative temperature/volume histogram (figure 7.1) of the simulations in the homogeneous volume without vasculature show that the improvement of the temperature distribution is small when more than two electrodes per segment are used. The inhomogeneity in the temperature distribution is mainly caused by the conductive transport of heat from the implant volume to the boundaries. As expected an enhanced effective thermal conductivity does not change the temperature profile; only the electrode power levels increase (Lagendijk, 1990b). A nonzero heat sink term makes the temperature gradients near the electrodes steeper, shifting the histogram leftwards to lower temperatures.

Single vessel anatomies

There were two sets of simulations in this group. In both series of calculations, a single non-equilibrated vessel with a diameter of 2 mm was stepped through the volume.

The results for the 'perpendicular' vessel, which was oriented as shown in figure 7.2, are summarised in the $T_{10} - T_{90}$ versus vertical shift graph shown in figure 7.3. From the figure, it is clear that the temperature control fails only in the case of
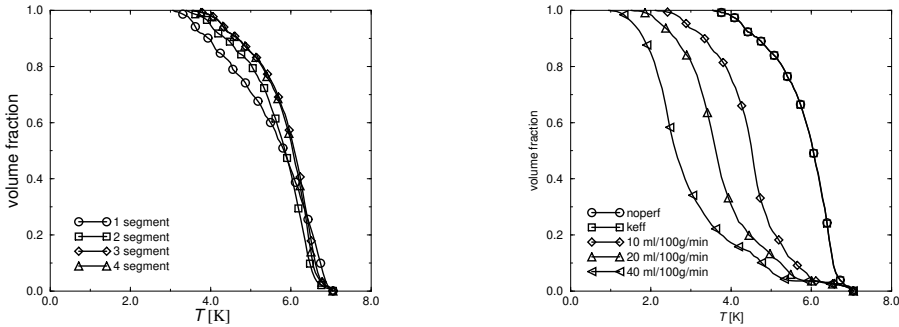
Figure 7.1: Cumulative temperature/volume histogram of the simulations in the homogeneous volume without vasculature. To the left, the CTVH's of four simulations with varying longitudinal segmentation and a k_{eff} of $0.6\,Wm^{-1}K^{-1}$ is shown. To the right, an implant with four electrodes per active section was simulated in a homogeneous tissue environment with varying values of heat conductivity and a non-zero heat sink term.

unsegmented electrodes when the vessel is positioned near the top of the implant. The segmented electrodes do not suffer from this problem, because they can *locally* adjust to the demand for heat.

A slightly different situation occurs when the vessel is oriented obliquely ($60°$ with the implant axis). This configuration is sketched in figure 7.4. The $T_{10} - T_{90}$ versus vessel shift (The Z-component of the shift is used in the figure) graph is shown in figure 7.5. The $T_{10} - T_{90}$ is less dependent on the shift in these simulations; the heat drain effect of the vessel is not concentrated at one side of the implant but more evenly distributed along the path of the electrodes.

In figure 7.6 the CTVH's from a set of calculations with varying tissue thermal properties is displayed. In these simulations we were interested in the inner vessel wall temperatures within the VOI. The minimum inner vessel wall temperature represents the minimum tissue temperature in case of infiltrative tumour growth. Due to the small volume heated and the large vessel diameter no significant equilibration occurs. In table 7.1 the calculated minimum temperatures in the convex hull of the implant are shown for various choices of the thermal parameters with the vessel at $Z = 1$ cm. When increasing the effective heat conductivity from $k = 0.6$ to $1.2\,Wm^{-1}K^{-1}$ the inner vessel wall temperature increases from 1.3 K to 2.2 K
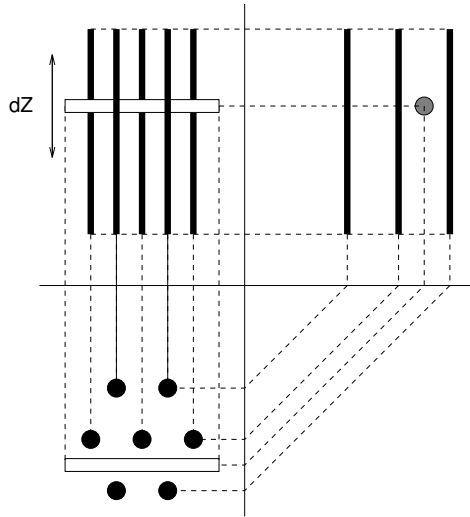
Figure 7.2: Orientation of the vessel with respect to the implant in the first series of single-vessel calculations. American projection. Z = 0 is at the centre of the implant.
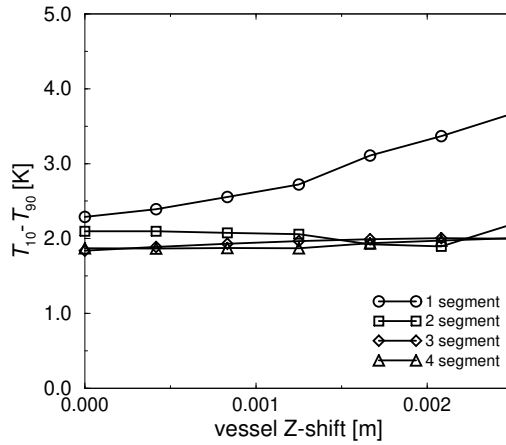

Figure 7.3: $T_{10} - T_{90}$ versus vessel shift; vessel is in plane perpendicular to long axis of implant and shifting from centre outwards
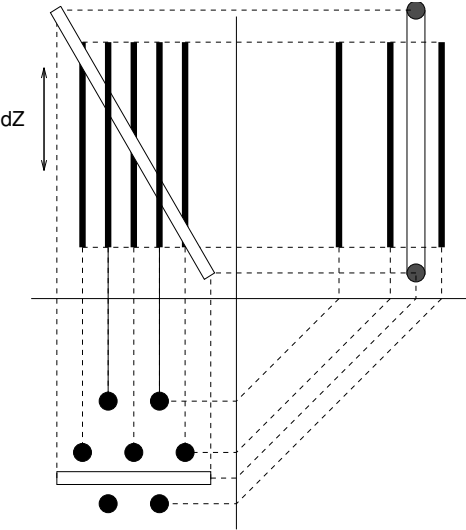
Figure 7.4: Orientation of the vessel with respect to the implant in the second series of single-vessel calculations. American projection.
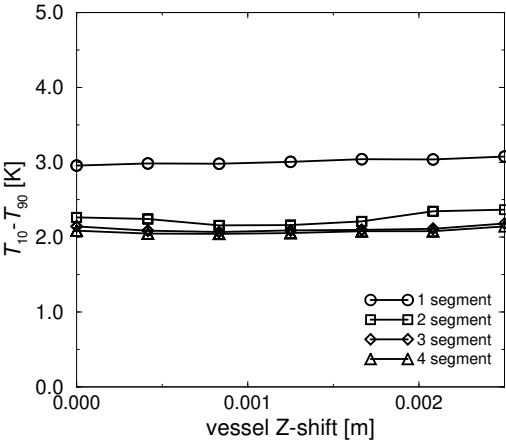

Figure 7.5: $T_{10}-T_{90}$ versus vessel shift; vessel is obliquely oriented in plane parallel to long axis of implant and shifting from central position outwards
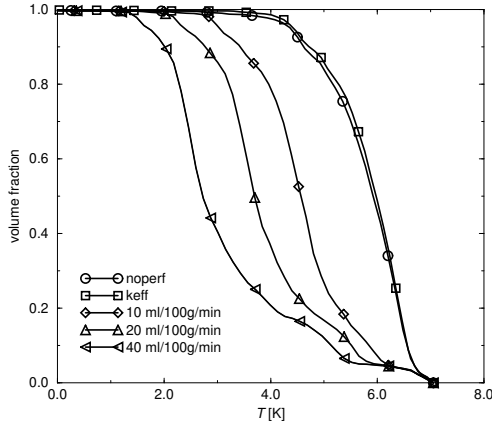
Figure 7.6: CTVH's for four-segment implant with a single non-equilibrated vessel. Several different thermal environments. The vessel was in the $Z = 1$ cm plane perpendicular to the long axis of the implant.

due to the increased ratio between the heat resistance in the vessel and in the surrounding tissue. As in the no-vessel case the introduction of a heat sink term makes the temperature gradients near the electrodes become steeper, shifting the histogram leftwards to lower temperatures. Vessel wall temperatures are thus affected by the introduction of a heatsink through the general decrease of surrounding tissue temperature.

Table 7.1: Minimum temperature in convex hull corresponding to data in figure 7.6. Single vessel, diameter 2 mm. This is also the minimum inner vessel wall temperature in the VOI.

k_{eff}	$[Wm^{-1}K^{-1}]$	0.6	1.2	0.6	0.6	0.6
W_b	$[ml(100g)^{-1}min^{-1}]$	0	0	10	20	40
T_{min}	$[K]$	1.3	2.2	1.0	0.8	0.6

Simple branching vessel anatomy

A simple vascular tree with one affluent and two effluent vessels was used. Three situations were investigated. The first one had no individual control of the electrodes (one per catheter). All electrodes carried the same current, which was chosen with the objective of getting the outer hull of the implant at about 4 K above the baseline temperature. This simulation shows significant overheating in the core of the implant. In the second and third simulation the electrodes were individually controlled, which effectively limits overheating in the implant. Here, the longitudinal control was varied by modelling respectively one and four electrodes per catheter. The results are shown in three iso-temperature surface renditions and three iso-T contour images in a plane containing the central axis of the implant (see figure 7.7). The cumulative temperature-volume histograms for four different electrode segmentations is shown in figure 7.8.

Complex counter current vascular tree

The most realistic simulations contained a total of about 600 vessel segments (3 meters of vessel track) in a volume of about 70 cubic centimetres. The implant, which has a volume of about 40 cc, was embedded in the vessel trees. The trees used here almost reach thermal equilibrium at the chosen values of blood flow and diameter (Van Leeuwen et al., (in preparation).

The iso-temperature images of the homogeneously and inhomogeneously perfused modelled implant are shown in figures 7.9 and 7.10.

The cumulative temperature-volume histograms for the mono and triple electrode segmentation in the homogeneously and heterogeneously perfused situation is shown in figure 7.11.

In the homogeneously perfused case the standard deviation of the 21 electrode currents was $36 \cdot 10^{-3}$ A; in the heterogeneously perfused case the standard deviation of the electrode currents was $45 \cdot 10^{-3}$ A. The mean of the moduli of the electrode currents was $62 \cdot 10^{-3}$ A in the homogeneous case and $53 \cdot 10^{-3}$ A in the heterogeneous case. Note that the power deposition near the electrodes is linearly related to the square of the electrode currents and will vary even more. This illustrates that the spatial control of the MECS system is used more intensively in the heterogenously perfused case. The temperature distribution in the homogeneously perfused anatomy is remarkably smooth with temperature heterogeneity mainly located near the larger vessels.
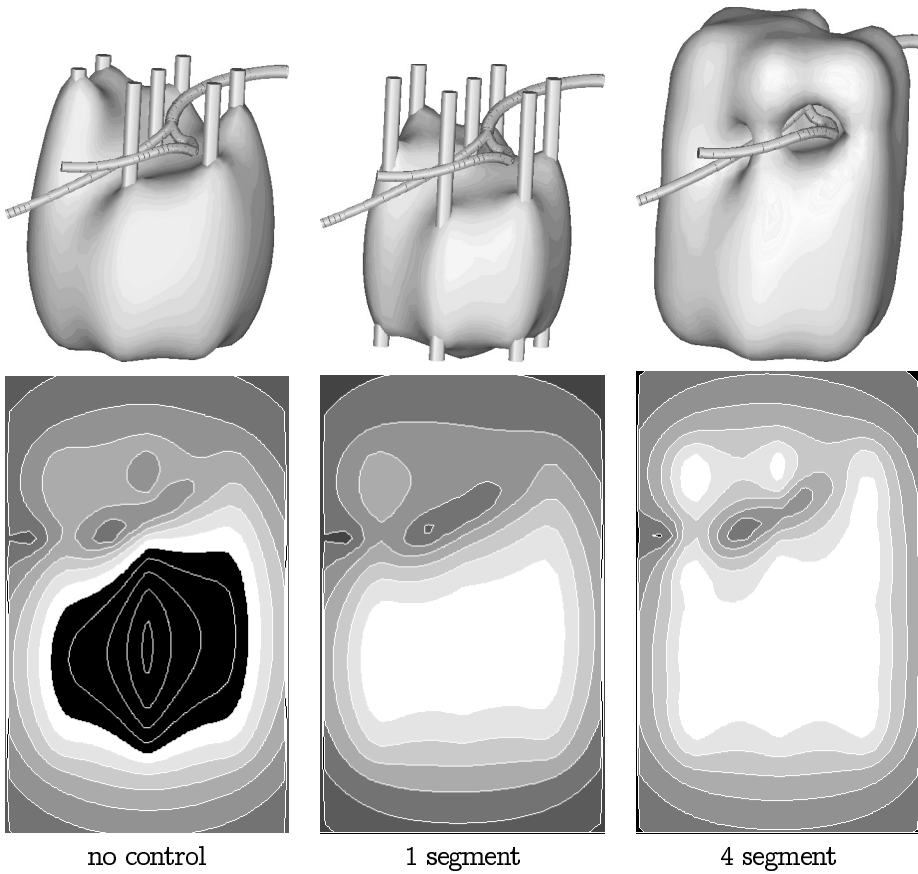
no control   1 segment   4 segment

Figure 7.7: Iso-temperature surfaces at $\Delta T = 4$ K and iso-contours in a plane through the central axis of the implant containing the fork-like tree vascular structure described in the text. The brightest shade of white represents the iso-segment with a maximum temperature of 7 K. Levels are 1 K apart. The black central area in the no-control iso-T contour image is overheated.
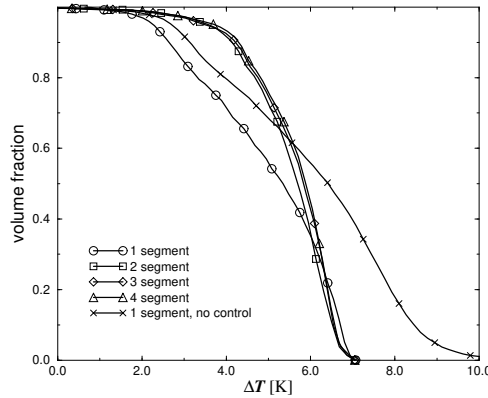
Figure 7.8: Cumulative temperature/volume histogram for the volume of interest in the implant containing the fork-like tree vascular shown in figure 7.7.

7.4 Discussion

In accordance with the results for 2D discrete vessel anatomies heated with a SFUS technique as given by Lagendijk et al. (1994a), the homogeneous anatomies with a single vessel or a simple vessel bifurcation show clearly (see figure 7.7) that in the case with 3D spatial control the influence of the vessel is restricted to the direct surroundings of the vessel. In case of 2D control (no control along the catheter) the influence of the vessel extends further and large parts of the target volume are underdosed. In case of increased effective thermal conductivity, due to the increased ratio between heat resistance in the vessel and in the surrounding tissue the vessel wall temperature rises and the underdosage is minimized (Crezee and Lagendijk, 1990). In the case with the single large vessel in a heat sink environment the temperature peaks around the electrodes producing a longer 'tail' in the cumulative histogram, shifting the CTVH's towards lower temperatures. This is in accordance with the results published in literature (Strohbehn, 1983; Strohbehn et al., 1982; Mechling and Strohbehn, 1986; DeFord et al., 1991; Crezee et al., 1991). The longer tail may be compensated for by increasing the control temperatures. A relatively small fraction of the treatment volume will then be exposed to temperatures exceeding the goal temperature. To obtain 3D control extensive temperature information is needed; these simulations (figure 7.7) illustrate the
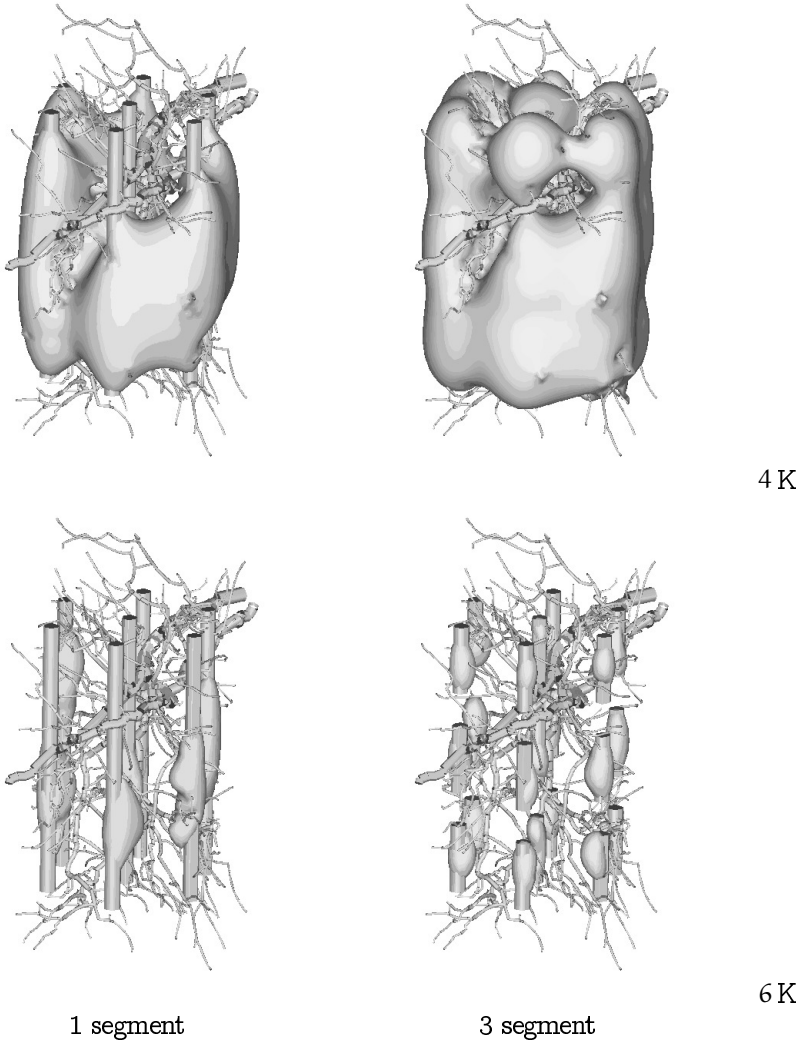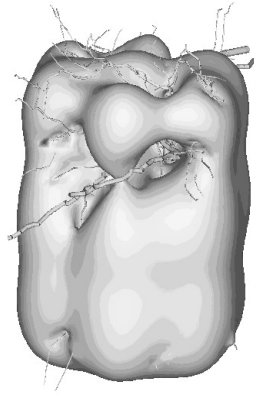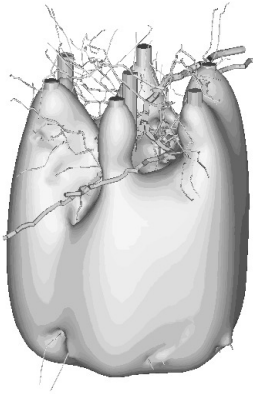
4 K

6 K

1 segment   3 segment

Figure 7.9: Iso-temperature surfaces at $\Delta T = 4$ K and $\Delta T = 6$ K from the complex vessel tree simulations with a homogeneous volume perfusion described in the text (section 7.2.2).

4 K

6 K

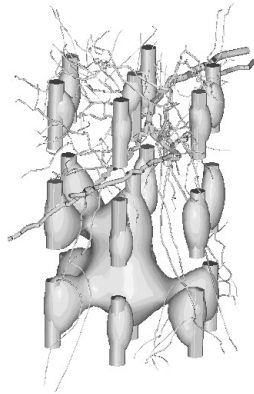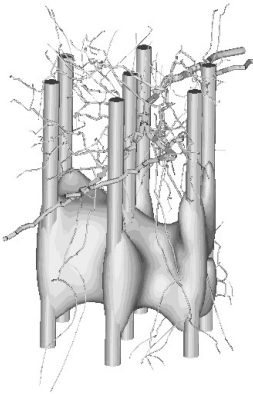1 segment   3 segment

Figure 7.10: Iso-temperature surfaces at $\Delta T = 4$ K and $\Delta T = 6$ K from the complex vessel tree simulations with an *inhomogeneous* volume perfusion described in the text.
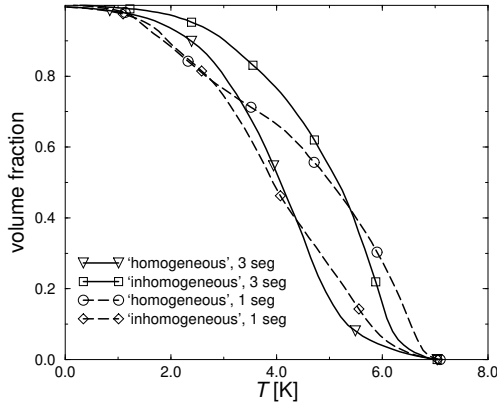
Figure 7.11: Cumulative temperature/volume histogram for the volume of interest in the implant containing the complex vascular tree anatomies. Four tracks are shown: two for the 'homogeneous' vascular anatomy, two for the 'inhomogeneous' vascular anatomy. The applicators contains either one or three segments.

importance of feedback control from the thermometry inside the catheters. The simulation with no individual control of the electrodes shows a severe overheating of the central volume and underdosage near the vasculature.

The most striking simulations are the ones with an anatomy with complete vessel networks simulating tissue perfusion effects. The vessel network is intended to simulate all blood flow related heat transfer, including the heat-sink behaviour. To accurately describe the thermal influence of the very small vasculature a slight increase of the effective thermal conductivity is still considered (Zhu and Weinbaum, 1995). The addition of such an effective thermal conductivity will lower the equilibration lengths and increase the vessel wall temperatures (Crezee and Lagendijk, 1990).

Again, important temperature heterogeneity occurs in the 2D-power control situations; with three-dimensional SAR control temperature heterogeneity is limited to the volume near the larger vessels. The use of the low inner wall temperatures in the analysis produces a slightly exaggerated impression of the temperature heterogeneity in the volume of interest. In the simulation, maximum tissue temperatures were set at $44°$C (7 K above baseline). Normalization of the temperatures at T_{90}

would give a better impression of the improvement of the temperature distribution with spatial control; the main effect of better spatial control is a steeper gradient in the temperature volume histograms (figure 7.11).

The simulations show (figure 7.8) that the minimum sensible length of the individual controllable electrodes is in the order of the catheter spacing. As also shown in Van der Koijk et al. (1996) (chapter 6), using shorter electrodes does not notably improve the temperature distributions in well-positioned implants. Temperature control improves dramatically when going from a single to two segments; further segmentation has less effect. To further improve the temperature distributions the spacing between the catheters, 15 mm in the simulations, may be decreased, which would improve the lateral SAR control. In view of the scale of the tissue inhomogeneities (about a centimetre), it makes no sense to increase the lateral spacing between the implant tracks very much; this will reduce power control in the lateral direction.

Various criteria have been proposed to assess the uniformity of clinical temperature/thermal dose distributions; the cumulative temperature-volume histogram and its parameters T_{50} and T_{90} are popular because they can be derived from the sampled clinical temperature data (Ryan et al., 1994; Stea et al., 1994). Other criteria include the minimum tumour temperature and the percentage of tumour volume above a target temperature, e.g. the HEP rating (Shimm et al., 1990; Paulsen et al., 1984; Strohbehn, 1994). The cumulative temperature/volume histograms used as a primary means of evaluating temperature distributions in a target volume in this chapter were constructed from the calculated temperatures of *all* voxels in the simulation target volume at a stationary temperature. They are not directly comparable to CTVH's obtained from clinical measurement; see the remarks at page 91. In simulations every volume element is accounted for and extremes in the temperature distributions will not be missed. This implies that the CTVH's from simulations will generally contain more extreme values, consistent with the statement that the use of more thermometry sensors in a clinical treatment results in worse CTVH's (Corry et al., 1988).

Kapp et al. (1993) achieved a $T_{10} - T_{90}$ of 3°C and a T_{90} of 40.7°C in anal carcinoma treated with hot water tubes, a system with reasonable longitudinal control. Results from interstitial systems without longitudinal control, similar to our single electrodes, yield higher values of $T_{10} - T_{90}$. For example, using microwave antennas in brain, Seegenschmiedt (1993) found a $T_{10} - T_{90} = 3.4$°C at $T_{90} = 39.8$°C. In the prostate, using an RF system, Prionas et al. (1994) obtained $T_{10} - T_{90} = 4.5$°C with $T_{90} = 39.6$°C. Ryan *et al.* also included temperature data from within the

Table 7.2: Relative heterogeneity corresponding to data in figures 7.9 and 7.10. Complex vascular tree. In all simulations: $T_{core} = 0\,K$.

	one segment			three segments		
perfusion	T_{90} [K]	$T_{10} - T_{90}$ [K]	HC	T_{90} [K]	$T_{10} - T_{90}$ [K]	HC
homogeneous	1.9	3.8	2.0	2.3	3.0	1.3
heterogeneous	1.8	4.7	2.6	3.0	3.1	1.0

applicators and obtained a $T_{10} - T_{90}$ of about $8°C$ at $T_{90} = 40.8°C$ using microwave antennas in the brain (Ryan et al., 1994).

We introduce an indicator for the T-heterogeneity in the implant relative to the T_{90} achieved, the dimensionless heterogeneity coefficient $HC = (T_{10} - T_{90})/(T_{90} - T_{core})$. The results of the homogeneous perfusion complex tree simulation show that HC decreases from 2.0 to 1.3 when the single segment electrode is replaced by a three segment one. The improvement is even more striking for heterogeneous perfusion where HC reduces from 2.6 to 1.0 (see table 7.2). The results derived from literature data are in the same range and show a similar tendency of improving for systems with longitudinal control, from HC between 1.2 and 2.1 to $HC = 0.8$ (see table 7.3).

Table 7.3: Relative heterogeneity corresponding to data in literature. At left without, at right with longitudinal control. $T_{core} = 37°C$

	no long. control			hot water		
reference	$T_{90} - T_{core}$ [K]	$T_{10} - T_{90}$ [K]	HC	$T_{90} - T_{core}$ [K]	$T_{10} - T_{90}$ [K]	HC
Seegenschmiedt (1993)	2.8	3.4	1.2	-	-	-
Kapp et al. (1993)	-	-	-	3.7	3.0	0.8
Ryan et al. (1994)	3.8	8.0	2.1	-	-	-
Prionas et al. (1994)	2.6	4.5	1.7	-	-	-

In clinical practice, inhomogeneity of the patient is determined by both the vasculature present in the tissue, which is the subject of this chapter, and the presence of regions of contrasting material properties (tissue inhomogeneity). The influence of tissue inhomogeneity on the behaviour of the MECS IHT system is investigated in the previous chapter. That study showed that using 2D controlled systems in fat-tumour anatomies may result in HC values above five, worse than the temperature inhomogeneities encountered in this study on the influence of vasculature.

The conclusions drawn from the results of the presented simulations pertain to the capacities of the MECS IHT system. This system, which controls 64 independent electrodes, is designed to provide the desired 3D control. Several refinements have been proposed in literature to improve other IHT systems to incorporate similar 3D power control. Hot source or conductive techniques have been developed; hot water tube systems provide intrinsic spatial control provided that the thermal resistance of the needle wall is low when compared to the thermal resistance of the surrounding tissue (Hand et al., 1991). Another technique with intrinsic spatial control is the application of thermal seeds with Curie point power control (Van Wieringen et al., 1996b; Cetas et al., 1994). Advantages of microwave techniques include compatibility with plastic catheters and good SAR penetration depth (Stauffer, 1990; Coughlin et al., 1992; Seegenschmiedt, 1993; Sneed et al., 1992; Ryan et al., 1994). Unfortunately, problems arise when attempts are made to upgrade the 2D-controlled to 3D-controlled systems. A technique which uses multiple, not individually controlled, microwave nodes to improve longitudinal SAR uniformity is described by Lee et al. (1986). A technique employing segmented ultrasound transducers is currently being developed (Hynynen, 1992; Diederich and Hynynen, 1993; Diederich et al., 1996). A segmented electrode, local current field (LCF) technique was developed at Stanford (Prionas et al., 1992).

7.5 Conclusion

Simulations including the effect of simple large vessel structures and complex vascular networks (both homogeneous and heterogeneous perfusion) demonstrate the great effect of blood flow on the temperature distributions obtained. It is concluded that the spatial SAR control of the MECS IHT system, combined with the temperature feedback available, is essential for optimizing the temperature uniformity.

Even if over-dosage in large parts of the tumour is acceptable the spatial control is needed to avoid overheating of the normal tissue in or near the target volume and to make the thermal dose distributions controllable by the clinician. The optimal length of the electrodes is in the order of the catheter spacing. The use of shorter electrodes does not notably improve the temperature homogeneity.

Further research is needed to investigate the parameters which are important for optimal temperature control in patients treated with the MECS IHT system; the parameters of interest include location, spacing, length and phase of RF electrodes in relation to the locations of large vessels, clusters of large vessels (high vessel

density), the dielectric anatomy and the effective thermal conductivity anatomy. Current research is aimed at obtaining practical clinical guidelines for optimal system settings in individual patients.

Summary and conclusion

The framework

Using heat for the treatment of malignant tumours is becoming standard treatment. However, it has proven to be far from easy to produce controlled temperature distributions in living tissue. The development of elaborate diagnostic scanning systems and the availability of considerable computational power has opened the way to direct physical modeling of the absorbed power distribution and temperature field in the tissue of the patient.

The work described in this thesis was focused on the preparation of the clinical introduction of a specific interstitial hyperthermia system, the Multi-Electrode Current Source Interstitial HyperThermia (MECS-IHT) system. In order to be able to plan a treatment with this system, and also to investigate the physical properties of the proposed treatment method, a number of computer models have been designed, implemented and tested and special procedures for the simulation of actual treatments were devised.

The MECS-IHT system.

The main physical problem of local hyperthermia is the strong spatial variation of the removal of heat from the treatment volume by blood flow.[1]

Local hyperthermia systems work by administering heat to the target volume and its immediate surroundings. In order to create an acceptable temperature distribution in the target volume the spatial distribution of the heat deposition must be adapted to the heat removal pattern in the tissue.

In 1991, Lagendijk and Visser started the development of a new capacitively coupled interstitial hyperthermia system, addressing this fundamental problem in local hyperthermia technique. The system devised consists of numerous metallic electrodes connected to high-frequency power sources, inserted in plastic catheters.

---

1. In this context, 'blood flow' includes the influence of discrete blood vessels and micro-circulation.

The coupling between the power sources and the tissue is dominated by the capacity between the tissue and the electrode: the dielectric catheter wall. Thus, relative independence of the electrical properties of the surrounding tissue was attained. It proved to be possible to place several independent electrodes in a single catheter. In this way, the heat deposition along the catheter track can be adjusted, allowing finer spatial SAR control than previously available.

A very strong point of the MECS system is that it incorporates extensive thermometry in the target volume. The temperature data acquired in the applicators can be used for real time feedback control of the power deposition of the system. Chapter 2 describes the MECS-IHT system with emphasis on the impedance matching.

The planning system

In a given patient situation a number of choices must be made to determine the parameters of the treatment. For example, the placement of the heat sources and their relative phases must be defined.

The process of selecting optimal parameters for the treatment is called treatment planning. The input for the planning procedure is a set of data concerning the patient: volume scans of the affected tissue and surroundings, vascular structures in and near the target volume, the target volume definition, geometrical constraints, etc.

The results of the planning should be a recipe for the implantation of the catheters and the electrode configuration and detailed information on the temperature distribution which can be expected.

The treatment planning is implemented as an iterative process. Once a certain choice is made for the treatment parameters, physical models of the heating system and the heat transport in the implant are used to asses the given setup. If the assessment of the setup is unfavourable, certain parameters can be changed (mostly 'by hand') and the assessment procedure is restarted. Parameters of the setup *can* be changed automatically in the treatment planning system, most notably the intensity of the heat sources. This opens the way to a realistic simulation of the dynamics of the treatment system.

Once a treatment is set up in a patient, reconstruction of the actual relative position of the relevant structures should be used for further treatment simulation.

The treatment planning system developed in the Utrecht research group consists of a number of modules:

▷   calculation of the power deposition in tissue;

▷   thermal model incorporating discrete vasculature;

▷   feedback controller used to optimise electrode settings;

▷   software for analysing temperature distributions;

▷   vessel reconstruction software;

▷   implant planning software;

▷   visualisation of the temperature distributions in tissue and along vasculature;

▷   visualisation of the implant setup.

A use of the planning system that is not directly of benefit for a specific patient is the investigation of general physical properties of the heating technique. In this way, the planning system is used to gain better understanding of the interaction between the treatment (power deposition) system and the patient (heat transport) system.

The electrical properties of the applicator

Multi electrode current source interstitial hyperthermia (MECS-IHT) employs individually controlled, 27 MHz radiofrequency electrodes inserted into plastic brachytherapy catheters.

In order to get a firm understanding of the physical behaviour of the electrodes and to verify the current source approximation in the hyperthermia treatment planning system we have investigated (1) the electrical properties of the electrode-catheter-tissue system and (2) the impact of inhomogeneity of the electrical properties of the tissue in the vicinity of the electrodes.

The results validate the use of the ideal current source approximation in the treatment planning SAR model. The models predict the presence of a significant heat source inside the electrode wall when lossy catheter materials are used, producing a conductive heating component in addition to the SAR in the tissue. For a given catheter spacing this conductive component will produce a more heterogeneous temperature distribution. Thus, the use of low-loss catheter materials like polyethylene and Teflon is recommended. In case of efficiency problems with the treatment system a compromise can be struck between a more lossy wall material and a less good penetration depth of the heating.

The thermal properties of the applicator

The thermal influence of self-heating of the catheter was investigated and an analysis of the measurement of temperatures inside the catheter during and after heating was made. Analytical models and a high resolution numerical model were

used for the calculation of steady state and transient distributions, respectively. The model results were compared with experimental data obtained in a muscle equivalent phantom.

The results from these investigations indicate that there is no significant difference between the temperature inside or outside the catheter when using low-loss catheter materials. Self heating in the catheter wall has an adverse effect on the uniformity of the stationary temperature distribution and the reliability of temperature measurement with the internal thermometry. This effect remains within acceptable limits for mildly lossy materials, where there is only a 6% difference between the temperature increase inside and outside when using low-loss Nylon.

Distortion of temperature gradients measured along the catheter was also investigated. Key factors are the thermal conduction across the thermocouple wires and especially the presence of minute layers of air between consecutive layers of the probe. The distortion extends less than two millimeters, which is acceptable.

The simulation results are compatible with measurements in phantoms and show that, if the proper choice of materials is made, the MECS applicator answers to our expectations and that the temperature measurement inside the catheter can be used for direct feedback treatment control.

Anatomical models without discrete vessels

The quality of temperature distributions that can be produced with the MECS-IHT system was investigated using computer models of idealised anatomies. These much idealised anatomical models did not contain discrete vessels. Binary media anatomies, containing media interfaces oriented parallel, perpendicular or oblique with respect to the long axis of the implant represented simple anatomies which *can* be encountered in clinic.

A 7 catheter hexagonal implant geometry with a nearest neighbour distance of 15 mm was used for the investigations. In each interstitial probe between 1 and 4 electrodes with a diameter of 2.1 mm were placed along an 'active section' with a length of 50 mm.

The study showed that even with high contrasts in electrical and thermal conductivity in the implant it remains possible to obtain satisfactory temperature distributions with the MECS system. Due to the 3D spatial control the temperature homogeneity in the implant can be made quite satisfactory, with $T_{10} - T_{90}$ in the order of $2 - 3$ K and a maximum temperature rise of 7 K in the volume. It is important to emphasise that treatment planning must ensure that the placement of the current source electrodes is compatible with the media configuration.

The minimum sensible length of the individual controllable electrodes is in the order of the catheter spacing. Using shorter electrodes does not notably improve the temperature distributions in well-positioned implants. Temperature control improves dramatically when going from a single to two segments; further segmentation has less effect. To further improve the temperature distributions the spacing between the catheters, 15 mm in the simulations, may be decreased, which would improve the lateral SAR control.

Inhomogeneities present in the implant volume lead to inferior temperature distributions if no longitudinal SAR control is available: it is then impossible to devise an electrode configuration compatible with the anatomy. If there is a limited amount of spatial control and the inhomogeneities are of comparable or larger scale, careful planning of the geometrical electrode configuration is essential. The performance of electrodes extending through the interface between media can be compromised. Although the effects seen in the CTVH's in these cases may not be spectacular, there can be significant local deviations from the prescribed temperature, which may have serious consequences for tumour control.

Anatomical models with discrete vessels

Simulations including the effect of simple large vessel structures and complex vascular networks (both homogeneous and heterogeneous perfusion) demonstrate the great effect of blood flow on the temperature distributions obtained. The spatial SAR control of the MECS IHT system, combined with the temperature feedback available, is essential for optimizing the temperature uniformity.

Even if over-dosage in large parts of the tumour is acceptable the spatial control is needed to avoid overheating of the normal tissue in or near the target volume and to make the thermal dose distributions controllable by the clinician. The optimal length of the electrodes is in the order of the catheter spacing. The use of shorter electrodes does not notably improve the temperature homogeneity.

Further research is needed to investigate the parameters which are important for optimal temperature control in patients treated with the MECS IHT system; the parameters of interest include location, spacing, length and phase of RF electrodes in relation to the locations of large vessels, clusters of large vessels (high vessel density), the dielectric anatomy and the effective thermal conductivity anatomy. Current research is aimed at obtaining practical clinical guidelines for optimal system settings in individual patients.

Epilogue

The clinical introduction of the MECS-IHT system is now well on its way. In Rot-

terdam, Utrecht and Amsterdam treatment protocols have been designed which are aimed at treating brain tumours, the prostate and soft-tissues. Present actual treatments with the system are technically successful.

Patient specific treatment planning in hyperthermia is still immature, mainly due to technical problems in the field of data acquisition (vessel reconstructions, dielectric and thermal tissue properties). *In-vivo* and phantom tests of the treatment planning system are currently running. These items are subject of a new project funded by the Dutch Cancer Society (NKB). The planning system, and notably the thermal model, developed during the project has proven to be versatile and powerful. For the first time, it has allowed us to faithfully model the detailed thermal behaviour of complex and realistic vessel networks.

The further development of the planning system and the MECS-IHT system towards full clinical usability is a formidable challenge. A concrete foundation is present.

Samenvatting en conclusie

Algemeen

Bij de bestrijding van kwaadaardige tumoren wordt steeds vaker gebruik gemaakt van behandeling met warmte. Bepaalde tumoren kunnen slecht tegen verwarming: de kankercellen worden gevoeliger voor radioactieve bestraling, zodat daarvan minder nodig is. Er zijn verschillende strategieën om het weefsel op te warmen. De technieken die een tamelijk klein deel van het lichaam verwarmen worden wel met 'lokale hyperthermie' aangeduid. Het is niet eenvoudig de temperatuur van een relatief klein deel van een menselijk lichaam op een gecontroleerde manier te verhogen, terwijl de rest op zijn oorspronkelijke temperatuur blijft. Door verbeterde afbeeldingstechnieken en snellere computers kunnen er nu betrouwbare modellen gemaakt worden van de manier waarop warmte in het weefsel van de patiënt wordt getransporteerd. Daarom is het tegenwoordig mogelijk goed onderzoek te doen aan het gedrag van (voorgestelde) verwarmingstechnieken.

In deze dissertatie wordt voornamelijk ingegaan op de voorbereidingen voor de klinische introductie van een tamelijk nieuw systeem, waarmee warmte 'van binnen uit' in het weefsel wordt gebracht. Dit zogenaamde interstitiële hyperthermie systeem wordt het 'Multi-Electrode Current Source Interstitial HyperThermia'-systeem genoemd, kortweg het MECS-IHT systeem. Om uit te zoeken hoe met dit systeem een goede behandeling kan worden gegeven, wordt onderzocht hoe de verschillende vrijheidsgraden het kunnen worden uitgebuit.

Het MECS-IHT systeem

In 1991 begonnen Jan Lagendijk (in het Academisch ziekenhuis te Utrecht) en Andries Visser (in de Dr. Daniel den Hoed kliniek te Rotterdam) met de ontwikkeling van een nieuw, verbeterd, capacitief gekoppeld interstitieel hyperthermiesysteem. Het grootste probleem bij het verwarmen van kleine weefselvolume's is dat de toegevoegde warmte op een ingewikkelde manier door het bloed wordt afgevoerd. Daardoor is het moeilijk de temperatuur in het hele volume op de gewenste

temperatuur te krijgen en te houden. Door de warmteontwikkeling plaatsafhankelijk te maken en te besturen met behulp van in het weefsel gemeten temperaturen wordt toch een behoorlijk goede controle over de temperatuurverdeling verkregen.

Lagendijk en Visser kozen er voor het probleem van de ruimtelijke sturing van vermogen aan te pakken met een interstitieel systeem[2]: binnen in catheters (dunne buisjes van plastic) die in het weefsel zijn ingebracht worden verschillende elektroden geplaatst. De elektroden worden afzonderlijk aangesloten op hoogfrequente spanningsbronnen. Het vermogen van de elektroden kan afzonderlijk worden geregeld. Het bleek mogelijk om verschillende (tot drie) onafhankelijke elektrodes in één catheter te plaatsen. Hierdoor kan de warmte-afgifte langs de gehele catheter worden gestuurd en ontstaat bij aanwezigheid van voldoende catheters een bruikbare controle over ruimtelijke afgifte van warmte.

Een sterk punt van het MECS-systeem is dat het uitgebreide informatie over de temperatuur in het doelvolume levert. Deze temperatuurdata wordt gebruikt voor directe (onvertraagde) teruggekoppelde sturing en controle van de warmteafgifte van het systeem.

De catheters die door het MECS-IHT systeem worden gebruikt worden ook toegepast voor een techniek die al langer bestaat en brachytherapie heet; daarbij worden er radioactieve bronnen in de buisjes aangebracht.

Het planningsysteem

Het bepalen van de optimale parameters voor een behandeling wordt treatment-planning genoemd. Hiervoor zijn gegevens nodig over de patiënt: ruimtelijke afbeeldingen van het aangetaste weefsel en de omgeving daarvan, de ligging van de bloedvaten in het volume, geometrische eigenschappen van het doelvolume, enzovoort.

De planning levert een behandelplan op: een voorschrift voor het aanbrengen van de catheters en de elektrodes. Zo dient er bijvoorbeeld te worden vastgesteld waar de elektroden moeten worden geplaatst en hoe ze moeten worden aangestuurd. Tevens komt er gedetailleerde informatie over de te verwachten temperatuurverdelingen ter beschikking.

Treatment-planning is in dit geval een iteratief proces. Op basis van ervaring wordt een eerste behandelplan opgezet. Dit plan wordt gebruikt om een fysisch model van

---

2. Het woord interstitiëel duidt er op dat er 'vreemd' materiaal in het weefsel (de interstitiële ruimte) wordt aangebracht. In het geval van het MECS IHT systeem worden er buisjes in het weefsel gebracht: het systeem is dus invasief.

de behandeling te maken, waarna met behulp van computerprogramma's wordt geschat wat het resultaat van de behandeling zou zijn. Als de resultaten van deze simulaties niet bevredigend zijn wordt bekeken wat er verbeterd zou kunnen worden. Na het aanbrengen van wijzigingen wordt een nieuwe schatting van het systeemgedrag gemaakt. Dat gaat zo door tot men tevreden is of men het opgeeft.

Enkele parameters kunnen automatisch worden gemanipuleerd. De belangrijkste daarvan is (op dit moment) de warmteproductie van afzonderlijke elektroden. Hierdoor wordt het in principe mogelijk een realistisch model van het dynamisch gedrag van het behandelingssysteem te maken.

Als alle voorbereidingen voor de behandeling van een patiënt zijn voltooid moet een reconstructie van de *echte* ligging van de catheters in het volume worden gebruikt in verdere simulatie van de behandeling. Deze informatie moet ook gebruikt worden bij het vastleggen van het verloop van de behandeling.

Het treatment-planning systeem dat wij de afgelopen jaren hebben ontwikkeld omvat de volgende delen:

▷ een SAR model voor de berekening van de warmtedepositie in weefsel;
▷ een thermisch model voor de berekening van de temperatuurverdeling in weefsel met bloedvaten;
▷ een programma dat een teruggekoppelde sturing van de elektroden realiseert;
▷ programmatuur voor het beoordelen van temperatuurverdelingen;
▷ programmatuur voor het reconstrueren van netwerken van bloedvaten;
▷ programmatuur voor het samenstellen van implantaten;
▷ programmatuur voor het visualiseren van temperatuurverdelingen in weefselvolumina en langs bloedvaten;
▷ programmatuur voor het visualiseren van implantaten en andere structuren in het weefsel.

Het planningsysteem is niet alleen ontwikkeld om specifieke behandelplannen voor patiënten te kunnen produceren. Andere toepassingen zijn het vergelijken van verschillende verwarmingstechnieken en het onderzoek aan de mechanismen die een rol spelen bij de interactie tussen verwarmingssystemen en het warmtetransport in de patiënt.

De elektrische eigenschappen van de applicator

Om een goed begrip te krijgen van het fysisch gedrag van de elektroden en in het bijzonder om de stroombronbenadering die in het SAR model wordt gebruikt te onderzoeken zijn de elektrische eigenschappen van het elektrode-weefsel systeem

onderzocht en is er gekeken naar de invloed van inhomogeniteit van de elektrische materiaaleigenschappen in de buurt van de elektroden.

Het resultaat van dit onderzoek was dat het gebruik van de stroombronbenadering in het SAR model verdedigbaar is. De resultaten van berekeningen op hoge resolutie laten zien dat er een extra warmtebron in de applicator aanwezig is wanneer gebruik wordt gemaakt van wandmateriaal dat belangrijke elektrische verliezen vertoont. Hierdoor ontstaat een (extra) conductieve bijdrage aan de temperatuurgradiënt bij de elektrode. Het gevolg van zo'n component is dat bij een gegeven afstand tussen de catheters in een implantaat een heterogenere temperatuurverdeling ontstaat. Daarom lijkt het beter weinig-verliesgevende materialen als polyethyleen of Teflon te gebruiken.

De thermische eigenschappen van de applicator

Een goed begrip van de warmtehuishouding binnen de applicator is belangrijk voor de interpretatie van de temperatuurmetingen die tijdens behandelingen plaatsvinden.

De twee mechanismen van belang zijn de opwarming van de catheterwand als die (grote) elektrische verliezen vertoont en de warmtegeleiding langs het thermokoppel dat voor de temperatuurmeting wordt gebruikt.

Het onderzoek toont aan dat er geen belangrijk verschil is tussen te temperatuur binnen en buiten de applicator, mits de wand niet te verliesgevend is en de tijds- en ruimtelijke afgeleiden van de temperatuur binnen de perken blijven. De resultaten zijn vergeleken met die van metingen in spier-equivalente fantomen.

Een van de belangrijkste factoren die een rol spelen bij de meting van temperatuurgradiënten langs de catheter is de aanwezigheid van dunne luchtlaagjes in de applicator. Hoe dikker die zijn, hoe groter de rol van de langsgeleiding binnen de catheter wordt, wat nadelig kan zijn.

De temperatuur die in de applicator wordt gemeten geeft een betrouwbare indicatie van de weefseltemperatuur buiten de applicator, en kan gebruikt kan worden voor de sturing van het vermogen van de elektroden.

Anatomische modellen zonder discrete vaten

Het eerste uitgebreide onderzoek aan het gedrag van het MECS-IHT systeem was gericht op de invloed van verschillen in de weefseleigenschappen nabij het implantaat. De tamelijk eenvoudige anatomieën die we hiervoor gebruikten bevatten nog geen bloedvaten. Toch komen er in de kliniek wel anatomische situaties voor die vergelijkbaar zijn met de eenvoudige modellen die we hier gebruikten.

In de berekeningen is gebruik gemaakt van een hexagonaal implantaat met 7 catheters die een naaste-buur afstand van 15 mm hadden. In elke catheter werden 1 tot 4 elektroden met een diameter van 2.1 mm gemodelleerd langs een actieve lengte van 50 mm.

Het is gebleken dat het MECS systeem zelfs bij grote contrasten in de elektrische en thermische eigenschappen een goede temperatuurverdeling kan produceren. Er moet dan wel voldoende aandacht (kunnen) worden geschonken aan de plaatsing van de elektroden en de ligging van de catheters.

Voorts bleek dat de minimale lengte van de elektrodes in de buurt van de naaste-buur afstand kan liggen. Het gebruik van kortere elektrodes levert geen aanwijsbaar betere temperatuurverdelingen op, als de elektroden tenminste verstandig zijn geplaatst. De beheersbaarheid van de temperatuurverdeling verbetert dramatisch wanneer van één op twee segmenten per applicator wordt overgegaan; verdere segmentatie heeft minder effect.

Als er geen sturing van de warmtedepositie mogelijk is, ontstaan er bij inhomogeniteiten in het behandelingsvolume onbruikbare temperatuurverdelingen. Het is dan onmogelijk om een goede elektrodeconfiguratie te ontwerpen. Bij beperkte sturing en wanneer de 'schaal' van de inhomogeniteiten van dezelfde orde wordt als die van de sturing, wordt een zorgvuldig ontwerp van de elektrodeconfiguratie erg belangrijk. Vooral het gedrag van elektroden die door de scheidingsvlakken tussen verschillende weefseltypen steken worden nadelig beïnvloed. Hoewel de effecten die in de temperatuur/volume histogrammen te zien zijn niet spectaculair hoeven te zijn kunnen er belangrijke locale afwijkingen in de temperatuurverdeling ontstaan, wat onplezierige gevolgen voor het resultaat van de behandeling kan hebben.

Anatomische modellen met discrete vaten

Het belangrijke effect van de aanwezigheid van discrete bloedvaten op de temperatuurverdeling die bij hyperthermiebehandeling in het weefsel ontstaat is het best te illustreren met behulp van simulaties waarin de effecten van die vaten ook echt gemodelleerd zijn. Wij hebben voor het eerst uitgebreide berekeningen aan de invloed van de aanwezigheid van realistische, ingewikkelde, ruimtelijk inhomogene vatnetwerken bij lokale hyperthermiebehandeling gedaan. Ook uit deze berekeningen bleek dat de ruimtelijkse SAR sturing die het MECS systeem biedt onontbeerlijk is voor het produceren van aanvaardbare temperatuurverdelingen.

Zelfs wanneer oververhitting in grote delen van het behandelingsvolume aanvaardbaar zou zijn is ruimtelijke sturing nog steeds nodig om te voorkomen dat gezond weefsel in de buurt van het doelvolume onnodig beschadigd raakt.

Hoewel er in de loop van dit onderzoek veel duidelijk is geworden over de relatie tussen weefseleigenschappen, de ligging van bloedvaten, de plaatsing van het MECS implantaat en de te verwachten kwaliteit van de temperatuurverdeling is er nog wel iets te wensen over. Veel onderzoek is nog nodig om beter te weten te komen hoe het bijvoorbeeld precies met de thermische en elektrische weefseleigenschappen zit; hoe de ligging van de bloedvaten samenhangt met de optimale plaatsing van het implantaat (zo die te vinden is); wat de invloed van het dynamische gedrag van de perfusie op de behandeling is, enzovoort.

Op dit moment wordt hard gewerkt aan het opstellen van klinisch bruikbare regels voor de inzet van het MECS systeem, gebruik makend van individuele patiëntinformatie. Het doel van dit alles is uiteindelijk te komen tot goed beheersbare, gecontroleerde locale behandeling met warmte.

Epiloog

De klinische introductie van het MECS-IHT systeem is inmiddels aardig op weg. In Rotterdam, Utrecht en Amsterdam zijn protocollen opgesteld voor de behandeling van hersentumoren, de prostaat en voor weke-delen tumoren. De huidige behandelingen verlopen in technische zin bevredigend. Over de klinische resultaten valt nu nog niet veel te zeggen.

De patiënt-specifieke planning van hyperthermiebehandelingen staat nog steeds in zijn kinderschoenen. Dat komt onder meer door technische problemen op het gebied van de vergaring van informatie over de ligging van bloedvaten en over de elektrische en thermische eigenschappen van het te behandelen weefsel. De kwaliteit van het treatment-planning systeem wordt op dit moment onderzocht in fantomen en in geperfundeerde weefsels. Dit onderzoek maakt deel uit van een nieuw project dat wordt gesteund door de Nederlandse Kankerbestrijding.

Het planningsysteem, en in het bijzonder het thermisch model, dat gedurende het project in de Utrechtse groep is ontwikkeld heeft bewezen dat het veelzijdig en krachtig is. Het bleek mogelijk te zijn het thermische gedrag het MECS-IHT systeem natuurgetrouw na te bootsen in anatomieën met ingewikkelde, realistische netwerken van bloedvaten.

De ontwikkeling van het MECS-IHT systeem en van het hyperthermie planningsysteem naar volwaardige klinische bruikbaarheid is een formidabele uitdaging. Er ligt een stevig fundament.

Dit werk vond plaats in een onderzoeksproject dat werd gefinancierd door de Nederlandse Kankerbestrijding.

List of publications

J.F. van der Koijk, J. Crezee, A.N.T.J. Kotte, G.M.J. van Leeuwen, J.J. Battermann, and J.J.W. Lagendijk. The influence of vasculature on temperature distributions in MECS interstitial hyperthermia: importance of longitudinal control. *International Journal of Hyperthermia*, in press. (This text is the basis of chapter 7 of this thesis.)

J.F. van der Koijk, J. Crezee, and J.J.W. Lagendijk. Thermal properties of capacitively coupled electrodes in interstitial hyperthermia. Submitted to *Physics in Medicine and Bioligy*. (This text is the basis of chapter 5 of this thesis.)

J.F. van der Koijk, J. Crezee, G.M.J. van Leeuwen, J.J. Battermann, and J.J.W. Lagendijk. Dose uniformity in MECS interstitial hyperthermia: the impact of longitudinal control in model anatomies. *Physics in Medicine and Biology*, 41(3):429–444, 1996. (This text is the basis of chapter 6 of this thesis.)

J.F. van der Koijk, J. de Bree, J. Crezee, and J.J.W. Lagendijk. Numerical analysis of capacitively coupled electrodes for interstitial hyperthermia. Submitted to the *International Journal of Hyperthermia*. (This text is the basis of chapter 4 of this thesis.)

J. Crezee, J.F. van der Koijk, R.S.J.P. Kaatee, and J.J.W. Lagendijk. Implications of using thermocouple thermometry in 27 MHz capacitively coupled interstitial hyperthermia. *Physics in Medicine and Biology*, ?(?):in press, 1997.

J. de Bree, A.N.T.J. Kotte, J.F. van der Koijk, and J.J.W. Lagendijk. A 3D treatment planning system for interstitial hyperthermia and brachytherapy. *The British Journal of Radiology*, 1996. (accepted).

J. de Bree, J.F. van der Koijk, and J.J.W. Lagendijk. A 3-D SAR model for current source interstitial hyperthermia. *IEEE Transactions on Biomedical Engineering*, 43(10):1038–1045, 1996.

A.N.T.J. Kotte, J. de Bree, J.F. van der Koijk, and J.J.W. Lagendijk. Thermal model for hyperthermia treatment planning incorporating geometrical vessel description. *The British Journal of Radiology*, 1996. (accepted).

A.N.T.J. Kotte, G.M.J. van Leeuwen, J. de Bree, J.F. van der Koijk, J. Crezee, and J.J.W. Lagendijk. A description of discrete vessel segments in thermal modelling of tissues. *Physics in Medicine and Biology*, 41(5):865–884, May 1996.

J.J.W. Lagendijk, J.F. van der Koijk, A.G. Visser, R.S.J.P. Kaatee, J. Crezee, J. de Bree, A.N.T.J. Kotte, A.P. Kanis, H. Kroeze, P.C. Levendag, and J.J. Battermann. Dose uniformity with the 27 MHz multi-electrode current source interstitial hyperthermia method. In G. Bruggmoser and R.F. Mould, editors, *Brachytherapy review, Proceedings German Brachytherapy Conference Freiburg*, pages 38–44, November 1994.

J.J.W. Lagendijk, A.G. Visser, R.S.J.P. Kaatee, J. Crezee, J.F. van der Koijk, J. de Bree, A.N.T.J. Kotte, A.P. Kanis, H. Kroeze, P.C. Levendag, and J.J. Battermann. Interstitial hyperthermia & treatment planning: the 27 MHz multi-electrode current source method. *Activity International Nucletron-Oldelft Radiotherapy Journal*, (special report 6):83–90, 1995.

G.M.J. van Leeuwen, A.N.T.J. Kotte, J. de Bree, J.F. van der Koijk, J. Crezee, and J.J.W. Lagendijk. Accuracy of geometrical modelling of heat transfer from tissue to blood vessels. *Physics in Medicine and Biology*, (submitted).

A.G. Visser, J.J.W. Lagendijk, R.S.J.P. Kaatee, J. Crezee, J.F. van der Koijk, A.P. Kanis, and J. de Bree. Design of a 27 MHz capacitive-coupling interstitial hyperthermia system. *Medical Physics*, 20(3):914, May/June 1993.

Bibliography

Aronen H.J., Gazit I.E., Louis D.N. et al. Cerebral blood volume maps of gliomas: comparison with tumor grade and histologic findings. *Radiology* (191):42–51, 1994

Bowman H.F., Martin G.T.and Newman W.H., Kumar S., Welch C., Bornstein B. and Herman T.S. Human tumour perfusion measurements during hyperthermia therapy. In E Gerner, ed., *Hyperthermic Oncology*, volume 1, Tucson, Arizona. Arizona board of Regents, 1992

Carslaw H.S. and Jaeger J.C. *Conduction of Heat in Solids*. Oxford University Press, Oxford, second edition, 1959

Cetas T.C., Richards W.F. and Gross E.J. Physics today, clinic tomorrow. a plan for new system development. *International Journal of Hyperthermia* 10(3):411–417, 1994

Chato J.C. Fundamentals of bioheat transfer. In M Gautherie, ed., *Thermal dosimetry and treatment planning*, Clinical Thermology, chapter 1, pp. 1–56. Springer-Verlag, Berlin, 1990

Chen J. Y. and Gandhi O.P. Electromagnetic deposition in an anatomically based model of man for leakage fields of a parallel-plate dielectric heater. *IEEE Transactions on Microwave Theory and Technique* 37(1):174–180, 1989

Chen M.M. and Holmes K.R. Microvascular contributions in tissue heat transfer. *Annals of the New York Academy of Science* 335:137–150, 1980

Chen Z. P. and Roemer R.B. The effect of large blood vessels on temperature distributions during simulated hyperthermia. *Journal of Biomechanical Engineering - Transactions of the ASME* 114(4):473–481, 1992

Corry P.M., Jabboury K., Kong J.S., Armour E.P., McCraw F.J. and LeDuc T. Evaluation of equipment for hyperthermia treatment of cancer. *International Journal of Hyperthermia* 4(1):53–74, 1988

Cosset J.M. *Interstitial, endocavitary and perfusional hyperthermia*, chapter Interstitial hyperthermia. Springer Verlag, 1990

Coughlin C.T., Wong T.Z., Ryan T.P., Jones E.L., Crichlow R.W., Spiegel P.K. and Jeffery R. Interstitial microwave-induced hyperthermia and iridium brachytherapy for the treatment of obstructing biliary carcinomas. *International Journal of Hyperthermia* 8(2):157–171, 1992

Crezee J. and Lagendijk J.J.W. Experimental verification of bioheat transfer theories: measurement of temperature profiles around large artificial vessels in perfused tissue. *Physics in Medicine and Biology* 35:905–923, 1990

Crezee J. and Lagendijk J.J.W. Temperature uniformity during hyperthermia: the impact of large vessels. *Physics in Medicine and Biology* 37(6):1321–1337, 1992

Crezee J., Mooibroek J., Bos C.K. and Lagendijk J.J.W. Interstitial heating: experiments in artificially perfused bovine tongues. *Physics in Medicine and Biology* 36(6):843–846, 1991

Crezee J., Mooibroek J. and Lagendijk J.J.W. *Interstitial and intracavitary thermoradiotherapy*, chapter Thermal model verification in interstitial hyperthermia, pp. 147–153. Springer, Heidelberg, 1993

Crezee J., Mooibroek J., Lagendijk J.J.W. and van Leeuwen G.M.J. The theoretical and experimental evaluation of the heat balance in perfused tissue. *Physics in Medicine and Biology* 39:813–832, 1994

Crezee J., Van der Koijk J.F., Kaatee R.S.J.P. and Lagendijk J.J.W. Implications of using thermocouple thermometry in 27 MHz capacitively coupled interstitial hyperthermia. *Physics in Medicine and Biology* ?(?):in press, 1997

De Bree J., Kotte A.N.T.J., Van der Koijk J.F. and Lagendijk J.J.W. A 3d treatment planning system for interstitial hyperthermia. In *Proc. 15th Annual Meeting ESHO*, p. 28, Oxford, UK. 1995

De Bree J., Kotte A.N.T.J., Van der Koijk J.F. and Lagendijk J.J.W. A 3D treatment planning system for interstitial hyperthermia and brachytherapy. *The British Journal of Radiology* 1996a. (accepted)

De Bree J., Van der Koijk J.F. and Lagendijk J.J.W. A 3-D SAR model for current source interstitial hyperthermia. *IEEE Transactions on Biomedical Engineering* 43(10):1038–1045, 1996b

De Leeuw A.A.C., Crezee J. and Lagendijk J.J.W. Temperature and SAR measurements in deep-body hyperthermia with thermocouple thermometry. *International Journal of Hyperthermia* 9(5):685–697, 1993

DeFord J.A., Babbs C.F., Patel U.H., Bleyer M.W., Marchosky J.A. and Moran C.J. Effective estimation and computer control of minimum tumour temperature during conductive interstitial hyperthermia. *International Journal of Hyperthermia* 7(3):441–454, 1991

Deurloo I.K.K., Visser A.G., Morawska M., van Geel C.A.J.F., van Rhoon G.C. and Levendag P.C. Application of a capacitive-coupling interstitial hyperthermia system at 27 MHz: study of different applicator configurations. *Physics in Medicine and Biology* 36(1):119–132, 1991

Dickinson R.J. Thermal conduction errors of manganin-constantan thermocouple arrays. *Physics in Medicine and Biology* 30:445–453, 1985

Diederich C.J. and Hynynen K. Ultrasound technology for interstitial hyperthermia, in interstitial and intracavitary thermoradiotherapy. *Seegenschmiedt H. and R. Sauer (eds), Berlin Springer, pp 5* 1993

Diederich C.J., Khalil I.S., Stauffer P.R., Sneed P.K. and Phillips T.L. Direct-coupled interstitial ultrasound applicators for simultaneous thermobrachytherapy: a feasibility study. *International Journal of Hyperthermia* 12(3):401–419, 1996

Duewell S ., Wuthrich R., Buck A., von Weymarn C. and von Schulthess G.K. Mri signal loss due to microcirculation: Phantom studies. *MRM* 14:347–357, 1990

Dutreix A. Can we compare systems for interstitial therapy? *Radiotherapy and Oncology* 3:127–135, 1988

Dutton A.W. and Roemer R.B. Quantitative evaluation of numerical models for the conjugated heat transfer problem in tissue. In *HTD–Vol. 288, Advances in Heat and Mass Transfer in Biological Systems*, pp. 1–7. ASME, 1994

Emami B., Scott C., Perez C.A., Asbell S., Swift P., Grigsby P., Montesano A., Rubin P., Curran W., Delrowe J., Arastu H., Fu K. and Moros E. Phase iii study of interstitial thermoradiotherapy compared with interstitial radiotherapy alone in the treatment of recurrent or persistent human tumors: A prospectively controlled randomized study by the radiation therapy oncology group. *International Journal of Radiation Oncology, Biology and Physics* 34(5):1097–1104, 1996

Emami B., Stauffer P. and Dewhirst M.W. RTOG quality assurance guidelines for interstitial hyperthermia. *International Journal of Radiation Oncology, Biology and Physics* 20:1117–1124, 1990

ESHO task group report 4. Treatment planning and modelling in hyperthermia. Technical report, postgraduate school of medical physics II university of Rome, 1992

Feldmann H.J., Molls M., Hoederath A., Krümpelmann S. and Sack H. Blood flow and steady state temperatures in deep-seated tumors and normal tissues. *International Journal of Radiation Oncology, Biology and Physics* 23:1003–1008, 1992

Fessenden P., Lee E.R., Anderson T.L. Strohbehn J.B., Meyer J.L., Samulski T.V. and Marmor J.B. Experience with a multitransducer ultrasound system for localized hyperthermia of deep tissues. *IEEE Transactions on Biomedical Engineering* 31(1):126–145, 1984

Gentili G.B., Leoncini M., Trembly B.S. and Schweizer S.E. Fdtd electromagnetic and thermal analysis of interstitial hyperthermic applicators. finite-difference time-domain. *IEEE Trans. Biom. Eng. Ref.* 42(10):973–980, 1995

Goffinet D.R., Prionas S.D., Kapp D.S., Samulski T.V., P. Fessenden, Hahn G.M., Lohrback A.W., Mariscal J.M. and Bagshaw M.A. Interstitial iridium-192 flexible catheter radiofrequency hyperthermia treatments of head and neck and recurrent pelvic carcinomas. *International Journal of Hyperthermia* 18:199–210, 1990

Hand J.W. *Interstitial and intracavitary thermoradiotherapy*, chapter Invasive thermometry practice for interstitial hyperthermia, pp. 83–87. Springer Verlag, Berlin, 1993

Hand J.W., Ledda J.L. and Evans N.T.S. Consideration of radiofrequency induction heating for localised hyperthermia. *Physics in Medicine and Biology* 27(1):1–16, 1982

Hand J.W., Trembly B.S. and Prior M.V. Physics of interstitial hyperthermia, radiofrequency and hot water tube techniques. In M Urano and E Douple, eds., *Hyperthermia and oncology*, volume 3. VSP, Zeist, The Netherlands, 1991

Handl-Zeller L. *Interstitial and intracavitary thermoradiotherapy*, chapter Clinical experience of interstitial thermoradiotherapy using hot water perfusion techniques, pp. 212–221. Springer Verlag, Berlin, 1993

Hornsleth S.N. *Radiofrequency regional hyperthermia.* Ph.D. thesis, Aalborg University, Denmark, 1996

Hynynen K. The feasibility of interstitial ultrasound hyperthermia. *Medical Physics* 19:979–987, 1992

James B.J. and Sullivan D.M. Direct use of CT scans for hyperthermia treatment planning. *IEEE Transactions on Biomedical Engineering* 39(8):845–851, 1992

Jia X., Paulsen K.D., Buechler D.N., Gibbs Jr F.A. and Meaney P.M. Finite element simulation of sigma 60 heating in the utah phantom: computed and measured data compared. *Interstitial Journal of Hyperthermia* 10(6):755–774, 1994

Johnson C.C. and Guy A.W. Nonionizing electromagnetic wave effects in biological materials and systems. *Proc. IEEE* 60:692–718, 1972

Kaatee R.S.J.P., Crezee J., Kanis A.P., Lagendijk J.J.W., Levendag P.C. and A.G. Visser. Design of applicators for a 27 mhz multi-electrode current source interstitial hyperthermia system; impedance matching and effective power. *Physics in Medicine and Biology* ?(?):(accepted), 1997a

Kaatee R.S.J.P., Crezee J., Kanis A.P., Lagendijk J.J.W., Levendag P.C. and Visser A.G. Spatial temperature control with a 27 mhz current source interstitial hyperthermia system. *International Journal of Radiation Oncology, Biology and Physics* ?(?):(accepted), 1997b

Kaatee R.S.J.P., Kampmeijer A.G., van Hooije C.M.C., van Rhoon G.C., Kanis A.P., Levendag P.C. and Visser A.G. A 27 MHz current source interstitial hyperthermia system for small animals. *International Journal of Hyperthermia* 11(6):785–796, 1995

Kaatee R.S.J.P., Lagendijk J.J.W, Visser A.G., Kolkman-Deurloo I.K.K., Kroeze H., van Rhoon G.C. and Levendag P.C. An improved 27 MHz capacitive-coupling interstitial hyperthermia system. In E Gerner, ed., *Hyperthermic Oncology 1992*, volume 20, p. 351, Tucson, Arizona. 1992

Kanis A.P., Lagendijk J.J.W., Kaatee R.S.J.P., De Bree J. and Visser A.G. Treatment control of a 27 MHz current source interstitial hyperthermia system. In *ESHO-94 Proceedings*, p. 39. ESHO, 1994

Kapp K.S., Kapp D.S., Stuecklschweiger G., Berger A. and Geyer E. Interstitial hyperthermia and high dose rate brachytherapy in the treatment of anal cancer: a phase I/II study. *International Journal of Radiation Oncology, Biology and Physics* 28:189–199, 1993

Knuth D.E. The art of computer programming. In *Fundamental Algorithms*, volume 1. Addison-Wesley, 1973

Kotte A.N.T.J., De Bree J., Lagendijk J.J.W., Bakker C.J.G., Van der Koijk J.F., Crezee J., Van Leeuwen G.M.J., Raaijmakers B.J., Struikmans H., Hulshof M.C.C.M., Visser A.G. and Battermann J.J. A 3D treament planning system for interstitial hyperthermia. In C Franconi, G Arcangeli and R Cavaliere, eds., *Hyperthermic Oncology 1996, Volume II*, pp. 537–539, Via O. Raimondo 00173 Rome, Italy. I.C.H.O., Tor Vergata, 1996a

Kotte A.N.T.J., De Bree J., Van der Koijk J.F. and Lagendijk J.J.W. Thermal model for

hyperthermia treatment planning incorporating geometrical vessel description. *The British Journal of Radiology* 1996b. (accepted)

Kotte A.N.T.J., De Bree J., Van der Koijk J.F. and Lagendijk J.J.W. Thermal model for hyperthermia treatment planning incorporating geometrical vessel description. *The British Journal of Radiology* 1996c. (accepted)

Kotte A.N.T.J., Van Leeuwen G.M.J., De Bree J., Van der Koijk J.F., Crezee J. and Lagendijk J.J.W. A description of discrete vessel segments in thermal modelling of tissues. *Physics in Medicine and Biology* 41(5):865–884, 1996d

Kotte A.N.T.J., Van Leeuwen G.M.J., De Bree J., Van der Koijk J.F., Crezee J. and Lagendijk J.J.W. A description of discrete vessel segments in thermal modelling of tissues. *Physics in Medicine and Biology* 41(5):865–884, 1996e

Lagendijk J.J.W. A microwave-like LCF interstitial hyperthermia system. *Strahlentherapie und Onkologie* 166(8):521, 1990a

Lagendijk J.J.W. Thermal models: principles and implementation. In S Field and J Hand, eds., *An introduction to the practical aspects of clinical hyperthermia*, pp. 478–512. Taylor & Francis, London, 1990b

Lagendijk J.J.W., Crezee J. and Hand J.W. Dose uniformity in scanned focused ultrasound hyperthermia. *International Journal of Hyperthermia* 10(6):775–784, 1994a

Lagendijk J.J.W., Crezee J. and Mooibroek J. Progress in thermal modelling development. In E Gerner and T Cetas, eds., *Hyperthermic Oncology 1992*, volume 2, pp. 257–261, Tucson, Arizona. 1992

Lagendijk J.J.W., Crezee J. and Mooibroek J. Progress in thermal modelling development. In E Gerner and T Cetas, eds., *Hyperthermic Oncology 1992*, volume 2, pp. 257–261, Tucson, Arizona. Arizona board of Regents, 1993

Lagendijk J.J.W., Hofman P. and Schipper J. Perfusion analyses in advanced breast carcinoma during hyperthermia. *International Journal of Hyperthermia* (4):479–495, 1988

Lagendijk J.J.W. and Mooibroek J. Hyperthermia treatment planning. *Recent results in Cancer Research* 101:119–131, 1986

Lagendijk J.J.W., Schellekens M., Schipper J. and van der Linden P.M. A three-dimensional description of heating patterns in vascularised tissues during hyperthermia treatment. *Physics in Medicine and Biology* 29(5):495–507, 1984

Lagendijk J.J.W., Van der Koijk J.F., Visser A.G., Kaatee R.S.J.P., Crezee J., De Bree J., Kotte A.N.T.J., Kanis A.P., Kroeze H., Levendag P.C. and Battermann J.J. Dose uniformity with the 27 MHz multi-electrode current source interstitial hyperthermia method. In G Bruggmoser and R Mould, eds., *Brachytherapy review, Proceedings German Brachytherapy Conference Freiburg*, pp. 38–44. 1994b

Lagendijk J.J.W., Visser A.G., Kaatee R.S.J.P., Crezee J., Van der Koijk J.F., De Bree J., Kotte A.N.T.J., Kanis A.P., Kroeze H., Levendag P.C. and Battermann J.J. Interstitial hyperthermia & treatment planning: the 27 MHz multi-electrode current source method. *Activity International Nucletron-Oldelft Radiotherapy Journal* (special report 6):83–90, 1995

Lee D.J., O'Neil M., Lam K.S., Rostock R. and Lam W.C. A new design of microwave interstitial applicators for hyperthermia with improved treatment volume. *International Journal of Radiation Oncology, Biology and Physics* 12:203–208, 1986

Lele P.P. *Hyperthermia in cancer therapy*, chapter Physical aspects and clinical studies with ultrasound hyperthermia, pp. 333–367. Hall Medical, Boston, 1983

Levendag P.C., Kaatee R.S.J.P., Visser A.G., Kolkman-Deurloo I.K.K., Van Rhoon G.C., Meeuwis C.A., C.A.J.F. Van Geelm and Van Hooye C. *Interstitial and intracavitary thermoradiotherapy*, chapter Interstitial radiation and/or interstitial hyperthermia for advanced and/or recurrent cancers in the head and neck: a pilot study, pp. 233–240. Springer Verlag, Berlin, 1993

Leybovich L.B. and Kurup R.G. evaluation of microwave interstitial antennas in the phantom with varying cross-section. *International Journal of Radiation Oncology, Biology and Physics* 25:105–112, 1992

Lippman S.B. *C++ primer*. Addison-Wesley, 1991

Lyng H., Monge O.R., Bohler P.J. and Rofstad E.K. Temperature distribution in locally advanced breast carcinoma during hyperthermic treatment: relationship to perfusion, vascular density, and histology. *International Journal of Radiation Oncology, Biology and Physics* 21(2):423–430, 1991

Lyng H., Monge O.R., Sager E.M. and E.K. Rofstad. Prediction of treatment temperatures in clinical hyperthermia of locally advanced breast carcinoma: the use of contrast enhanced computed tomography. *International Journal of Radiation Oncology, Biology and Physics* 21:451–457, 1993

Marchal C., Nadi M., Hoffstetter S., Bey P., Pernot M. and Prieur G. Practical interstitial method of heating operating at 27.12 MHz. *International Journal of Hyperthermia* 5(4):451–466, 1989

Mechling J.A. and Strohbehn J.W. A theoretical comparison of the temperature distributions produced by three interstitial hyperthermia systems. *IJROBP* 12:2137–2149, 1986

Milligan A.J. Canine muscle blood flow during fractionated hyperthermia. *International Journal of Hyperthermia* 3:353–359, 1987

Milligan A.J., Conran P.B., Ropar M.A., McCulloch H.A., Ahuja R.K. and Dobelbower R.R. Predictions of blood flow from thermal clearance during regional hyperthermia. *International Journal of Radiation Oncology, Biology and Physics* 9:1335–1343, 1983

Mooibroek J. and Lagendijk J.J.W. A fast and simple algorithm for the calculation of convective heat transfer by large vessels in three-dimensional inhomogeneous tissues. *IEEE Transactions on Biomedical Engineering* 38(5):490–501, 1991

Murray C.D. The physiological principle of minimum work: I. the vascular system and the cost of blood volume. *Proceedings National Academy of Science U.S.A.* 12:207–214, 1926

Nah B.S., Choi I.B., Oh W.Y., Osborn J.L. and Song C.W. Vascular thermal adaptation in tumors and normal tissue in rats. *International Journal of Radiation Oncology, Biology and Physics* 35:95–101, 1996

Okabe A., Boots B.N. and Sughihara K. *Spatial tessellations: concepts and applications of voronoi diagrams*. John Wiley & Sons, 1992

Oleson J.R., Samulski T.V., Leopold K.A., Clegg S.T., Dewhirst M.W., Dodge R.K. and George S.L. Sensitivity of hyperthermia trial outcomes to temperature and time: implications for thermal goals of treatment. *International Journal of Radiation Oncology, Biology and Physics* 25:289–297, 1993

Overgaard J. Esho newsletter September 1994, 1994

Overgaard J., Gonzalez Gonzalez D., Hulshof M.C.C.M., Arcanangeli G., Dahl O., Mella O. and Bentzen S.M. Randomised trial of hyperthermia as adjuvant to radiotherapy for recurrent or metastatic malignant melanoma. *The Lancet* 345:540–543, 1995

Paulsen K.D. *An introduction to the Practical Aspects of Clinical Hyperthermia*, chapter Power deposition models for hyperthermia applicators, pp. 305–343. Taylor&Francis, London, 1990a

Paulsen K.D. *Thermal dosimetry and treatment planning*, chapter Calculation of power deposition patterns in hyperthermia, pp. 57–117. Springer-Verlag, 1990b

Paulsen K.D., Strohbehn J.W. and Lynch D.R. Theoretical temperature distributions by an annual phased array-type system in ct-based patient models. *Radiation Research, 53* 100:536–552, 1984

Paulsen K.D., Strohbehn J.W. and Lynch D.R. 3d bioelectromagnetic computation on finite elements. *Applied Computational Electromagnetics Soc. Journal* 7(2):9–25, 1992

Pennes H.H. Analysis of tissue and arterial blood temperature in the resting human forearm. *Journal of Applied Physiology* 1:93–122, 1948

Perez C.A., Gillespie B., Pajak T., Hornback N.B., Emami B. and Rubin P. Quality assurance problems in clinical hyperthermia and their impact on therapeutic outcome: a report by the radiation therapy oncology group. *International Journal of Radiation Oncology, Biology and Physics* 16:551–558, 1989

Popel A.S. *Handbook of Bioengineering*, chapter Network models of peripheral circulation. McGraw-Hill, New York, 1987

Potchen E.J., Haacke E.M. and Siebert J.E. chapter Magnetic Resonance Angiography, Concepts and applications. Mosby-Year Book Inc, St. Louis, 1993

Prionas S.D., Kapp D.S., Goffinet D.R., Bagshaw M.A., Ben-Yousef R., Sokol J.L. and Fessenden P. Interstitial radiofrequency-induced hyperthermia. In E Gerner and T Cetas, eds., *Hyperthermic Oncology 1992*, volume 2, pp. 249–253. The Arizona Board of Regents, Tucson, Arizona, 1992

Prionas S.D., Kapp D.S., goffinet D.R., Ben-Yosef R., Fessenden P. and Bagshaw M.A. Thermometry of interstitial hyperthermia given as an adjuvant to brachytherapy for the treatment of carcinoma of the prostate. *International Journal of Radiation Oncology, Biology and Physics* 28(1):151–162, 1994

Rawnsley R.J., Roemer R.B. and Dutton A.W. The simulation of discrete vessel effects in experimental hyperthermia. *Journal of Biomechanical Engineering - Transactions of the ASME* 116(3):256–262, 1994

Roberts D.W., Coughlin C.T., Wong T.Z., Fratkin J.D., Double E.B. and Strohbehn J.W. hyperthermia interstitial and iridium brachytherapy in treatment of malignant glioma. *J. Neurosurg.* 64:581–587, 1986

Roemer R.B. *Biological, physical and Clinical aspects of Hyperthermia*, chapter Heat transfer in hyperthermia treatments: Basic principles and applications, pp. 210–242. AIP, 1988

Roemer R.B. The local tissue cooling coefficient: A unified approach to thermal washout and steady-state 'perfusion' calculations. *International Journal of Hyperthermia* 6:421–430, 1990a

Roemer R.B. Thermal dosimetry. In M Gautherie, ed., *Thermal Dosimetry and Treatment Planning*, pp. 119–214. Springer, 1990b

Roemer R.B. and Cetas C.T. Applications of bioheat transfer simulations in hyperthermia. *Cancer Research* 44:4788s–4798s, 1984

Ryan T.P., Trembly B.S., Roberts D.W., Strohbehn J.W., Coughlin C.T. and Hoopes P.J. Brain hyperthermia: I. interstitial microwave antenna array techniques—the darthmouth experience. *International Journal of Radiation Oncology, Biology and Physics* 29(5):1065–1078, 1994

Salcman M. and Samaras G.M. Interstitial hyperthermia for brain tumors. *J Neuro-Oncology* 1:225–236, 1983

Samulski T.V., Lyons B.E. and Britt R.H. Temperature measurements in high thermal gradients: Ii analysis of conduction effects. *International Journal of Radiation Oncology, Biology and Physics* 11:963–971, 1985

Schepps J.L. and Foster K.R. The UHF and microwave dielectric properties of normal and tumour tissues: variation in dielectric properties with tissue water content. *Physics in Medicine and Biology* 25(6):1149–1159, 1980

Schreier K., Budihna M., Lesnicar H., Handl-Zeller L., Hand J.W., Prior M.V., Clegg S.T. and Brezovich I.A. Preliminary studies of interstitial hyperthermia using hot water. *International Journal of Hyperthermia* 6(2):431–444, 1990

Seegenschmiedt M.H. *Interstitial and intracavitary thermoradiotherapy*, chapter clinical experience of interstitial thermoradiotherapy using microwave techniques, pp. 193–209. Springer, Heidelberg, 1993

Sekins K.M., Emory A.F., Lehmann J.F. and MacDougall J.A. Determination of perfusion field during local hyperthermia with the aid of finite element thermal models. *Journal of Biomedical Engineering* 104:272–279, 1982

Sekins K.M., Lehumn J.F., Esselman P., Dundore D., Emory A.F., deLatevr B.J. and W.B. Nelp. Local muscle blood flow and temperature responses to 915 MHz diathermy as simultaneously measured and numerically predicted. *Arch. Phys. Med. Rehabil.* 65:1–7, 1984

Shimm D.S., Kittelson J.M., Oleson J.R., Aristizabal S.A., Barlow L.C. and Cetas T.C. Interstitial thermoradiotherapy: thermal dosimetry and results clinical. *International Journal of Radiation Oncology, Biology and Physics* 18:383–387, 1990

Silberman A.W., Rand R.W., Storm F.K., Drury B., Benz M.L. and Morton D.L. Phase i trial of thermochemotherapy for brain malignacy. *Cancer* 56:48–56, 1985

Smith S.R. and Foster K.R. Dielectric properties of low-water-content tissues. *Physics in Medicine and Biology* 30(9):965–973, 1985

Sneed P.K., Gutin P.H., Stauffer P.R., Phillips T.L., Prados M.D., Weaver K.A., Suen S., Lamb S.A., Ham B., Ahn D.K., Lamborn K., Larson D.A. and Wara W.M. Thermoradiotherapy of recurrent malignant brain tumours. *International Journal of Radiation Oncology, Biology and Physics* 23:853–861, 1992

Sowinski M.J. and van den Berg P.M. A three-dimensional iterative scheme for an electromagnetic capacitive applicator. *IEEE Transactions on Biomedical Engineering* 37(10):975–986, 1990

Sowinski M.J.; van den Berg P.M. A three-dimensional iterative scheme for an electromagnetic inductive applicator. *IEEE Transactions on Biomedical Engineering* 39(12):1255–1264, 1992

Stauffer P.R. *An introduction to the Practical Aspects of Clinical Hyperthermia*, chapter Techniques for interstitial hyperthermia, pp. 344–370. Taylor&Francis, London, 1990

Stauffer P.R., Diederich C.J. and Seegenschmiedt M.H. *Interstitial heating technologies*, volume 1: biology, physiology, physics, pp. 279–320. Springer Verlag, Berlin, 1995

Stauffer P.R., Sneed P.K., Suen S.A., Satoh T., Matsumoto K., Fike J.R. and Phillips T.L. Comparative thermal dosimetry of interstitial microwave and hyperthermia radiofrequency-lcf. *International Journal of Hyperthermia* 5:307–318, 1989

Stea B., Rossman K., Kittelson J., Shetter A., Hamilton A. and Cassady J.R. interstitial irradiation versus interstitial thermoradiotherapy for supratentorial malignant gliomas: a comparative survival analysis. *International Journal of Radiation Oncology, Biology and Physics* 30(3):591–600, 1994

Steger A.C. *Interstitial and intracavitary thermoradiotherapy*, chapter Laser technology for interstitial hyperthermia, pp. 63–74. Springer, Heidelberg, 1993

Strohbehn J.W. temperature distributions from interstitial RF electrode hyperthermia systems: theoretical predictions. *International Journal of Radiation Oncology, Biology and Physics* 9:165–1667, 1983

Strohbehn J.W. Hyperthermia equipment evaluation. *International Journal of Hyperthermia* 10(3):429–432, 1994

Strohbehn J.W., Trembly B.S. and Douple E.B. blood flow effects on the temperature distribution from an invasive microwave antenna array used in cancer therapy. *IEEE Transactions on Biomedical Engineering* 29:649–661, 1982

Stuchly M.A., Krasewski A., Stuchly S.S. and Smith A.M. Dielectric properties of animal tissues in vivo at radio and microwave frequencies: comparison between species. *Physics in Medicine and Biology* 27(7):927–936, 1982

Sullivan D.M. Optimization methods for treatment planning in the sigma 60. In E Gerner and T Cetas, eds., *Hyperthermic Oncology 1992*, volume 2, pp. 219–221, Tucson, Arizona. 1993

Turner P.F. *Electromagnetic hyperthermia devices and methods*. Master's thesis, Utah University, Salt Lake City, 1983

Van der Koijk J.F., Bakker C.G.M. and Lagendijk J.J.W. Estimation of dielectric tissue properties for hyperthermia treatment planning using MRI. In *ESHO-93*, p. 55, Brussels, Belgium. European Society of Hyperthermic Oncology, 1993

Van der Koijk J.F., Crezee J. and Lagendijk J.J.W. Thermal properties of capacitively coupled electrodes in interstitial hyperthermia. *???* ?(?):?, 1997a

Van der Koijk J.F., Crezee J., Van Leeuwen G.M.J., Battermann J.J. and Lagendijk J.J.W. Dose uniformity in MECS interstitial hyperthermia: the impact of longitudinal control in model anatomies. *Physics in Medicine and Biology* 41(3):429–444, 1996

Van der Koijk J.F., De Bree J., Crezee J. and Lagendijk J.J.W. Numerical analysis of capacitively coupled electrodes for interstitial hyperthermia. *International Journal of Hyperthermia* ?(?):?, 1997b

Van der Koijk J.F., Lagendijk J.J.W. and Crezee J. Temperature uniformity in interstitial hyperthermia. In *Proc NAHS 1995*, San Jose, CA. NAHS, 1995

Van der Zee J. Eindverslag ontwikkelingsgeneeskunde project og 89-32. 1993

Van der Zee J. personal communication, 1995

Van Es C.A., Wijrdeman H.K., De Leeuw A.A.C., Mooibroek J., Lagendijk J.J.W. and Battermann J.J. Regional hyperthermia of pelvic tumours using the utrecht coaxial tem system: a feasibility study. *International Journal of Hyperthermia* 11(2):173–186, 1995

Van Leeuwen G.M.J., Kotte A.N.T.J., Crezee J. and Lagendijk J.J.W. Tests of the geometrical description of blood vessels in a thermal model using counter current geometries. *Physics in Medicine and Biology* (submitted)

Van Leeuwen G.M.J., Kotte A.N.T.J., De Bree J., Van der Koijk J.F., Crezee J. and Lagendijk J.J.W. Accuracy of geometrical modelling of heat transfer from tissue to blood vessels. *Physics in Medicine and Biology* (submitted-b)

Van Leeuwen G.M.J., Kotte A.N.T.J., De Bree J., Van der Koijk J.F. and Lagendijk J.J.W. Investigation of the thermal effects of separate vessel generations in artificial vascular networks. In C Franconi, G Arcangeli and R Cavaliere, eds., *Hyperthermic Oncology 1996, Volume II*, pp. 495–497, Via O. Raimondo 00173 Rome, Italy. I.C.H.O., Tor Vergata, 1996

Van Leeuwen G.M.J., Kotte A.N.T.J., and Lagendijk J.J.W. Network generation algorithm (in preparation)

Van Wieringen N., van Dijk J.D.P., , Van Veldhuizen J. and Nieuwenhuys G.J. The effect of catheters and coatings on the performance of palladium–nickel thermoseeds: design and evaluation of implantation techniques. *International Journal of Hyperthermia* p. (accepted), 1996a

Van Wieringen N., van Dijk J.D.P., Nieuwenhuys G.J., Snel C.E. and Cetas T.C. Power absorption and temperature control of multi-filament palladium-nickel thermoseeds for interstitial hyperthermia. *Physics in Medicine and Biology* 41:2367–2380, 1996b

Vernon C.C., Hand J.W., Field S.B., Machin D., Whaley J.B., Van der Zee J., Van Putten W.L.J., van Rhoon G.C., van Dijk J.D.P., Gonzalez Gonzalez D., Liu F.F., Goodman P. and Sherar M. Radiotherapy with or without hyperthermia in the treatment of superficial localised breast cancer: results from five randomised controlled trials. *International Journal of Radiation Oncology, Biology and Physics* ((in press)), 1996

Visser A.G., Deurloo I.K.K., Levendag P.C., Ruifrok A.C.C., Cornet B. and van Rhoon G.C. An interstitial hyperthermia system at 27 MHz. *International Journal of Hyperthermia* 5(2):265–276, 1989

Waterman F.M., Nerlinger R.E., Moyland D.J. and Leeper D.B. Response of human tumor blood flow to local hyperthermia. *International Journal of Radiation Oncology, Biology and Physics* 13:75–82, 1987

Weinbaum S. and Jiji L.M. A new simplified bioheat equation for the effect of blood flow on local average tissue temperature. *Journal of Biomechanical Engineering - Transactions of the ASME* 107(2):131–139, 1985

Wonnell T.L., Stauffer P.R. and Langberg J.J. Evaluation of microwave and radio-frequency catheter ablation in a myocardium-equivalent phantom model. *IEEE Transactions on Biomedical Engineering* 39(10):1086–1095, 1992

Wust P., Stahl H., Löffel J., Seebass M., Riess H. and Felix R. Clinical, physiological and anatomical determinants for radiofrequency hyperthermia. *International Journal of Hyperthermia* 11(2):151–167, 1995

Zhu L. and Weinbaum S. A model for heat transfer from embedded blood vessels in two-dimensional tissue prepearations. *Journal of Biomechanical Engineering - Transactions of the ASME* 117(1):64–73, 1995

Zwamborn A.P.M., Van den Berg P.M., Mooibroek J. and Koenis F.T.C. Computation of three dimensional electromagnetic-field distributions in a human body using the weak form of the cgfft method. *Applied Computational Electromagnetics Soc. Journal* 7(2):26–42, 1992

Nawoord

De basis voor dit proefschrift is gelegd in een omgeving die erg stimulerend was. Jan Lagendijk, mijn eerste 'baas', heeft mij een stijl van leiding geven getoond die erg to-the-point, open en doelgericht is, maar ook vrijheid laat om iets eens zover uit te spitten dat je het bijna niet leuk meer vindt. Hans Crezee bleek te beschikken over een welhaast schokkende nuchterheid, die hij lijkt te combineren met groot psychologisch inzicht en met veel vakkundigheid. Het afscheid van het 'jonge honden team', waar ik met Jacob de Bree, Alexis Kotte en Gerard van Leeuwen deel van uitmaakte was niet gemakkelijk. Hoewel, of wellicht omdat, de stijl van aanpak van problemen binnen ons team zeer verschilde ontstond er een goede samenwerking. Ik hoop dat ik nog veel met zulke enthousiaste, toegewijde en creatieve mensen zal mogen samenwerken!

Professor Battermann heeft mij eens op bezoek gehad bij een implantatie voor brachytherapie. Zijn uitnodigende gebaren ten spijt heb ik een en ander niet van al te nabij meegemaakt, maar deze gebeurtenis heeft mij toch een heel andere kijk op klinisch ingrijpen gegeven.

Bert Cramer, Jan Kok, Cees–cmos–Imhof (die gelukkig erg goed sinaasappels kan vangen, om over sneeuwballen nog maar te zwijgen) en Iris Gademan stonden altijd klaar als er iets in elkaar gezet, afgewogen of geprutst moest worden. Ook andere leden van de groep fysisch assistenten en versnellertechnici waren altijd bereid een helpende hand te leveren waar dat van pas kwam. Met Jack de Koning heb ik nog altijd te doen als ik denk aan zijn taxi-avontuur bij Dordrecht na een avondje doorzakken in Utrecht. Hier is zijn levendige verhaalstijl natuurlijk ook debet aan. Liesbeth van Doodewaard en Joke van Randwijk wisten altijd waar iedereen zich bevond, wat een knappe prestatie is.

Met Robert Kaatee, Andries Visser en Bart Kanis heb ik eigenlijk wat minder te maken gehad dan ik wel zou willen, hoewel ik in dezelfde stad woon waar zij hun werkplek hebben. Als er iets te bespreken was dan ging dat in een zeer goede sfeer en de samenwerking was dan ook aangenaam.

Rob Beersma heeft mij getoond wat iemand die een echte informatica-opleiding heeft genoten vermag; Ramesh Baghwandien vormde met $\pi\alpha(b)$ een overslaanbaar duo op het gebied van de geïmproviseerde humor. Ik hoop dat zij zich in hun nieuwe werkkringen (en hun eventuele lease-auto's) op hun gemak voelen. Ric Exterkate ben ik dankbaar voor de moeite die hij voor mij gedaan heeft om te zorgen dat ik ook terwijl ik niet meer in het AZU werkte gebruik kon blijven maken van de rekenfaciliteiten in Utrecht. Met Jaap Mooijbroek heb ik een plezierig bezoek aan Rome gebracht, naar aanleiding waarvan ik bijna een extra artikel heb geschreven, wat echter door experimentele complicaties in het slop raakte. Astrid de Leeuw heeft mijn aandacht voor groepsprocessen nieuw leven ingeblazen. Van Bas Raaijmakers vraag ik mij af of 'ie T*M nog wel eens leest.

Discussies op medisch/biologisch gebied werden (soms) vol vuur gevoerd met Derk Rutgers en Pieter Hofman. Harm Wijrdeman was een waardig tegenstander bij het testen van gevaarlijke stellingen.

De samenwerking met Chris Bakker en met Rien Moerland bij de MR metingen die in 1993 voor mij zijn uitgevoerd vond ik erg stimulerend. Ook de relatie met 3D-CV (onder andere tijdens de C++ cursus van Karel Zuiderveld en door het betrouwbare werk van Bart Muijzer) was goed. Marcel Metselaar en Jan de Groot heb ik regelmatig lastig gevallen met moeilijke vragen; ze wisten daar altijd goed raad mee.

Vele docenten die *echt* enthousiasme voor hun vak opbrachten staan mij nog helder voor de geest. Zonder die mensen was ik hier nooit terechtgekomen. Het is niet gebruikelijk de Nederlandse staat te bedanken voor de mogelijkheden die je geboden werden. Ik denk dat dat niet terecht is. De organisatie van de Nederlandse samenleving maakte voor mij veel mogelijk.

Een aantal mensen heeft mij de afgelopen tijd wel erg intensief bijgestaan. In het bijzonder wil ik Karst Meijer en Erik van den Broek bedanken voor de inspanningen die zij zich hebben getroost. Alexis Kotte heeft zich buitengewoon ingespannen om de verschillende kwaliteitsparameters van de entourage gelijktijdig te optimaliseren. Barbara Calon zal zich wel twee keer bedenken voordat ze aan het schrijven van een proefschrift begint...

Al deze mensen, die mij enkele van de mooiste jaren van mijn leven hebben geschonken, wil ik graag zeer hartelijk bedanken.

Degene die in dit kader de meeste erkenning verdient is mijn moeder. Maar dat is een ander verhaal.

Curriculum Vitae

De auteur van dit proefschrift is in Rotterdam geboren op 9 juli 1965. In 1982 behaalde hij het diploma bij de Hildegardisschool voor IVO-MAVO. Drie jaar later volgde de 'verklaring' van de Christiaan Huygens MTS (vakgebied elektronica) en in 1986 het eerste jaar van de HTS (vakgebied elektrotechniek), beide te Rotterdam. Eind 1986 begon hij aan de studie voor natuurkundig ingenieur van de Technische Universiteit te Delft. In juni 1987 behaalde hij het propedeutisch examen en in februari 1992 het doctoraal. Hij studeerde af in de vakgroep Lage Temperaturen onder leiding van prof. dr. H. Postma.

Van mei 1992 tot mei 1996 werkte hij als toegevoegd onderzoeker op de afdeling Radiotherapie van het Academisch Ziekenhuis Utrecht. Het werk vond plaats in de groep van dr. ir. J.J.W. Lagendijk. De nadruk lag hier op het modelleren van het fysisch gedrag van een verwarmingssysteem dat in levend menselijk weefsel kan worden toegepast.

Op het moment van schrijven werkt hij bij KPN-Research, het laboratorium van Koninklijke PTT Nederland.

Index